Dissertation
submitted to the
Combined Faculties for the Natural Sciences and for Mathematics
of the Ruperto-Carola University of Heidelberg, Germany
for the degree of
Doctor of Natural Sciences

Put forward by
Diplom-Physicist: Marcel Oberländer
Born in: Blankenburg (Harz), Germany
Oral examination: December the 16th, 2009

Three-dimensional reengineering of neuronal microcircuits

The cortical column in silico

Referees:
Prof. Dr. Bert Sakmann
Prof. Dr. Karlheinz Meier

Abstract German

Die hier präsentierte Dissertation beschreibt eine Pipeline zum Nachbau drei-dimensionaler, anatomisch realistischer, funktioneller neuronaler Netzwerke mit subzellulärer Auflösung. Die Pipeline besteht aus fünf Methoden:

1. "NeuroCount" ergibt die Anzahl und drei-dimensionale Verteilung aller neuronalen Zellkörper in großen Hirnregionen.
2. "NeuroMorph" ergibt verlässliche neuronale Rekonstruktionen, inklusive dendritischer and axonaler Morphologien.
3. "daVinci" registriert neuronale Morphologien in ein standartisiertes Bezugssystem.
4. "NeuroCluster" gruppiert die standartisierten Rekonstruktionen objektiv in anatomische Neurontypen.
5. "NeuroNet" kombiniert die Anzahl und Verteilung der Neuronen mit den standartisierten Rekonstruktionen und bestimmt die Anzahl synaptischer Kontakte, in Abhängigkeit von Neurontyp und Neuronposition, für jedwede zwei Neurontypen.

Die entwickelten Methoden werden anhand des Nachbaus eines Netzwerkes im somatosensorischen System der Ratte demonstriert. Dort existiert eine eins-zu-eins Repräsentation zwischen der sensorischen Information, aufgenommen durch ein einzelnes Barthaar, und abgetrennten Bereichen im Thalamus und Kortex. Der Nachbau dieses Kreislaufes resultiert in einem zylinderförmigen Netzwerk Modell bestehend aus ≈15200 anregenden kortikalen, durch Kompartemente repräsentierten, Neuronen. Dieses Netzwerk ist mit ≈285 präsynaptischen thalamischen Neuronen verbunden. Anregung dieser "kortikalen Kolumne *in silico*" mit gemessenen physiologischen Signalen, wird einen Beitrag zum Verständniß neuronalen Informationsverarbeitung in Säugetiergehirnen leisten.

Abstract English

The presented thesis will describe a pipeline to reengineer three-dimensional, anatomically realistic, functional neuronal networks with subcellular resolution. The pipeline consists of five methods:

1. "NeuroCount" provides the number and three-dimensional distribution of all neuron somata in large brain regions.
2. "NeuroMorph" provides authentic neuron tracings, comprising dendrite and axon morphology.
3. "daVinci" registers the neuron morphologies to a standardized reference framework.
4. "NeuroCluster" objectively groups the standardized tracings into anatomical neuron types.
5. "NeuroNet" combines the number and distribution of neurons and neuron-types with the standardized tracings and determines the neuron-type- and position-specific number of synaptic connections for any two types of neuron.

The developed methods are demonstrated by reengineering the thalamocortical lemniscal microcircuit in the somatosensory system of rats. There exists an one-to-one correspondence between the sensory information obtained by a single facial whisker and segregated areas in the thalamus and cortex. The reengineering of this pathway results in a column-shaped network model of $\approx$15200 excitatory full-compartmental cortical neurons. This network is synaptically connected to $\approx$285 pre-synaptic thalamic neurons. Animation of this "cortical column *in silico*" with measured physiological input will help to gain a mechanistic understanding of neuronal sensory information processing in the mammalian brain.

Acknowledgements

A very special Thanks to:

- my supervisor Prof. Dr. Bert Sakmann for his unlimited support, trustfulness and encouragement during the past years and the opportunity to continue the presented work at the Max Planck Florida Institute.
- my family and friends, especially to my parents, who supported me during my entire life and the past years of study.
- my girlfriend Aline, who supported me during the past five years and took care that I also spent some time outside the institute.

A special Thanks to:

- my collaborators: Albert Berman, Dr. Philip J. Broser, Dr. Randy M. Bruno, Dr. Christiaan P. J. de Kock, Vincent J. Dercksen, Dr. Moritz Helmstädter, Dr. Stefan Hippler, Dr. Stefan Lang and Hanno-Sebastian Meyer. Without teamwork and your help, none of the presented results would have been possible.
- the undergraduate students under my supervision: Caroline, Firas, Jasmin, Kristina, Melanie, Rita, Robert, Stefan, Stefanie and Tatjana. Without you doing all the tedious, time-consuming tracings, counts, programming and sample preparation, none of the presented results would have been possible within three years.
- my thesis committee, Prof. Dr. Bert Sakmann, Prof. Dr. Alexander Borst and Prof. Dr. Tobias Bonhöffer, for fruitful discussions and continuous encouragement.
- Chris Roome, Wulf Kaiser, Klaus Bauer and Marlies Kaiser, who helped me with every technical problem, even after I moved to Munich.

Contents

List of Tables

List of Figures

Chapter 1

Introduction

- **Definition 1:** *In vivo* refers to studies conducted in the living organism.
- **Definition 2:** *In vitro* refers to studies performed (literally in glass) in the laboratory.
- **Definition 3:** *In silico* refers to studies of mechanistic numerical computer based models to complement experiments done *in vitro* or *in vivo*.

1.1 Neuronal circuits: from *in vitro/in vivo* towards *in silico*

One fundamental challenge in neuroscience is to understand how brains process sensory information about the environment and how this can be related to the animal's behavior. The here presented work will focus on this question at the level of anatomically realistic functional neuronal networks with subcellular resolution. In general, neuronal networks are composed of chemically or electrically coupled local and long-range microcircuits of anatomically and physiologically classified cell types. Specifically, each neuron is composed

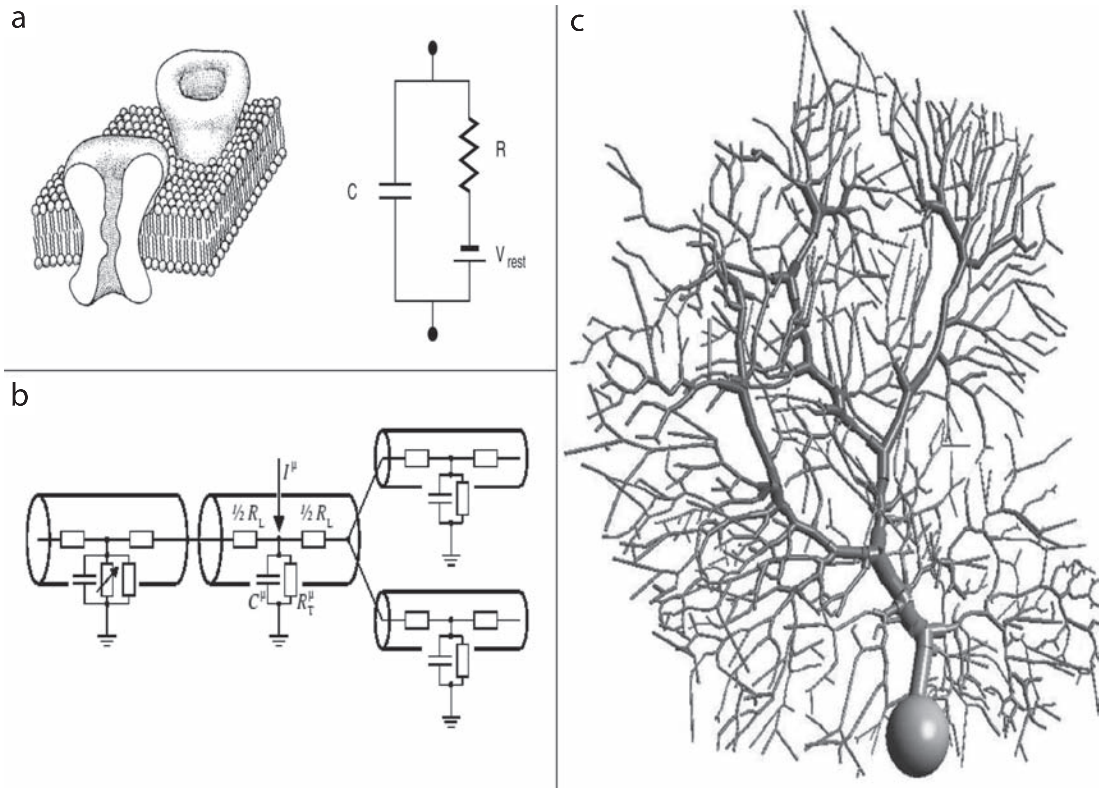

Figure 1.1: ***In silico* single neuron model.** *(a) Figure adopted from [1]. Left: the 30-50 Å thin bilayer of lipids isolates the extracellular side from the intracellular one. From an electrical point of view, the resultant separation of charge across the membrane acts like a capacitance. Ion channels (here voltage-independent) provide a conductance through the membrane. Right: Associated passive electrical (RC-)circuit, consisting of a capacitance and a resistance in series with a battery, which accounts for the neuron's resting potential* V_{rest}*. (b) Figure adopted from [2]. Multi-compartment neuron model. Spatial discretization of the cable equation results in multiple coupled compartments, where each one is locally equivalent to a uniform cable and may contain nonlinear (e.g.voltage-dependent) ionic currents. (c) Figure adopted from [3]. Realistic full-compartmental model of a cerebral Purkinje neuron. Reconstructed bifurcations and variations in diameter and electronic properties are incorporated into the model. Such models are capable to reproduce measured sub- and suprathreshold physiological responses and complex dendritic computations.*

of a cell body (soma), multiple dendrites and one axonal tree, which receive electrical input from and transfer output towards other neurons, respectively. Hence, pioneered by Ramón y Cajal about a century ago, neurons are usually grouped anatomically with respect to their soma shape, dendrite morphology and/or axonal branching pattern.

Functionally, their (electro)physiological membrane properties can be described by electrical circuits containing a capacitance and resistance (RC-circuit) (Fig.1.1a). During equilibrium states, a voltage difference arises from deviating ion concentrations between the inside and outside of the cell's membrane. This resultant resting potential (V_{rest}) is cell-type specific, but typically around -70mV. The membrane itself functions as a capacitance (C), which contains small pores (ion channels) with channel-type specific resistances (R_i). These pores mediate ionic currents across the membrane. Some channels are continuously open (passive or leaky) and others open and close actively with respect to voltage or chemical ligand concentration. Such active (e.g. voltage-dependent) conductances were first described in a neuron model by Hodgkin and Huxley (HH) in 1952:

$$C\frac{dV}{dt} = -(\sum_i I_i + I_{leak}), \tag{1.1}$$

where

$$I_i = \frac{V - E_i}{R_{i(V,t)}}, \tag{1.2}$$

represents voltage-dependent channel kinetics and E_i the reversal potential of each ion channel type. Positive signs of E_i (e.g. $E_{Na} = 54mV$) reflect lower ion concentrations inside the neuron, resulting in inward currents upon depolarization of the membrane. In contrast, negative signs (e.g. $E_K = -77mV$) represent outward currents upon depolarization. This model, successfully explains a fast membrane depolarization, called action potential (AP) or spike, which is believed to be the fundamental electrophysiological unit in information processing. Simplified, fast channels permeable for inwardly streaming positively charged ions (e.g. Na^+) open once a channel-specific voltage threshold is reached. The resultant depolarization opens more and more channels and hence an AP is elicited. By immediate inactivation of the depolarizing channels (in case of Na^+ by reaching an inactivation threshold) and simultaneous slow opening of channels permeable for outward streaming positively charged ions (e.g. K^+), the membrane potential is reset to rest. This process is called suprathreshold activity, in contrast to subthreshold activity, which describes changes of the membrane potential mediated largely by ligand-gated rather than voltage-gated ion channels.

Further development of electrical neuron models by Wilfred Rall, who believed that the complexity of the dendrites and axonal arborization would affect the neuronal processing, resulted in a cable theory for neurons. Numerous bifurcations as well as variations in diameter and electrical properties along the neuronal branches, however diminish the possibility to find analytical solutions for the resultant cable equations [4]. This lead to numerical solutions of spatially discrete, anatomy based neuron models composed of multiple HH-typed compartments (Fig.1.1c), each locally resembling a uniform cable (Fig.1.1b).

Initiated by Roger Traub and colleagues, many of these full-compartmental neuron models with active HH-type properties were synaptically interconnected, resembling realistic microcircuits and carrying out realistic neuronal operations. Following this tradition, attempts to reengineer the three-dimensional anatomy and connectivity of functional networks of many thousand full-compartmental neurons, were started [5], [6]. Such goals would be unfeasible without continuously increasing computing power and recently available large scale imaging techniques.

Initiated by Bert Sakmann, my colleges and I aim to reconstruct a functionally well defined network in the primary somatosensory cortex (S1) of four week old rats (i.e. post-natal day 28, p28). The so called "cortical (barrel) column" is related in a one-to-one fashion to information acquired by a single facial whisker hair on the animal's snout. It has a diameter of $\approx 400 \mu m$, a height of 2mm and contains about ≈ 18000 neurons. Functional output from this network, based on single whisker information, is sufficient to trigger simple behaviors, such as decision making. Hence, animation of a realistically reengineered cortical column with single whisker input, measured *in vivo*, will potentially yield new insights and understanding of principle mechanisms that explain how the brain translates environmental input into behavioral responses.

The mammalian cortex is organized into six layers (L1-L6) and receives input from, or transfers output towards other brain areas, such as the thalamus. Hence, many anatomical and functional studies of cortical columns in S1 revealed neuronal microcircuits between (interlaminar) and within (intralaminar) layers, from the thalamus to the cortex (thalamocortical) and vice versa (corticothalamic). However, due to its complexity, a quantitative three-dimensional anatomical description of these circuits, their constituents and connections is still missing. Figure 1.2 summarizes the general elementary building blocks necessary to quantitatively describe and reengineer *in silico* neuronal microcircuits, such as an average cortical column [5]:

1. To model full-compartmental neurons with active HH properties, three-dimensional axonal and dendritic morphology, ion channel composition, and distributions and electrical properties of the different types of neuron are required, as well as the total numbers of neurons in the microcircuit and the relative proportions of the different types of neuron.

2. To model synaptic connections, the physiological and pharmacological properties of the different types of synapses that connect any two types of neurons are required. In addition, statistics on which part of the axonal arborization (presynaptic innervation pattern) connects to which regions of the target neuron (postsynaptic innervation

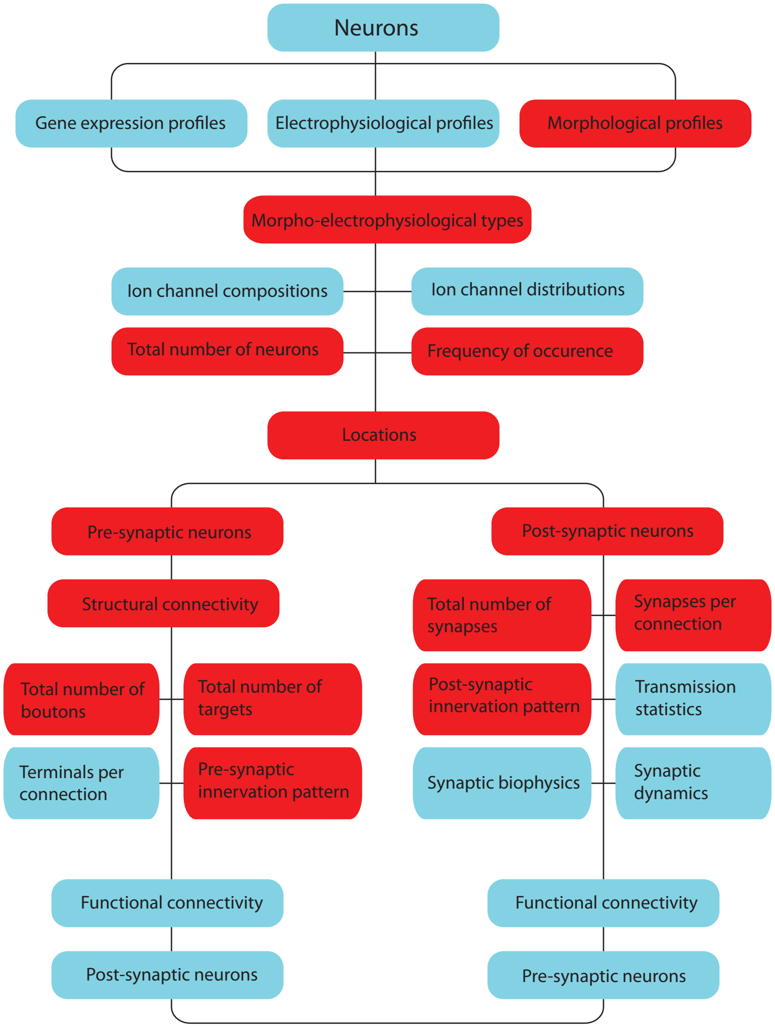

Figure 1.2: **Elementary building blocks of neuronal circuits.** *Microcircuits are composed of neurons and synaptic connections between them. To model neurons, three-dimensional morphology, ion channel composition, distributions and electrical properties of the different types of neurons are required. Further the total number of neurons in the microcircuit and the relative proportions of the different types of neurons are needed. To model synaptic connections, the physiological and pharmacological properties of the different types of synapses that connect any two types of neurons are required. In addition the pre- and postsynaptic innervation statistics are necessary. The red items will be addressed in the presented thesis. Figure adopted from [5].*

pattern) needs to be known. Further, the number of synapses involved in forming connections, and the connectivity statistics between two types of neuron need to be determined.

The here presented work will focus on the anatomical prerequisites of *in silico* microcircuits (red in Fig.1.2), which will be obtained by five custom designed new methods:

NeuroCount, NeuroMorph, daVinci, NeuroCluster and NeuroNet.

NeuroCount automatically extracts the number and three-dimensional distribution of neuron somata in some cubic millimeter large volumes. NeuroMorph is a semi-automated tool to reconstruct the full three dimensional branching pattern of dendrites and axonal arbor of single neurons. Both methods are less time-consuming and more objective than previously used manual approaches. In consequence, statistically significant samples of anatomical data are generated, which yield a quantitative determination of:

1. average absolute numbers and three-dimensional distributions of excitatory (glutamatergic) and inhibitory (GABAergic) neuron somata,
2. average three-dimensional dendritic and axonal features of individual morphological neuron-types.

daVinci registers the neuron tracings into a standardized reference frame of a cortical barrel column. NeuroCluster then enables to objectively group the neurons into morphological classes. Finally, NeuroNet combines the three-dimensional neuron soma distributions, the determined neuron-types and reconstructions, with the standardized reference system of a cortical column and finally yields:

1. the three-dimensional presynaptic innervation of local and long-range microcircuits,

2. the three-dimensional postsynaptic innervation for individual neuronal cell-types,
3. the average number and subcellular three-dimensional organization of synapses between any two types of neurons.

Ultimately, the presented methods and results lead to an *in silico* network model of a cortical column, which contains ≈15200 excitatory full-compartmental neurons within a volume of 0.24 cubic millimeters in S1. The neurons are divided into eight classified cell types and synaptically connected to ≈285 thalamocortical axonal trees. The anatomical, functional and behavioral relevance for this network will be introduced within the subsequent section.

1.2 The ”whisker-barrel-system” in rats

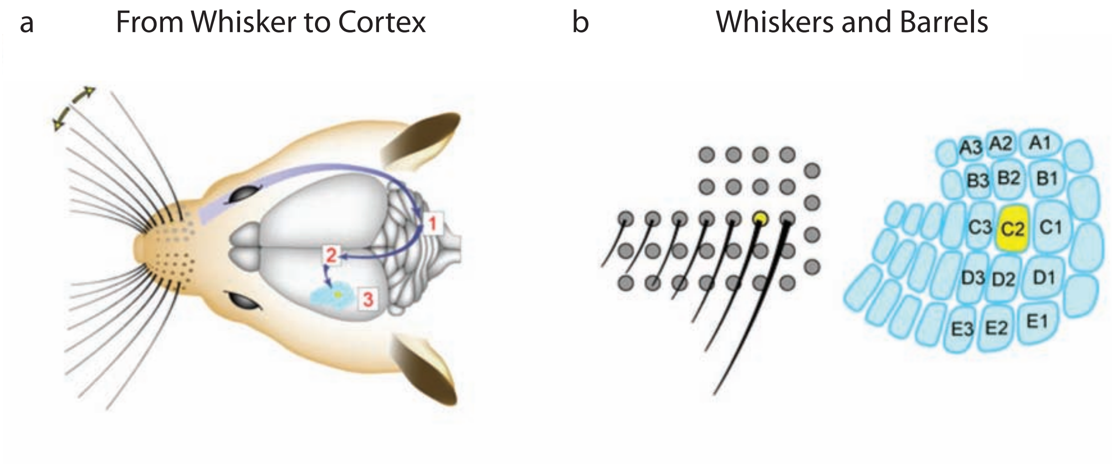

Figure 1.3: **One whisker one barrel hypothesis.** *(a) Information about deflection of a single whisker is transmitted to the brain stem (1), to the thalamus (2) and finally to S1 (3). (b) The layout of whisker follicles on the snout of rodents is identical between rats and mice (left, C-row whiskers shown). Anatomical structures in L4 of S1 are termed ”barrels”. The spatial organization of these barrels resembles the one of the whiskers, giving rise to the hypothesis that each barrel processes the information from its corresponding whisker. The nomenclator for both whiskers and barrels consists of rows (A-E) and arcs (1, 2, 3, etc.). Figure adopted from [7].*

About forty years ago, Thomas Woolsey and Hendrik Van der Loos first described a remarkable correspondence between the pattern of the whiskers on the face of a mouse and the spatial organization of neuron clusters (barrels) in its primary somatosensory cortex [8]. They hence suggested the ”one-barrel-one-whisker” hypothesis, which proposed that each cortical barrel is activated by an individual whisker. Shortly after, anatomical as well as functional evidence for this hypothesis was observed (Figure 1.3).

1.2.1 Anatomy of the whisker system

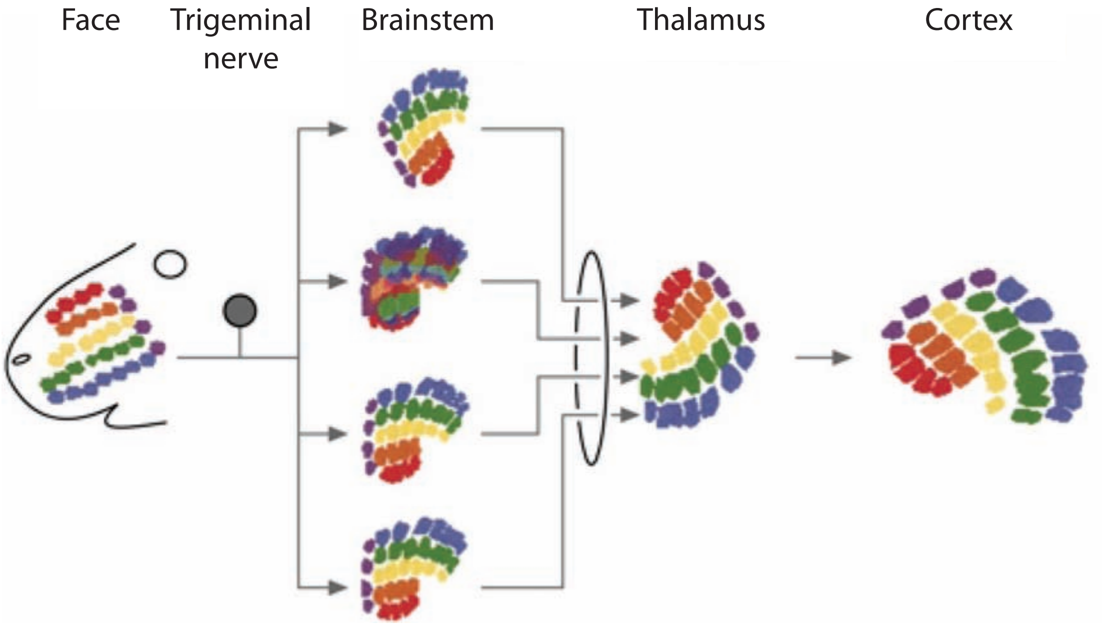

Figure 1.4: **Anatomy of the whisker system.** *Each peripheral axon in the trigeminal nerve innervates one whisker follicle. Centrally the whiskers are aggregated in whisker related bundles that terminate in several nuclei in the brainstem. From top to bottom: principal sensory nucleus and spinal trigeminal complex subnuclei: oralis, interpolaris and caudalis. ”Barrelettes” are present in all but the subnuclei oralis. Whisker-related aggregations of afferent fibres and somata are also observed in the thalamus and S1. Figure adopted from [9].*

The subsequent anatomical description of the whisker system is in parts adopted from Daniel Simons and Peter Land [9] and illustrated by Figure 1.4.

Rats, like most nocturnal rodents, use their whiskers as complex tactile sensory organs to explore their environment. Muscle slings around the whisker follicle move the whisker hairs back and fourth in a rhythmic 10-Hz pattern, called ”whisking”. A whisker follicle is innervated by 100 to 150 large myelinated axons of primary afferent neurons located in the trigeminal ganglion. Each fibre innervates only a single follicle and their functional response differs in three features:

1. their preferred direction of whisker movement,
2. their AP firing patterns caused by whisker movement versus steady state displacement,
3. and their relative sensitivities to deflection amplitude and velocity.

Further, each primary afferent neuron responds to stimulation of only a single whisker. The peripheral pattern of innervation is thus as discrete and punctuate as the whiskers themselves. In consequence, these discrete peripheral nerve fibres transmit information that can be used by the brain to determine the location, size and texture of touched objects.

In the central nervous system (CNS), whisker nerves terminate in several nuclear groups in the brainstem: the principle sensory nucleus and three divisions of the spinal trigeminal complex: oralis, interpolaris and caudalis. Small, whisker-related cell groups, called "barrelettes", are clearly visible in the principle sensory nucleus, somewhat less discernable in spinal trigeminal complex: interpolaris and caudalis, and absent altogether in oralis. The clearly visible barrelettes in nucleus pricipalis reflect a functional correspondence between the barrelet neurons and a single whisker, whereas the other nuclei are responsive to multiple whiskers.

The brainstem neurons transmit whisker-related information to somatosensory regions of the contralateral thalamus. The major recipient of input from the principal sensory nucleus is the medial division of the ventral posterior nucleus (VPM), which like the principle sensory nucleus and S1, contains groups of neurons, that are related to the information from a single whisker. In VPM these groups are in the form of elongated ovoids, called barreloids. The response properties of barreloid neurons is actively regulated by inhibitory circuits involving feedback connections from thalamic reticular nucleus (RT). Moreover, both VPM and RT receive feedback from corticothalamic neurons in the barrel cortex, influencing how whisker information is pre-processed in the thalamus, before it arrives in the cortex itself.

Barreloid neurons are the major source of afferent input to the barrel cortex, and neurons in a barrel receive thalamic inputs largely, although not exclusively, from their corresponding barreloid. Thalamocortical VPM axons arborize selectively throughout the centers of individual barrels and mainly innervate dendrites in L4, the lower part of L5 (L5B) and the upper part of L6.

The barrels are separated from one another by cell-sparse zones, called septa. Unlike their barrel counterparts, septal neurons often extend their dendrites into neighboring barrels, where they are likely to be contacted to barreloid (VPM) axons. Septal and barrel neurons, mainly in L1 and the upper part of L5 (L5A), receive additional afferent thalamocortical input from the medial division of the posterior nucleus (POm), the major thalamic relay for interpolaris and caudalis processing streams. Hence, related target neurons typically receive information involving many neighboring whiskers. In summary, information of whisker deflection is processed along two independent pathways (Figure 1.5). One, refereed to as the "lemniscal" pathway, comprises clear anatomical maps segregating neighboring whisker representations from the periphery, via barrelettes in the principal sensory nucleus of the brainstem, barreloids in the VPM of the thalamus, up to barrel regions in S1. There, the primary input is within L4, L5B and L6. This pathway is regarded as a labeled-line single-whisker signaling pathway.

In contrary, the second pathway, referred to as "paralemniscal", represents multi-whisker

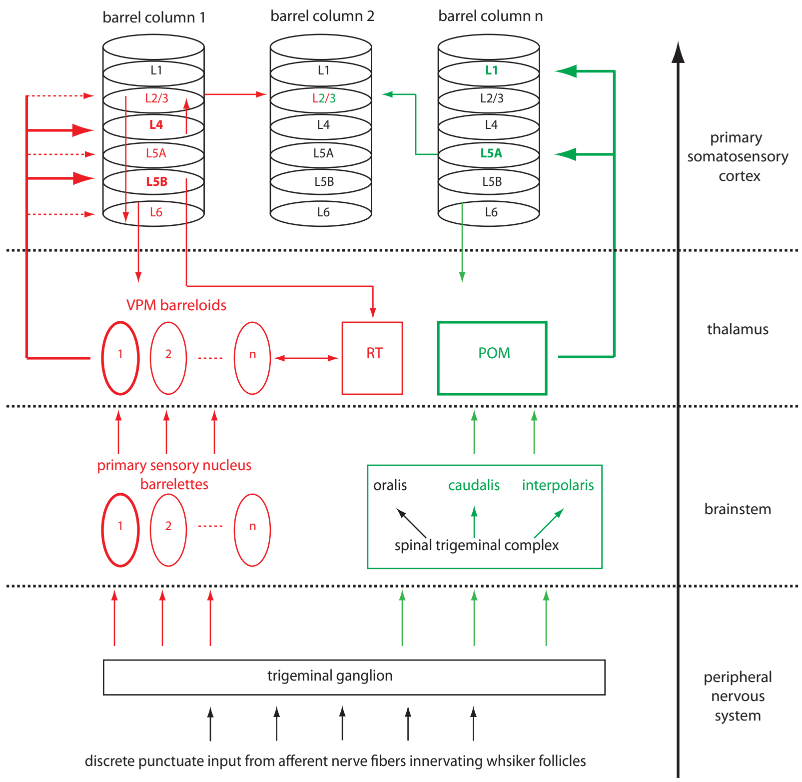

Figure 1.5: **Scheme of lemniscal and paralemniscal pathways.** *The lemniscal pathway (red) transmits sensory input from a single whisker via clear anatomical maps: from barrelettes in the primary sensory nucleus of the brainstem, to corresponding barreloids in the VPM, up to corresponding barrel columns in S1. The main thalamocortical input via this pathway arises in L4 barrel and L5B neurons. L4 conveys this input to L2/3 neurons, which in turn spread the excitation to the entire barrel cortex and to the main cortical output layer L5B. L5B and L6 are further involved in a corticothalamic feedback loop giving input to the VPM/POm and nucleus reticularis (RT). The related inhibitory feedback loop between RT and VPM regulates the strength and precise timing of the thalamocortical VPM input. The paralemniscal pathway (green) processes multiple-whisker information. Clear anatomical maps are lacking for this pathway: from the spinal trigeminal complex interpolaris and caudalis in the brainstem, to the POm, up the L1 and L5A in S1. L5A in turn conveys this input to L2/3 of the surrounding barrel columns. This pathway is suppressed under anesthetized conditions.*

signaling from the periphery, via the nucleus interpolaris and caudalis of the brainstem, POm in the thalamus, up to barrel and septal regions in S1. There, the major input addresses L1 and L5A.

However, the above presented anatomical description of the whisker information pathways is so far rather qualitative and any quantitative description, especially in three dimensions, is lacking and will therefore be subject of this work. Here, I will mainly focus on the lemniscal pathway from one barreloid in the VPM to its corresponding barrel column in S1. By quantitatively determining the number and 3D distribution of neuron somata in VPM and S1, classifying postsynaptic excitatory cell types in S1 and reconstructing the presynaptic innervation of VPM axons, the number and subcellular distribution of thalamocortical VPM synapses for every postsynaptic neuron will be estimated.

1.2.2 Functional organization of the barrel cortex

During *in vivo* experiments, sensory input into the barrel cortex arises from different kinds of stimuli. First, controlled deflection of a single whisker under anesthesia (a passive touch for the animal) results in strong cortical sensory responses. Extracellular recordings, by introducing an electrode into S1, allows for direct measurement of stimuli evoked suprathreshold activity (APs) of individual neurons [10]. This data suggests that the AP activity, evoked by passive touch, is well aligned with the anatomical barrel map, but differs significantly between different cortical layers (Fig.1.4).

Sensory information related to passive deflection of a single whisker arrives in the S1 barrel column foremost via the lemniscal pathway, namely by the dense excitatory thalamocortical innervation of neurons located in the corresponding VPM barreloid. Strong inhibitory feedback from the RT to the VPM sharpens the timing of the sensory input to the cortex [11], [12]. As first-order approximation, a single deflection therefore evokes a

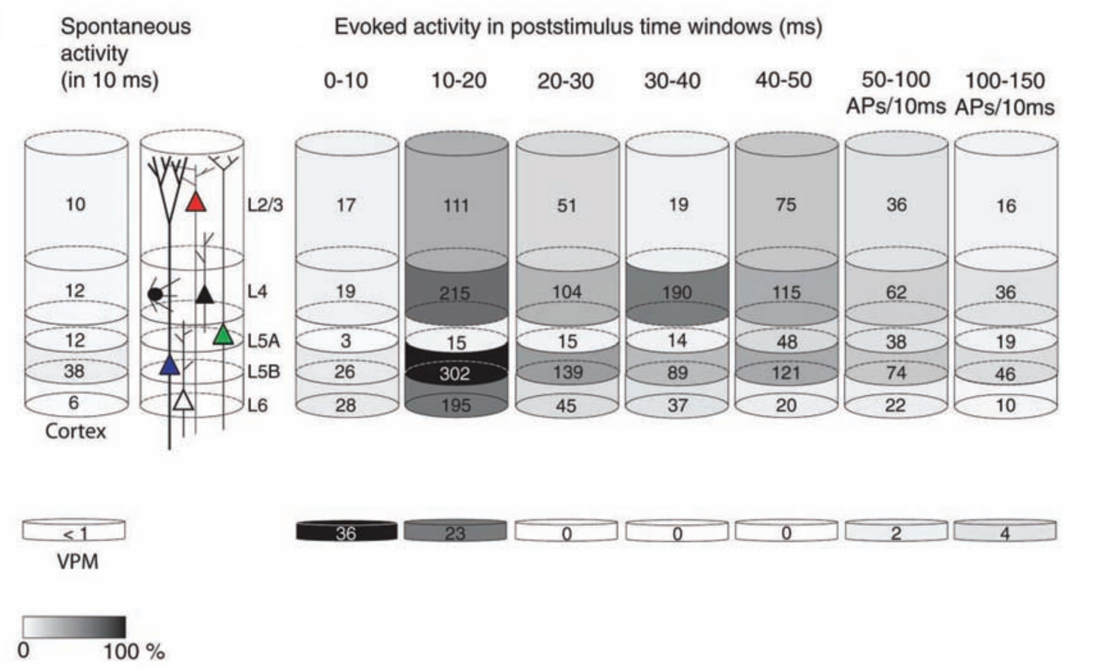

Figure 1.6: **Layer- and cell-type-specific suprathreshold activity in a barrel column.** *The number of APs per layer of a cortical column was derived by extracellular recordings in anesthetized rats, before (spontaneous activity) and after (evoked activity) passive deflection of a single whisker. The average number of APs per cell was multiplied with estimates for the total number of cells per layer. The barrel column is activated by approximately 60 thalamic APs fired within 20ms after deflection. The strongest response to passive deflection arises in L5B and L4. Figure adopted from [10].*

nearly synchronous volley of 50-70 APs in one barreloid, which is mainly conveyed to L4, L5B and L6 of the corresponding barrel column. The fast 10 fold increase in suprathreshold activity in these layers (Fig.1.6) is hence primarily and directly caused by synchronously active thalamocortical synapses [12].

L4 barrel neurons have dendritic and axonal arbors laterally confined to a single L4 barrel [13], [14], [15], and the thalamic input arriving in L4 will therefore largely remain confined to the barrel for the initial step of cortical processing [7]. The excitatory L4 axons prominently innervate L2/3 in the immediately overlying area. In contrast, axonal arbors of such L2/3 pyramidal neurons extend well beyond the boundaries of a single barrel column [16]. Being activated upon whisker deflection, either directly by VPM innervation or indirectly by L4 neurons, these excitatory neurons hence depolarize cells widely distributed across the barrel cortex. In addition, L2/3 cells form a prominent input to L5. L5 hence integrates excitatory synaptic input from VPM, L5, L4 and L2/3, and is thought to be the main cortical output layer, projecting into subcortical regions like the PONS and the striatum.

Using voltage-sensitive dye imaging (VSDI) [18] the described spread of activity can be directly monitored at millisecond temporal and subcolumnar spatial resolution. By rapidly changing its fluorescence linearly with respect to the membrane potential, VSDI is further very sensitive to subthreshold changes. The earliest response evoked by brief passive deflection of a single whisker occurs after ∼10ms and is highly localized within its corresponding barrel column (Fig.1.7)[17]. This is in very good agreement with the suprathreshold measurements (Fig.1.6).

However, during the following milliseconds the response increases in amplitude and propagates horizontally to cover a larger fraction of the barrel cortex. This suggest that the more localized suprathreshold activity reflects the ”tip of the iceberg” of a large and distributed subthreshold activity [19], involving many cortical neurons and multiple local microcir-

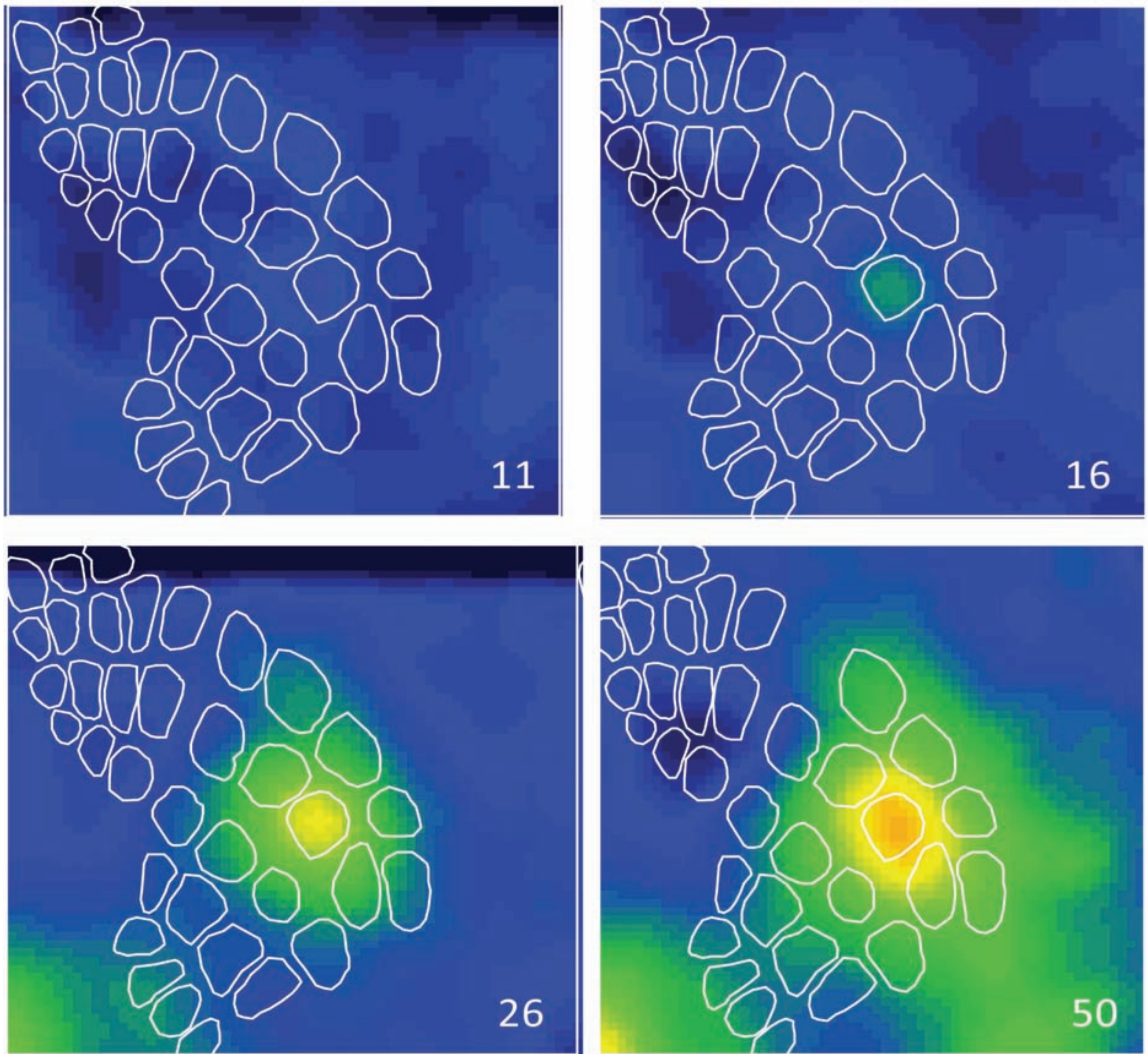

Figure 1.7: **Spreading of subthreshold activity in barrel cortex.** *By injecting a voltage-sensitive-dye (VSD) the spread of activity after passive deflection of a single whisker can be monitored with ms time resolution and subcolumnar spatial resolution. The first activity arises ∼10ms after the stimulus and is laterally confined to the anatomical barrel boundaries. During the following milliseconds the activity spreads to the surrounding columns, but the peak amplitude remains in the barrel column. Figure to some extend adopted from [17].*

cuits.

In summary, passive deflection of a single whisker in the anesthetized animal results primarily, although not exclusively, in sensory processing within a functionally well-defined cortical barrel column and can be described (in a simplified way) by an excitatory synaptic circuit from VPM to L4 barrel to L2/3 to L5 [20]. This pathway will subsequently be referred to as the cortical lemniscal processing pathway.

A second kind of stimulus arises when the whisker touches an object during active whisking in the awake animal (an active deflection for the animal). In addition to the canonical cortical lemniscal pathway, there are numerous other important synaptic connections that are likely to be involved in information processing during active touch. In contrast to passive touch, where L4, L5B and L6 neurons are dominantly activated, L4 and L5A cells show the strongest response to active touch [21].

Since the paralemniscal thalamocortical pathway from the POm mainly innervates L1 and L5A, L5A seems to be the starting point of a paralemniscal cortical pathway [7] that is coactive to the lemniscal cortical pathway when the animal is awake. It is currently of great interest to determine the functional interactions between these different synaptic networks and how they contribute to different aspects of whisker-related sensory perception [7].

To address this question a description of the paralemniscal cortical pathway, similar to the one of the lemniscal cortical pathway (VPM → L4 → L2/3 → L5) needs to be done. In cooperation with Dr. Christiaan P.J. de Kock (VU Amsterdam) and Dr. Alexander Groh (TU Munich) I started this by reconstructing both POm and L5A axons. As previously shown, POm axons innervate L1 and L5A, whereas L5A axons innervate L2/3 [22], [23]. However, reconstructing the full three-dimensional extend of L5A axons, it will become obvious that these cells project specifically into L2/3 of multiple surrounding barrel columns. L2/3 is hence subjected to lemniscal and paralemniscal processing streams, which indicates that lemniscal and paralemniscal pathways converge within S1 and are not as separate as in subcortical areas [24], [25].

Summarizing the anatomical and functional organization of the whisker system, the separation into single-whisker (lemniscal) and multi-whisker (paralemniscal) pathways is reflected in every brain region, including the barrel cortex, that is involved in processing whisker-related sensory perception. Apart from being constituted of anatomically distinct excitatory circuits (Fig.1.5), these pathways reflect functionally different contexts. Whereas the paralemniscal pathway seems to be inactive in the anesthetized animal, the lemniscal pathway is active during active touch in the awake and during passive touch in the anesthetized animal.

In the here presented work I will mainly focus on the anatomy and connectivity of the thalamocortical lemniscal circuit (VPM → S1) and briefly on the starting point of the cortical paralemniscal pathway (L5A → L2/3). The three-dimensional reengineering of these functionally important microcircuits will potentially allow for *in silico* experiments, that will shed light on the mechanisms of activation of a cortical column by passive touch or spreading of activity during active touch.

1.2.3 Whisker-related behavior and plasticity

Apart from its clear anatomical and functional correlation with a single whisker, another important reason to investigate whisker-related sensory processing in rodents, is to gain insight into the basis of decision making in mammalian brains. Sensory information serves to guide behavior and sensory processing can therefore be viewed as the starting point for motor control and the planning of future actions [7].

In the laboratory, rodents can learn to use their whiskers to perform various behavioral tasks. One example is the detection of edge locations. Shown by [26], [27], [28] rodents can use their whiskers to reach across a gap between two platforms (Fig.1.8). If reaching the other side, the animal reliably jumps over the gap and receives some reward (e.g. sweet milk). If the two platforms are too far apart, the animal will refuse to cross this gap. Moreover, this gap-crossing behavior can be performed with a single intact whisker.

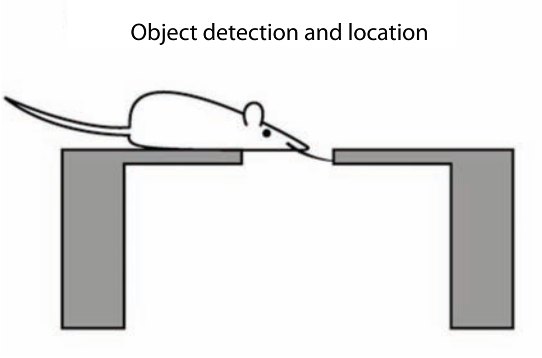

Figure 1.8: **Learned whisker-related behavior.** *Edge detection and location forms the basis of the gap-crossing task. A rodent must reach across a gap with its whiskers to locate a target platform where a reward is placed. The decision to cross the gap or to remain in the home platform depends on the gap size. If the animal cannot touch the other side, it will never jump. The decision is reliably made even upon a single touch by a single whisker. Figure adopted from [7].*

This situation is achieved by acute whisker removal (trimming), which means clipping off the whisker hairs near the skin surface, without damaging the follicle. Whereas whisker trimming within the first five days after birth results in an abnormal organization of the barrel field, trimming in adult animals does not alter the barrel pattern [7]. Nevertheless, compared to untrimmed animals, VSDI and extracellular recordings reveal decreased activity in barrels corresponding to removed whiskers and increased activity in barrels corresponding to remaining intact whiskers. The mechanisms underlying these functional or anatomical changes, in general termed plasticity, are yet unknown.

However, notably no trimming effects are observed in thalamic neurons. This is strong indication that plastic changes occur at the level of thalamocortical synapses and/or in the local cortical circuitry [7]. By reconstructing thalamocortical axons from barreloids corresponding to either trimmed or intact whiskers, in cooperation with Dr. Randy M. Bruno (Columbia University, NY), I will show that whisker removal in adult rats results in a significant pruning of VPM axons.

In consequence, the tools designed to reengineer a three-dimensional average cortical barrel column will not only yield possibilities to study synaptic mechanisms underlying simple whisker-evoked behaviors, such as decision-making, but will further help to understand plasticity effects on neuronal networks after deprivation or injury of sensory organs.

Chapter 2

Methods

A cortical barrel column contains many thousand neurons of various types and thalamocortical, as well as intracortical axons can spread over some cubic millimeter volumes, reaching a total length of several centimeters. Hence, a quantitative three dimensional reengineering of such large functional neuronal networks and circuits will hardly be achieved by manually counting, reconstructing, classifying and interconnecting neurons.

Using newly available mosaic/optical-sectioning confocal and widefield microscopy, in combination with powerful computing hardware and custom designed software, I developed methods to quantitatively derive all anatomical data necessary to reengineere average *in silico* networks.

The first tool, NeuroCount, automatically extracts the midpoint positions (landmarks) of histochemically labeled fluorescent neuron somata from large three dimensional confocal image stacks. Further, in combination with cell-type-specific markers, the fraction of individual neuronal types among all neurons can be obtained. Here, the number and three-dimensional distribution of excitatory and inhibitory neurons in all six cortical layers of S1 and the single layered thalamic VPM will be presented. As stated above, this data is an ultimate prerequisite for reconstructing the lemniscal thalamocortical pathway of the rat whisker system.

The second tool, NeuroMorph, allows for a semi-automated tracing of both dendrites and axons, from *in vivo* labeled single neurons, using transmitted light brightfield microscopy (TLB). By measuring the properties of the TLB imaging system and of the cortical tissue, a compensation of optical aberrations by deconvolution becomes possible and guarantees an authentic and reliable detection of usually too faint axons next to intensely stained dendrites.

Here, I will present representative samples of excitatory dendrite morphologies from all cortical layers as well as thalamocortical VPM and intracortical L5A axon morphologies. Registering these tracings to standardized column dimensions will then allow for statistical analysis and classification of neuron anatomy.

Finally, the third tool, NeuroNet, combines results from the two previously introduced methods and yields realistic anatomy and connectivity of neuronal microcircuits. Here, starting with the average three dimensional soma distribution of each cortical layer in S1, an average standard barrel column is built up with reconstructed and classified excitatory dendrite morphologies. By superimposing thalamocortical VPM axon tracings, the three dimensional axo-dendritic overlap with each neuron population is calculated. By estimating the number of synapses per axonal length, NeuroNet will finally yield an estimate of the absolute number and three dimensional distribution of VPM synapses for each excitatory neuron.

In summary, the subsequently presented tools result in an *in silico* network model of approximately 15200 realistically distributed full compartmental excitatory cortical neurons, which are synaptically connected to about 285 thalamic neurons in the corresponding VPM barreloid. This model network anatomically resembles the thalamocortical lemniscal pathway, which is involved in processing of sensory information from a single whisker, both in the anaesthetized and awake rat. Animating this cortical column *in silico* with thalamocortical input, measured *in vivo*, will potentially allow to gain understanding of cortical information processing and ultimately show how cortical output can trigger simple whisker related behaviors, such as the decision to cross a gap.

2.1 3D counting of neuron somata

As previously described in [29], the estimation of absolute numbers of neurons, densities or rates of density change in neuron populations is usually based on random, sparse sampling methods [30], [31] such as stereology [32]. These methods determine cell densities by inspecting a representative sub-volume of tissue and extrapolating the obtained density values to a reference volume. Usually these density values are given with an accuracy of about 10% [33] for large anatomical units, such as primary visual (V1), somatosensory (S1) or motor cortex (M1). However, deviation between densities in previous studies is much larger. For instance in V1 a variety of densities values is reported (40000 [30], [34], [35], 52000 [33], 75000-80000 [36], [37] neurons per cubic millimeter). It is hence difficult to determine density changes within or between neuron populations, or across functional sub-units, such as the cortical column. In consequence, it would be favorable to count the absolute number of neurons in large volumes and hence derive the detailed three dimensional neuron distribution of the brain area of interest. In case of the cortical barrel column such a volume should be around 0,5mm x 0,5mm x 2mm (0.5 cubic millimeter [38]) in order to avoid edge artifacts.

Recently available three-dimensional imaging techniques (mosaic/optical-sectioning confocal laser scanning microscopy) and suitable neuronal stains opened new possibilities for the determination of neuronal densities within entire volumes. Neuronal stains, like NeuN [39], [40], [41], [42] labeling all neuron somata, or GAD67 [43], [38], [44], [45] labeling GABAergic interneuron somata, as well as genetically encoded labels of specific neuron populations in transgenic mice [46], allow in principle the quantitative determination of density differences between neuron populations at high level of detail (e.g. between or within cortical layers).

Several neuron counting and detection methods have been reported, both manual and automated ones. The obvious disadvantage of manual neuron detection, apart from possible subjectivity, is the amount of time needed for neuron counting. In consequence, automated accurate detection and segmentation of neurons from microscopic images has been extensively studied [47]. In general, these algorithms can be divided into three categories: threshold-based [48], [49], watershed-based [50], [51], [52], [53], [54] and model-based approaches [55], [56], [57], [58].

None of the three automated algorithm categories yield satisfying results for the here presented sample data. This is due to the fact that model-based methods have comparatively better specificity in detecting the targets, i.e. such methods find all objects satisfying the model-shape but only those. In contrast, threshold- or watershed-based approaches display relatively better detection sensitivity, i.e. they find all objects, but usually result in incorrect numbers [47], e.g. for our sample data, touching, densely clustered neurons are counted as one, resulting in about 20% less neurons.

Here, I present an automated 3D neuron counting approach, developed in cooperation with Vincent J. Dercksen (Zuse Institute Berlin (ZIB)), that combines all three approaches to a novel high-throughput system for detection of neuron somata [29]. The system is described on the example of confocal image stacks of NeuN-labeled neurons from S1. The slightly adapted method for co-localization in multi-channel images is described on the example of NeuN neurons counterstained with GAD67. This allows to measure the fraction of GABAergic interneurons among all neurons [38].

The presented processing pipeline consists of three steps: pre-processing, morphological and model-based filtering. The goal of the first threshold-based step is to create a binary image, separating foreground (i.e. stained neurons) from background. It consists of a number of image processing steps, including compensation for imaging or staining artifacts such as bleaching, shading or uneven uptake of the stain. This threshold-based approach is usually not sufficient to detect the true number and position of neurons. High neuron densities and limited microscope resolution result in clusters of neurons that cannot be separated by the local threshold step. The first processing step is therefore regarded as a pre-processing step that guarantees a similar input to the second (watershed-based) and third (model-based) processing steps. The implementation of the latter two steps is independent of the data type.

In the second watershed-based step, clusters of neurons which are connected by narrow links are separated by a morphological filtering process, resulting in an image of distinct watershed regions (3D objects of connected foreground voxels, identified by a label number), and ideally representing individual neurons. Some clustered neurons appear however like a single, large and uniformly stained neuron. The morphological filters are not capable of splitting such clusters into distinct watershed objects.

The third, model-based processing step addresses this problem. It assumes a single dominant neuron population within the image stacks with a Gaussian-distributed neuron (i.e. soma) volume. The mean neuron volume and its variance are calculated from a volume histogram of the watershed regions. Undivided clusters are then split according to their volume, assuming that it has to be an integer multiple of the mean soma volume. An additional advantage of this constraint is that its parameters are not specified by the user but automatically calculated during the image processing. In a correction step, eventually present spatially separated neuron sub-populations with larger mean volumes are investigated and remain unsplit.

I also present an extension of the method to multi-channel image stacks for co-localization of counterstained neurons. Here, NeuN-labeled neurons were counterstained with GAD67 in order to measure the fraction of GABAergic interneurons among all neurons [38].

2.1.1 Sample preparation and imaging

All presented image data was acquired by methods described in detail before [59], [60], [61]. Development and validation of the automated counting pipeline was performed on confocal image stacks of NeuN/GAD67-stained neurons [43], [38] provided by Hanno-Sebastian Meyer (MPI for Medical Research, Heidelberg). These stacks were acquired from 50μm thick physical vibratome sections from brain tissue of adult wistar rats, cut either along the thalamocortical, coronal or a specified tangential axis. Large three-dimensional confocal image stacks were generated by mosaic/optical-sectioning using confocal laser scanning microscopes (SP2 or SP5, Leica Microsystems GmbH, Wetzlar, Germany; Flowview FV1000, Olympus, Japan). SP2 or SP5 images were acquired by 40x (HCX PL APO CS; N.A.: 1.25-0.75; oil-immersion) or 63x (HCX PL APO CS; N.A.: 1.3; glycerol-immersion) magnification objectives, yielding a pixel size of 0.366μm x 0.366μm or 0.232μm x 0.232μm, respectively. FV1000 images were acquired by a 60x (PLAN APO N, N.A.:1.42; oil-immersion) magnification objective, yielding a pixel size of 0.331μm x 0.331μm. Mosaic refers to multiple overlapping 2D images (e.g. 5x5), each representing one microscopic field of view. Sampling along the z-direction during optical-sectioning was 0.6μm.

2.1.2 Manual detection of soma positions

Image stacks containing single mosaic tiles were loaded into Amira 4.0 or 4.1 [62], [63]. Landmarks (3D voxel coordinates) were assigned manually to the center of all stained neuron somata (soma landmarks) during a careful examination of the image planes (optical sections).

Objects at the stack border in the x- or y-direction were always counted. The x/y overlap was set to approximately 5 microns. In consequence neurons at the x/y border (overlap area) of mosaic tiles were detected twice. By aligning the mosaic images, twice detected neuron somata coincide and can be erased. If the mosaic area is chosen larger than the area of interest, x/y border effects can hence be completely neglected.

The x/y border rule is not applied at the z-borders of the image stacks. Here neurons are regarded to be within the image stack if their diameter increases to a maximum value and decreased again or was constant for three more optical sections before reaching the stack border. A detailed description of the manual counting, the validation of the border criteria and the approximate inter-user-variability of 2.1% can be found in [38].

2.1.3 Computing hard- and software

The software and algorithms are custom written in C++ [64]. The raster image file I/O, iteration through a raster image, as well as multiple of the subsequent image filters use the ITK Image Processing Library [65]. The software is executed on AMD dual-core 64-bit Opteron computers, equipped with either 1 CPU and 2 Gigabytes of memory, 4 CPUs and 32 Gigabytes of memory (DELTA Computer Products GmbH, Reinbek, Germany) or 8 CPUs and 64 Gigabytes of memory (fms-computer.com, Netphen, Germany).

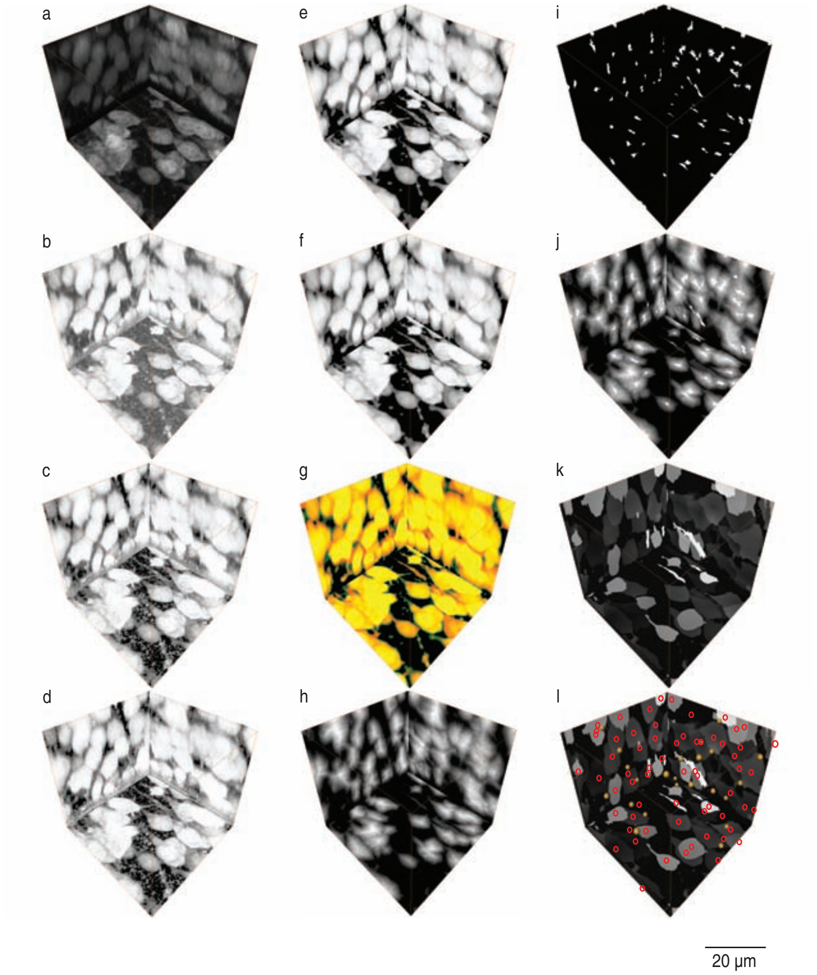

Figure 2.1: **NeuroCount Illustration.** *X/y-, x/z- and y/z-projections of a representative small volume of NeuN-stained somata. (a) original image stack, (b)-(g) pre-processing: (b) local intensity mapping → amplification of weak somata., (c) local lower threshold → reduction of background, (d) hit-or-miss transform → reduction of small isolated noise artifacts, (e) median filter → reduction of noise and smoothing of structures, (f) closing filter → filling of small holes within the structure, (g) cropping filter → structures are cropped from their artificial halos, (h)-(k) watershed-based processing: (h) Euclidean distance transform, (i) regional maxima = markers, (j) grayscale reconstruction → starting basins for watershed segmentation, (k) marker-driven watershed segmentation → individual foreground regions representing individual or clustered somata, (l) model-based processing, splitting of remaining clustered watershed objects according to object volume → set of position landmarks (orange); for illustration: landmark projections (red circles). Figure adopted from [29].*

2.1.4 Threshold-based filtering (pre-processing)

Fluorescent images can suffer from two kinds of artifacts. First, shading or bleaching of the stain, as well as deviating neuron densities, lead to an uneven illumination across mosaic images and usually affect the image acquisition itself. It results in different signal-to-noise ratios (SNRs) across and between individual image planes. The second artifact is caused by uneven uptake of the fluorescent dye, resulting in varying intensity values across individual neurons. The first issue is addressed by subdividing the large mosaic stack into approximately 400μm x 400μm large sub-stacks, overlapping by 5%. The entire processing pipeline is then successively applied to these individual smaller stacks. Each image plane of such a sub-stack is further split into rectangular bricks and processed individually, in order to compensate for local SNR variations within and between the sub-stack planes (see next subsection). The second issue is addressed by processing each three-dimensional object (e.g. neuron soma) individually (see subsection: Removal of artificial halos).

It should be emphasized that the mentioned artifacts are strongly dependent on the imaging instrumentation and the used staining method. If the imaging system incorporates automatic shading correction that reduces deviations in SNR already during the image acquisition, the subsequent filters will not affect the image quality negatively. However, the here presented imaging systems yield no sufficient intrinsic correction and hence the pre-processing is essential for an authentic neuron counting.

Bricking

Uneven illumination across individual image planes prohibits the application of global image operators. Further, illumination deviations between individual image planes limit a general application of 3D image operators. Each image plane (i.e. one sub-stack, ≈400μm x 400μm) is hence subdivided into 2D bricks. In the case of the SP2 confocal microscope at

40x magnification, the optimal bricks size was determined to be 256x256 pixels for a sub-stack that resembles exactly one field of view (375μm x 375μm; 1024 x 1024 pixel). This size was determined by systematic testing and is linearly adjusted for different magnifications, pixel resolutions or sub-stack sizes, in order to guarantee a similar brick area for all kinds of images. Hence, the number of bricks decreases with decreasing magnification (or pixel resolution) and fixed image size.

Intensity mapping

Direct application of a lower threshold operator on each 2D brick, which sets all pixels having a value smaller than the threshold value to zero, proved to be problematic. The SNR is usually too low to set an adequate threshold value that separates somata from background. Hence the intensities for each brick are mapped by a non-linear sigmoid-shaped filter 2.1 [65] onto a new range:

$$I' = \frac{255}{1 + \exp(-(I - \frac{\beta}{\alpha}))}, \tag{2.1}$$

where I' and I denote the new and old intensity (gray) values, respectively. β ideally represents the center and α the width of the neuron's intensity range. This filter progressively attenuates intensity values outside this range and produces a very smooth and continuous transition to the specific intensity range of interest (Figure 2.1b). It results in a per-brick amplification of the neurons with respect to their surroundings (Figure 2.2a/b). Systematic testing yielded an intensity range of neurons that is best described by the following values for α and β:

$$\beta = \mu_{original} + 0.75\sigma_{original}; \alpha = \sigma_{original}, \tag{2.2}$$

where $\mu_{original}$ and $\sigma_{original}$ refer to the mean gray value and standard deviation of each 2D image brick, respectively.

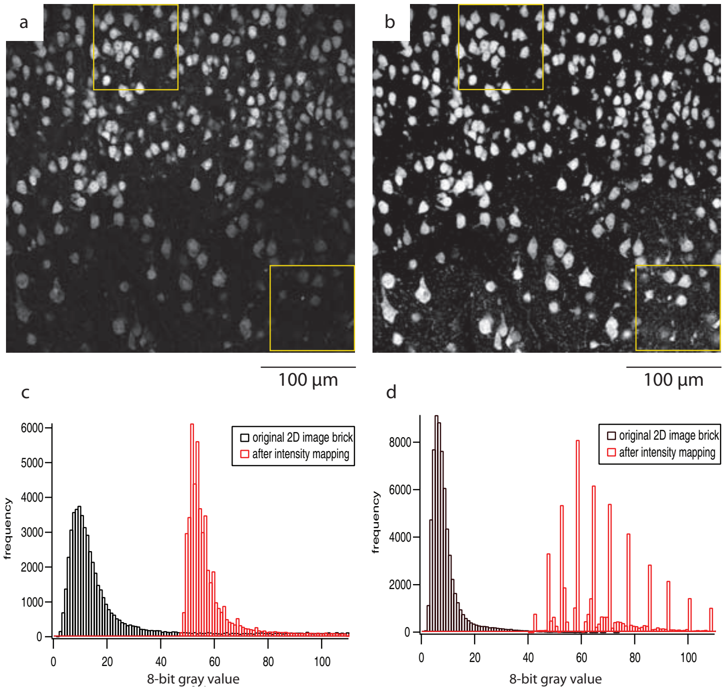

Figure 2.2: **Local intensity mapping.** *(a) Single thalamocortical x/y image plane affected by uneven illumination. The high-contrast in the upper brick results in a broad gray value histogram (panel c; width of black histogram=6.22), whereas the low-contrast bottom brick has a more narrow histogram (panel d; width of black histogram=3.58). (b) Image plane after local intensity mapping. The neurons across the entire plane are of similar intensities. The noise in the prior low-contrast brick is high, resulting in a much broader histogram (panel d; width of red histogram=56.52), whereas the width of the histogram of the high-contrast brick remains more or less unchanged (panel c; width of red histogram=4.36). (c) In high-contrast bricks the intensity mapping leads to amplification of the somata and attenuation of the background. Hence, the lower threshold should be approximately the mean value of the mapped image. (d) In low-contrast bricks the structures and a significant part of the background are amplified, resulting in a broad histogram. Hence, the lower threshold needs to be higher than the mean value after mapping. This is realized by the threshold* t_1 *in equation 2.3. For high-contrast images* t_1 *is essentially* μ_{new} *(here:* $\mu_{new} + 1$*), whereas in the low-contrast case* t_1 *is significantly increased (here:* $\mu_{new} + 17$*). Figure adopted from [29].*

Lower threshold

Once the neurons are amplified with respect to their surrounding, a lower threshold t_1 is applied in order to separate the neuron somata from background:

$$t_1 = \mu_{new} + \frac{1.1}{\sigma_{original}} \cdot \sigma_{new}, \tag{2.3}$$

where μ_{new} and σ_{new} refer to the mean gray value and standard deviation of each 2D image brick after intensity mapping. This thresholding step sets all voxels below t_1 to background, i.e. to value zero. The local threshold function comprises a term inversely proportional to the standard deviation of the image brick prior the intensity mapping. This accounts for possible uneven illumination within each image plane. The width of the intensity distribution ($\sigma_{original}$) can vary significantly from one brick to the next. Two extreme situations occur when neurons are surrounded by low background, resulting in broad intensity distributions (Figure 2.2a, top brick/2.2c), and when neurons are surrounded by background values similar to the neurons' intensities, resulting in a narrow distribution (Figure 2.2a, bottom brick/2.2d). In the latter case, the width of the intensity distribution after mapping will be much larger than the original one ($\sigma_{new} \gg \sigma_{original}$), resulting in an approximate threshold of $t_1 = \mu_{new} + \sigma_{new}$ (Figure 2.2d). In the other case, the two widths will be of similar order of magnitude, resulting in a threshold of $t_1 = \mu_{new}$ (Figure 2.2c). Thus, this filter is capable of discriminating neurons surrounded by high and low background values (Figure 2.1c and 2.2b).

Hit-or-miss transform

The two previous filtering steps result in image stacks of significantly reduced background. However, small "speckle" artifacts are usually still present. The image planes are therefore subjected to a hit-or-miss transformation with rectangular frame masks of increasing size as structuring elements [66], [61]. The transformation is applied to every image plane. Isolated foreground objects that are completely surrounded by a frame are converted to background (Figure 2.1d). Beginning with a radius of one pixel and increasing the frame size subsequently to three pixels, small and isolated artifacts are removed.

Median filtering

In order to smooth the intensity distribution within neurons, a median filter is applied as implemented by the ITK [65]. Each voxel is assigned a new intensity value, which is the median value of its surrounding voxels within a 5x5x5 voxel large neighborhood (Figure 2.1e). The neighborhood size was obtained by systematic testing. This filter is computed in three dimensions because neurons are 3D objects, which consist of 2D planes that may vary systematically in gray values. 2D median filters would not decrease these inter-plane deviations.

Closing transform

Next, a grayscale closing filter [66] is applied as implemented by the ITK [65]. Its geometrical interpretation is that a ”sphere” rolls along the outside boundary of a foreground object (i.e. neuron soma). It tends to smooth contours, fuses narrow breaks, eliminates small holes, and fills small gaps in the neurons (Figure 2.1f). The 3D structuring element (sphere) has a radius of five voxels (approximately 2/3 of a soma radius) and was derived after systematic testing.

Removal of artificial halos

The uneven uptake of stain results in neurons of weak intensities in intermediate neighborhood to neurons with high intensity values. The intensity mapping described above causes amplification of the surrounding of such weakly pronounced neurons and sometimes fuses them with other neurons (”halos” (Figure 2.1g, green)). By removing halos that were introduced by the intensity mapping, the neurons are cropped to their original volume (Figure 2.1g, yellow/orange). This is realized by processing each 3D object of connected foreground pixels individually. For each 2D plane of each object, a lower threshold value t_2 is calculated, defining the foreground for this object plane:

$$t_2 = \mu_{filter} - 1.2\sigma_{filter} + \frac{40}{\sigma_{original}}, \tag{2.4}$$

where μ_{filter} and σ_{filter} refer to the mean gray value and standard deviation of each 2D object plane after the closing filter. The local threshold function comprises a term inversely proportional to the intensity deviation of the 2D object plane $\sigma_{original}$ in the unprocessed image, again compensating for uneven illumination between the bricks as described in subsection ”Lower threshold”. The parameters for the threshold function are obtained by systematic testing. This is the final result of the first (pre-processing) step.

2.1.5 Morphological filtering

The filtering described in the previous section results in a stack of 2D gray value images, which is then transformed into a binary stack by setting all pixels with a gray value different from zero to 255. In the following such stacks will be considered as single 3D binary images. In order to find the total number of neurons in the image, one could simply count the total number of 3D connected foreground objects (groups of connected voxels) in the image. However, the limited resolution of light microscopy imaging systems in addition to high neuron densities results in clusters of neurons that cannot be separated by the pre-processing pipeline. In consequence, direct counting produces total neuron numbers which are generally too low, because a single foreground object may consist of multiple connected

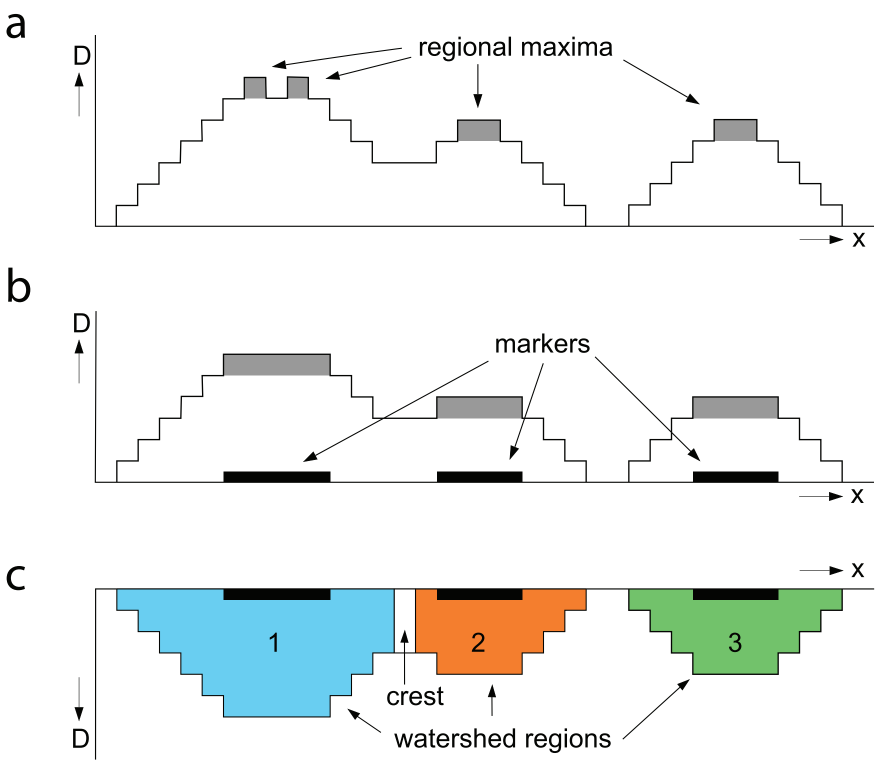

Figure 2.3: **Watershed filtering.** *One-dimensional illustration of the separation of touching somata by marker-based watershed segmentation. Objects containing two (or more) maxima in the distance field separated by a minimum are assumed to consist of two (or more) clustered neurons and need to be separated. (a) Regional maxima of the distance field D. Due to contour irregularities multiple maxima per object may appear (left object), which is undesired. (b) By subtracting 1 from the distance field at the position of regional maxima, and computing the regional maxima of this modified distance field, better markers are obtained. (c) The adopted distance field is "flooded" using the marker positions as initial basins. Positions where the levels from the different watersheds meet, are marked as crest regions. After the flooding is completed, crest regions are turned into background. (D has been inverted to better illustrate the basin flooding metaphor.) As a result, clustered neurons are split at the minima of the distance field, i.e. where the connection between two neurons is thinnest. Figure adopted from [29].*

neurons. Therefore such clusters are divided into their constituent neurons, using a method described by [67]. This method consists of three steps:

- Computation of a distance transform for each 3D foreground object of the binary image.
- Finding exactly one marker for each neuron (i.e. multiple markers for neuron clusters), where marker refers to a single voxel or a group of connected voxels.
- Computation of a watershed transformation, using the markers as initial basins.

Geodesic distance transform

First, a distance transform [66] is computed for each 3D foreground object in the binary image. This results in intensity values for each voxel that resemble the physical Euclidean distance to the closest background voxel. Thus, voxels in the interior of objects have high values, object voxels close to the boundary have low values and background voxels have zero value (Figure 2.1h). These values are computed by repeatedly (binary) eroding [66], [65] the objects in the pre-processed image, successively peeling their outer boundaries. During each erosion step and for each foreground object, the physical Euclidean distance to the prior erosion level is assigned to voxels of the current most outer layer. A 3x3x3 voxel binary cross is used as structuring element for erosion.

Grayscale reconstruction

This second step should ideally generate a single marker for each neuron within a foreground object (Figure 2.1i). One approach to realize this would be to compute the regional maxima of the distance image (Figure 2.3a). A regional maximum M of a grayscale image I is defined as a connected region of voxels with a given value h (plateau at altitude h), such that every voxel in the neighborhood of M has a value strictly lower than h. An efficient method to compute regional maxima uses a morphological operation called grayscale reconstruction [68] as implemented by the ITK [65]. Computing all regional maxima results however in too many markers: some objects have multiple very close regional maxima, due to contour irregularities and discretization artifacts. Usually these markers differ by only one level in the distance function. Therefore such regional maxima are reconnected by subtracting 1 from the values in the distance image at all marker positions and computing the regional maxima (Figure 2.1i) of this modified distance function (Figure 2.3b).

Watershed segmentation

The final step uses the set of markers M to assign the set of foreground voxels belonging to each neuron. These neuron regions are found using a procedure called marker-driven watershed segmentation. The general watershed algorithm uses intensity information to divide a gray value image into foreground regions (catchment basins), separated by watershed lines (background). This algorithm can be illustrated by a landscape flooding metaphor. The inverted distance image $D' = -D$ can be regarded as a landscape where the minima of D' correspond to valleys (Fig 2.3c). When this landscape is flooded, the water level starts to rise from the valleys (or catchment basins) until the different basins meet at the watershed lines (or crests). Afterwards, each basin corresponds to one of the desired neuron regions and is bounded by the watershed lines and/or the image background. The marker-driven watershed segmentation ensures that one obtains exactly one region for each marker, by creating an input image D^* adapted from D' such that

1. its only regional minima are located at the marker positions and
2. its only crest-lines are the highest crest-lines of D' that are located between the minima (marker positions)

The image D^* is then flooded as in the general watershed case. For details I refer to [67]. Further, the flooding algorithm described in [69] was chosen to efficiently find the neurons that correspond to the markers (Figure 2.1k).

2.1.6 Model-based cluster splitting

The preceding processing steps result in individual 3D objects (neuron regions) that represent the neuronal somata within the image stack. However, some clusters of neurons are still not separated because they have similar intensities and are so close to each other in the original image that they appear like a single, almost spherical neuron. To separate such clusters I chose a model-based filter. It is based on the assumption that within each substack there is a single dominant neuron population of neurons with Gaussian distributed volumes and that most clusters could be split by the filters of the first two pipeline steps.

Volume histogram and mean neuron size calculation

Regarding the assumption above, the voxel volume of each watershed region is calculated and results in a histogram of these volumes. The first histogram bin always comprises many small artificial objects. Hence, taking the second peak of the histogram as the mean volume of the dominant neuron population, a Gaussian distribution is fitted to the histogram at this value (Figure 2.4a). The distribution for individual neurons (i.e. not part of a neuron cluster) is parameterized by three values, the mean value, the standard deviation and the peak amplitude (μ_1, σ_1, A_1). Clusters of n = 2,3,..N connected neurons will also be parameterized by Gaussian distributions. Their according mean value μ_n is simply given by:

$$\mu_n = 1.1 \cdot n \cdot \mu_1. \tag{2.5}$$

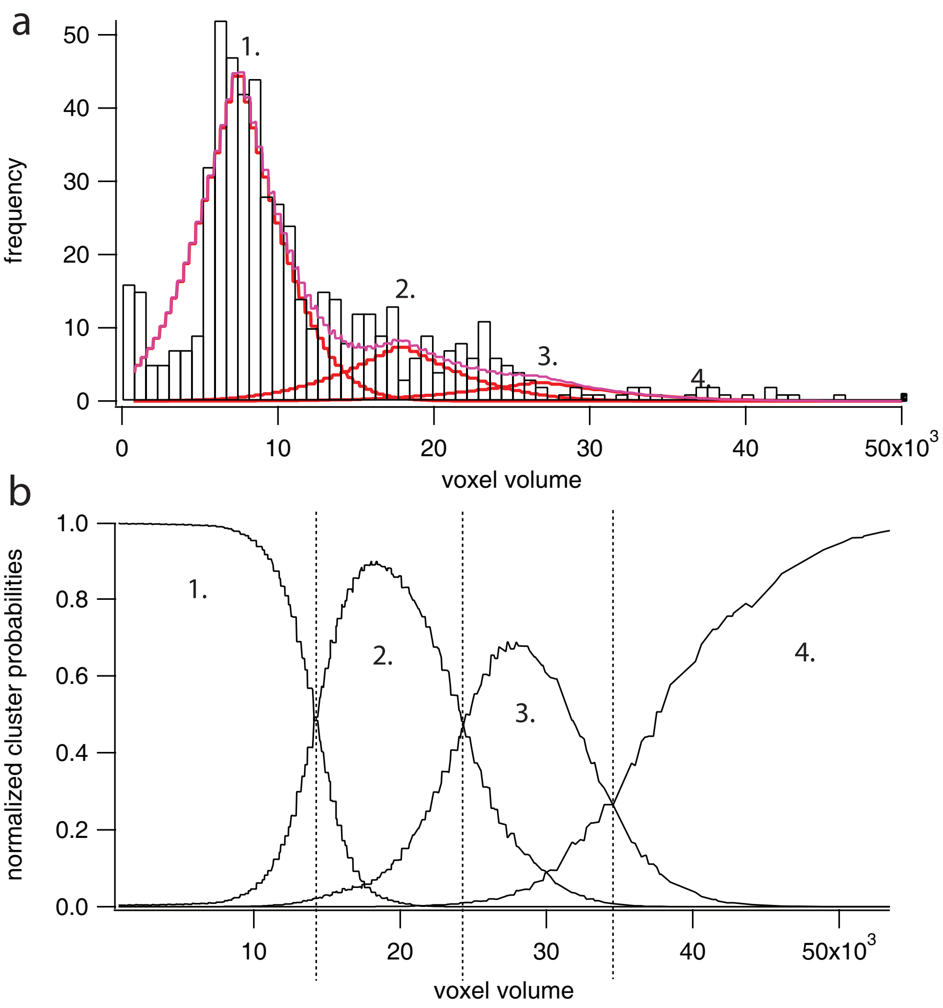

Figure 2.4: **Model-based splitting.** *Volume histogram of watershed objects. The first mode is assumed to reflect the dominating neuron population and is fitted by a Gaussian (red 1). The higher modes are assumed to be integer multiples of the first mode (→ here: 3 more Gaussians representing clusters of 2, 3 and 4 neurons, respectively). The pink plot represents the sum of the four distributions. (b) Normalized probability values for each object volume. According to the above distributions four probability values are calculated for each object volume and normalized to 1. The resulting four plots are shown. The intersections (vertical dashed lines) represent volumes the separate the clusters. Figure adopted from [29].*

The additional multiplication with 1.1 is due to the assumption that the unresolved gaps between the neurons add a small amount to the cluster volume and is derived by systematic testing. The standard deviation for each cluster type σ_n is calculated by standard error propagation:

$$\sigma_n = \frac{1}{\sqrt{n}} \sum_{i=1}^{n} \sigma_i, \tag{2.6}$$

and the according amplitude A_n is calculated by averaging the height of the five bins around μ_n. This is done until the largest 3D region (object) in the watershed image is covered by a distribution (Figure 2.4a).

Evaluation of cluster type

Each watershed object can only belong to a single distribution. Therefore the probability p_{mn} for each object and for each distribution is calculated, where m refers to the object number and n to the n^{th} cluster distribution (number of connected neurons). Each p_{mn} value is normalized to one (Figure 2.4b), resulting in N normalized cluster probabilities for each watershed object.

$$\bar{p}_{mn} = \frac{p_{mn}}{\sum_{n=1}^{N} p_{mn}}. \tag{2.7}$$

Each object is regarded to consist of as many neurons as is its highest normalized probability value. However, objects that are smaller than the mean neuron volume minus twice the standard deviation are considered to be artifacts and are ignored during further processing.

Splitting of clusters by k-means cluster analysis

Once each watershed object is assigned a most likely cluster type (i.e. $n = k = 1, 2, , N$ neurons), the according k reference voxels (landmarks) are calculated, by using a k-means clustering algorithm as implemented by the ITK [65]. The k-means algorithm works as follows:

1. The input for each watershed object are k (= n; i.e. most likely number of neurons in a cluster) initial mean values (default landmarks) specified as k random voxels within the object.

2. Each voxel of a watershed object is assigned to its closest landmark among the k mean values.

3. Calculation of each k-means cluster's mean from the newly assigned landmark voxels within the objects and hence updating the k mean values of a neuron cluster.

4. Repetition of step 2 and step 3 until the termination criteria is met, here if no voxel changes its cluster membership from the previous iteration.

This results in k landmark voxels for an object (consisting of $k = n$ neurons). Each landmark is used as position reference of an individual neuron and a list of these landmark voxels is visualized in Amira [62], [63] (Figure 2.1l).

Correction for 2^{nd} population of larger neurons

The assumption of a single Gaussian distributed neuron volume across the entire image stack can cause miss-counting if two neuron populations of significantly different volumes are present. I therefore assume that there is only a small spatial overlap between these populations and that one of them is dominant. This is a reasonable assumption for the presented sub-image sizes of ≈400μm x 400μm x 50μm. If the minor population is smaller in volume than the majorities' mean volume (i.e. GABAergic interneurons), these neurons will still be counted as one. However, if the minority population consists of large neurons (Figure 2.5) the prior described splitting will result in an overestimation of the neuron

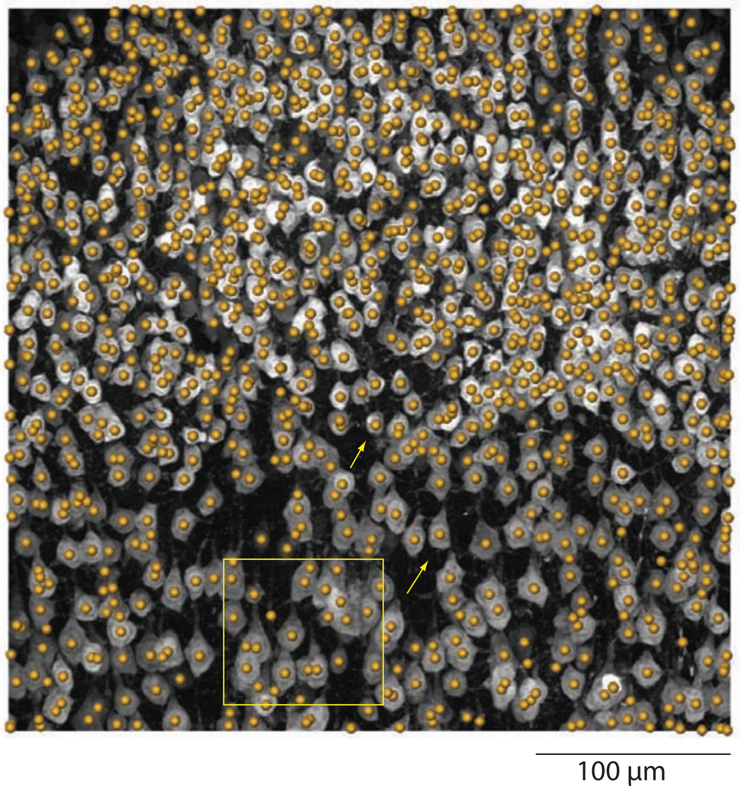

Figure 2.5: **Large neuron correction.** *Maximum z-projection of NeuN-stained confocal image stack. The yellow box represents the volume shown in Figure 2.1. This stack is from an area of S1 where L4 neurons (upper part) overlap with larger L5 neurons (lower part). Even though two neuron populations with significantly different volumes are present, the correction algorithm avoids miscounting (e.g. neurons indicated by arrows). Figure adopted from [29].*

density.

This issue is addressed by evaluating the local surrounding of each watershed object before model-based splitting. If more than 10% of the watershed objects in a surrounding box of 300 x 300 x 100 voxels have the same cluster probability (larger than 1), the object will not be split (Figure 2.5). This filter also corrects for systematic errors of the pre-processing step. In bricks with low SNR the neurons are slightly enlarged compared to bricks of high SNR. If significant SNR gradients are present within the image stack, the systematic increase in volume in low SNR bricks can lead to an artificial second neuron-type. This means that the neuron volume in some regions of the image can be systematically larger compared to the original image stacks. This effect is also compensated by the described correction filter.

2.1.7 Colocalisation

NeuN reliably labels all neuron somata within an image [39]. It is hence possible to counterstain specific neuron-types and to image them simultaneously at a different fluorescent wavelength, acquiring so called multi-channel image stacks. Since all neurons within the NeuN channel are detected by the prior described pipeline, the local surrounding of each landmark voxel is inspected in the other channels. If a neuron is also detected in one of the other channels, not only the position and density of all neurons within the stack can be evaluated, but also the neuron-type can be obtained.

Figure 2.6 shows an example for this procedure. GAD67 positive interneurons were colocalized in a second fluorescent channel (Figure 2.6a/b). The pre-processing of the second channel is again dependent on the staining and imaging techniques. In the case of GAD67, imaged by a confocal laser scanning microscope, immunoreactive GABAergic interneurons show a strong somatic GAD67-signal [43], [38]. However, GAD67 positive synapses will

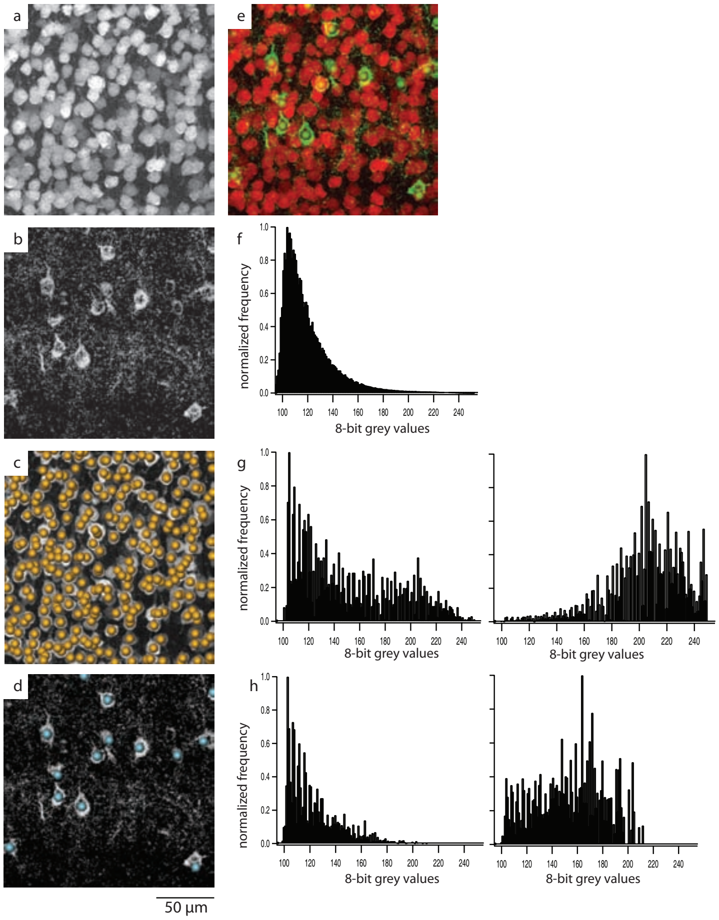

Figure 2.6: **Colocalisation.** *(a) Max x/z-projection of NeuN-stained confocal image stack. (b) Max x/z-projection of GAD67 counterstained image stack. (c) Automatically detected NeuN landmarks. (d) GAD67 positive landmarks generated by evaluating the surrounding of each NeuN landmark in the pre-processed version of b, (e) overlay of a and b with automatically detected GAD67 landmarks (green = counterstained somata). (f) normalized gray value histogram of GAD67 image (g) left: normalized gray value histogram in GAD67 stack around a NeuN landmark position, right: left histogram divided by "background" histogram from f; due to the presence of a GAD67-positive neuron, high gray values are dominant (h) due to the absence of a GAD67-positive neuron, low gray values are dominant → if the divided histogram is dominated by gray values below 150, no GAD67 landmark is assigned; if it is dominated by gray values higher than 150, a co-localized GAD67 landmark is set. Figure adopted from [29].*

also be stained, resulting in small (<10 voxel) bright spots (Figure 2.6b). Hence, the major step of the pre-processing of the GAD67 channel is to get rid of these synapses.

Here, the pre-processing is based upon a gradient magnitude filter [66] as implemented by the ITK [65]. The resultant gradient image is further subjected to an exponential intensity mapping using the following equation:

$$I' = \exp(\frac{\log(256)}{255} \cdot I) - 1, \tag{2.8}$$

where I' and I refer to the intensity (gray) values after and before the mapping, respectively. This mapping effectively attenuates low background values and enhances the synaptic signals. The result is then subtracted from the original image. After these additional GAD67 specific filters, the brick-wise intensity mapping as described before is applied. A final median filter with a structuring element of 1 pixel radius reduces any remaining small artifacts, leaving only GAD67 positive neuron somata (Figure 2.6d).

Figure 2.6f shows a histogram of such a pre-processed stack. Since the fraction of GAD67-positive neurons among all neurons is low (≈15%) [33], the stack histogram is dominated by the background. Figure 2.6g/h show intensity histograms around landmark positions that were generated for the NeuN channel images. Figure 2.6g (left) shows the landmark histogram of the k-mean cluster around the corresponding NeuN landmark in the presence of a GAD67-positive neuron, whereas the k-means cluster of the landmark used for the landmark histogram in figure 2.6h (left) does not contain such a neuron. All histograms are normalized to one and landmark histograms are shifted so that the bin with the maximum number of gray values coincides with the maximal bin of the stack histogram. These matched histograms are bin-wise divided and the resultant ratio histogram is again normalized to one (Figure 2.6g/h, right).

If no GAD67 positive neuron is present at the landmark position, the landmark histogram resembles the shape of the stack histogram, since this is dominated by background. Therefore the divided histogram shows no contribution at high gray values that correspond to foreground (Figure 2.6h, right). In contrast, if a GAD67 positive neuron is present, the amount of foreground pixels is overrepresented in the landmark histogram with respect to the stack histogram. Hence, the ratio histogram shows a significant distribution at high gray values (Figure 2.6g, right). The criterion for co-localization can therefore be defined as a threshold function. If 20% of the object's pixels fall into bins from 150-255 of the ratio histogram the neuron is considered to be present in both channels.

2.2 3D reconstruction of neuron morphologies

As derived above and described in detail before [61], the accurate tracing of single neurons is one prerequisite for the determination of anatomical features of different neuron cell-types required for biophysical modeling of single cells and signal processing in neuronal circuits. Several automated reconstruction approaches have been reported previously. These reconstructions, made with two-photon [70], confocal [71], [72], [73], [74], [75], [76], [77], [78] or brightfield images [79], focus mainly on the dendritic tree and the extraction of geometrical features such as volumes or surface areas of dendrites or spines. Hence, these approaches completely lack a reconstruction of the axonal arbor. The reason is that the axonal branching pattern is more complex and that axons spread over a much larger volume (cubic millimeters) compared to dendrites (a few hundred cubic micrometers). Furthermore, axonal staining is fainter than that of dendrites because of their smaller diameters and greater distance from the soma where a tracer is loaded into the cell. Thus, no successful automated tracing of these widely spreading neuronal projections has yet been reported. The method presented here, was developed in cooperation with Dr. Philip J. Broser (Royal Queen Mother Hospital, White Chapel, London) and focuses on the accurate tracing of all neuronal projections. The dendritic tree and the extensively spreading axonal arbor are traced and reconstructed simultaneously.

Typically the cells are filled *in vivo* with a tracer like biocytin [80]. The brain is then perfused with fixative and cut in sections of about 50-100μm thickness. The current approach for tracing these neurons and their axons in 3D is a manual one, based on the Camera Lucida technique (e.g. The Neurolucida System (MicroBrightField), Filament-Tracer (BITPLANE)). Here, neuronal structures in each section are traced manually. A human user interacts with a microscope that is enhanced with computer imaging hardware and software [79], [81]. The user recognizes patterns and marks neuronal structures on a live camera image displayed on a computer screen. By moving the stage horizontally in x and y and focusing through the brain slice in the z-direction, a progressively larger volume is inspected. The 3D-tracings of neuronal branches from this volume are collected by the computer system interfaced to the camera and result in a 3D-graph representation of neurons.

Manual tracings of dendritic trees are very reliable. The reliability is due to the localized branching pattern and the relatively large diameters ($\approx$2μm-5μm) of dendrites. However, the axonal arbor frequently extends further away from the soma. The average volume that has to be inspected by the user is for most cell-types around 1.5mm x 1.5mm x 100μm per brain section. For accurate tracing, this volume should be inspected in a raster scan order, moving from one field of view to the next and progressively focusing through the specimen.

Using a 40x objective and a standard CCD-camera (e.g. Q-icam (Q-imaging, Canada)), the number of fields of view is around 12000, with an average sampling along the optical axis of 1μm. Since axons can have diameters less than one micron, a 100x objective is usually used for manual tracing. In this case around 77000 fields of view have to be inspected.

Taking a typical cell (e.g. L2/3 pyramidal neuron of rat cortex), which spreads over 10 to 20 brain sections, the number of fields of view that have to be inspected is of the order of $10^5 - 10^6$. Manual reconstruction of axonal branching patterns is hence tedious and time consuming. Therefore, correct manual tracing of axons requires experienced users to reach a reliable level of reconstruction quality.

I present a semi-automatic reconstruction pipeline that traces reliably both dendrites and axonal arbors by extracting their skeleton (approximate midline). In addition the method presented here needs significantly less time compared to manual tracing. The automated tracing is carried out on large image stacks acquired by mosaic scanning [82] and optical sectioning [60] using a TLB microscope. The manual inspection of thousands of fields of view is replaced by the acquisition of a stack of mosaic images. A rectangular pattern of overlapping mosaic tiles (adjacent fields of view) is scanned, covering an area of a brain slice sufficient for the tracing of axonal arbors usually 1.5mm x 1.5mm (Figure 2.7a). The 3D information is obtained via optical sectioning, meaning the recording of such mosaic planes at multiple focal positions that are separated by 0.5μm.

This large 3D image is then deconvolved (see sec. 2.2.3), based on measured optical properties of the microscope, as derived in cooperation with Dr. Stefan Hippler (MPI for Astronomy, Heidelberg) [83]. This guarantees an improvement of SNR and resolution, in particular along the z-direction. A local threshold function that checks for connectivity extracts neuronal structures from the background. The extracted foreground objects are transformed into thinned approximate midlines (the skeleton) and yield a graph representation of dendrites and the widely spreading axonal arbor. The automatically reconstructed branches from serially sectioned brain slices are than manually edited and automatically spliced using custom made software in Amira [62], [63].

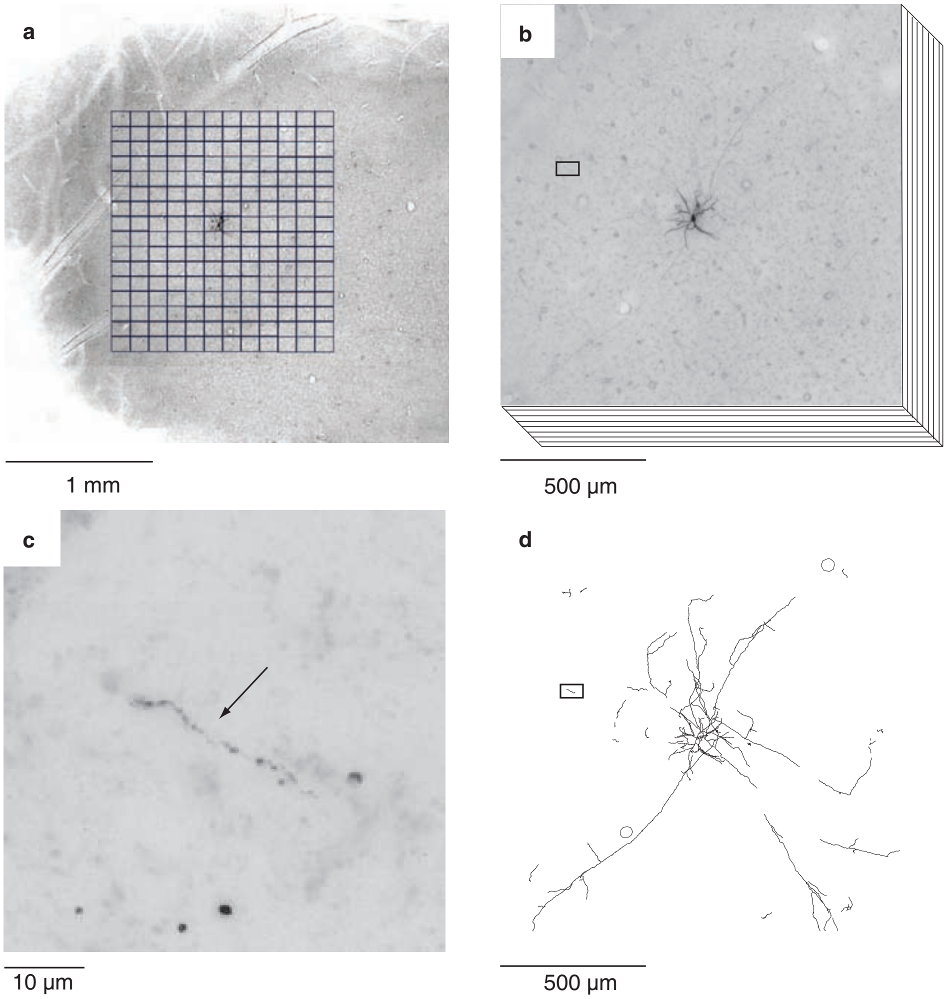

Figure 2.7: **Mosaic microscopy for neuron tracing.** *(a) Overview of a biocytin-filled neuron (L2/3 pyramid) from a brain slice taken with a 100x objective. The black mosaic indicates the scanning area (1,5mm x 1,5mm). A 3D image stack is acquired by mosaic/optical-sectioning. (b) The pattern of overlapping tiles (adjacent fields of view) is stitched to a large 2D mosaic image. Mosaics are recorded for all focal planes separated by 0,5µm, resulting in a 3D stack. (c) Enlargement of the box shown in b showing a faint axonal branch about 1mm away from the soma. This illustrates the requirement to scan large volumes at high resolution. (d) Result of semi-automated reconstruction pipeline. Figure adopted from [61].*

2.2.1 Sample preparation

All cells were filled in Wistar rats (P28 - 31; Charles River Laboratory). Experiments were carried out by Dr. Randy M. Bruno (Columbia University, NY) and Dr. Christiaan P.J. de Kock (VU Amsterdam) in accordance with the animal welfare guidelines of the Max Planck Society.

Cells were filled with biocytin either extracellularly using juxtasomal recording and electroporation [84] or via whole-cell recording [85]. In both cases patch pipettes, pulled from unfilamented borosilicate glass on a Sutter P-97 puller (Sutter Instruments) were used. The outside diameter of the shank entering the brain varied from 25 to 75μm, and the tip opening had an inside diameter less than 1μm.

At least 1h was allowed to pass after cell filling and prior to tissue fixation to insure sufficient diffusion of the biocytin throughout the axonal arbor. The animal was deeply anesthetized and perfused transcardially with phosphate buffer followed by 4% paraformaldehyde. Cortex and thalamus were cut tangentially and coronally, respectively, in 50-100μm thick vibratome sections. Biocytin in these sections was stained with the chromogen 3.3′- diaminobenzidine tetrahydrochloride (DAB) using the avidin-biotin-peroxidase method [80]. Sections were sometimes counterstained for cytochrome oxidase [86]. Processed sections were then mounted on slides and coverslipped with Mowiol (Hoechst, Austria).

2.2.2 Image acquisition

A standard TLB microscope (Olympus BX-51, Olympus, Japan) equipped with a motorized x-y-z stage (Maerzhaeuser Wetzlar, Germany) was used for image acquisition. It can be used for TLB and fluorescent microscopy. In order to obtain monochromatic illumination, if used in TLB mode, a $546nm \pm 5nm$ band pass illumination filter (CHROMA

AF-analysentechnik, Germany) was attached to the diaphragm of the lighthouse. This band pass filter minimizes the chromatic aberrations of the imaging system and simplifies the theoretical description of the optical pathway from a polychromatic to a monochromatic one. The light is transmitted by a high numerical aperture (1.4NA) oil immersion condenser (Olympus, Japan), assuring parallel illumination of the specimen under "Koehler"-conditions [87].

In fluorescent mode, a 100W xenon arc lamp is used with a $470nm \pm 10nm$ band pass filter and a $485nm$ dichroic mirror (Olympus, U-MGFPHQ) to excite the samples. Fluorescent emission is controlled by the dichroic mirror and a $520nm \pm 20nm$ band pass filter. The specimen is imaged by a 100x high numerical aperture oil immersion objective (Olympus 100x U PLAN S APO; 1.4NA) in combination with a 0.5x TV-mount (Olympus U-TV0.5XC-3) or a 40x objective (Olympus 40x U PLAN FL N; 1.3NA) in combination with a non-magnifying TV-mount. The immersion oil has a refractive index of $n_{oil} = 1.516$ similar to glass. In addition the aberrations for a 40x dry objective (Olympus 40x U PLAN FL; 0.75NA) are measured to illustrate the advantages of immersion objectives.

The stage is navigated in three spatial directions by an OASIS-4i-controller hardware and software (Objective Imaging Ltd, Cambridge, UK). It allows the acquisition of large mosaic images [82] at different focal planes. Mosaic in this context refers to a two-dimensional image of overlapping tiles (i.e. adjacent fields of view) that are aligned automatically and then stitched during the image acquisition, resulting in a large composite image (Figure 2.7a/b). The user defined scan area is automatically divided into a series of overlapping fields of view which are called tiles. For each tile location a stack of images is acquired using optical sectioning [60] with a typical separation of 0.5μm between the focal planes. For each focal plane the corresponding tiles are then stitched together, resulting in a three-dimensional stack of two-dimensional mosaic images for each focal position (Figure 2.7b).

This process is executed by the Surveyor Software (Objective Imaging Ltd, Cambridge, UK).

The images are recorded by a "Q-icam Fast" 1394 camera (Q-imaging, Canada), equipped with a CCD chip, which in combination with the 100x objective and the 0.5 TV-mount yields an x/y sampling of 92nm per pixel (116nm per pixel if the 40x objective and a non-magnifying TV-mount are used). Since the illumination is limited to one wavelength, 8-bit gray value images, rather than RGB color images are acquired.

In order to guarantee a similar dynamic range of the gray values for mosaic image stacks from different brain slices and animals, the exposure time of the CCD camera is set semi-automatically by the Surveyor Software. Therefore the mean gray value in a typical field of view within the scan area is calculated and is set to be 210. "Typical" here refers to a field of view without any stained neuron somata or blood vessels. This highly important feature of the image acquisition is the basis for an optimal deconvolution and therefore a robust neuron tracing. However, significant exposure gradients within the scan area are a considerable constraint to this method. Its consequences and the limitations for neuron tracing will be discussed later.

In summary, image acquisition results in a high-resolution 3D mosaic image. The typical image stack size used for neuron tracing is 1.5mm x 1.5mm x 100μm. However, the mosaic pattern can be adjusted to smaller or larger areas. Using the 100x objective in combination with the 0.5 TV-mount or the 40x objective with a non-magnifying TV-mount the sampling is 92nm x 92nm x 500nm or 116nm x 116nm x 500nm per voxel. Hence, the data volume for such a stack is approximately 15-30 Gigabyte.

Despite the fact that the TLB microscope is probably the most widely used instrument in a lifescience laboratory [88] it has one significant disadvantage in comparison to the above mentioned high-resolution fluorescent techniques. Out-of-focus light caused by diffraction effects due to the finite aperture of the objective and aberrations induced by the optical components or the specimen result in a blurred contribution to each 2D image plane. As a consequence the resolution, especially along the optical (z-)axis, is not sufficient to obtain a high-resolution visualization and quantification (e.g. of neuronal morphology) from raw TLB data [88].

The optical limits of the imaging system can be described in terms of its 3D point-spread function (PSF) or its Fourier Transform the optical transfer function (OTF) [87]. The PSF specifies the appearance of an idealized point (delta function) after being imaged by the microscope system. Neglecting coherency effects and noise caused by the CCD camera, the imaging of an object is then given in terms of a convolution of the PSF $s(x, y, z)$ with the object's intensity distribution $o(x, y, z)$ [89], [60]:

$$i(x, y, z) = o(x, y, z) \otimes s(x, y, z), \tag{2.9}$$

where $i(x, y, z)$ refers to the stack of recorded 2D images and the symbol $\otimes$ denotes the convolution operation described in standard textbooks.

2.2.3 Shack-Hartmann-analysis-based deconvolution

According to equation (2.9) image formation could be reverted if the PSF is known. This procedure is called deconvolution or image restoration. The intensity distribution of the object could then be obtained, apart from spatial frequency domains of the OTF that are dominated by noise or at the zero crossing [90]. For any further considerations the noise caused by the CCD camera, which becomes more dominate with low light intensities [91], will be neglected. The camera's exposure time is automatically adjusted to guarantee that stained neuronal processes cover a maximum gray value range and to ensure none-zero background of unstained tissue [61]. Therefore, throughout this section, noise refers to unstained light-absorbing cortical tissue that surrounds stained neurons and does not include the CCD noise which can be problematic in fluorescence microscopy.

It is obvious that the deconvolution result approaches its optimal performance if the applied PSF resembles the properties of the imaging system. Hence, a correct PSF will reduce artifacts from unstained background that are interpreted as noise and consequently improve the quality of an incoherently illuminated wide-field TLB image stack in terms of SNR, where SNR here refers to the ratio between stained neuronal processes and the unstained tissue background. In addition, the resolution will improve significantly, making a high-resolution visualization and quantification of wide-field data possible. In consequence, the correct determination of the microscope's PSF is essential.

Several theoretical [92], [93], [94] and experimental [95], [96] methods have been described to obtain the 3D PSF of a microscope. A common approach is to measure the PSF by recording a series of 2D images of a sub-resolution object with different amounts of defocus, where sub-resolution refers to an object whose dimensions are smaller than the diffraction limit [87] of the microscope's objective. Fluorescent objects (beads) of this size yield a weak signal that requires an extremely sensitive detector and limits the axial range over which the PSF can be measured [97], [98], [96]. When the optical influences of the tissue need to be investigated, this method is exceedingly difficult [88] for two reasons. First, the fluorescent bead needs to be inserted into the tissue making its signal even fainter, and second it is laborious to measure the PSF for every single preparation.

The alternative, application of a theoretically modeled PSF for deconvolution, is also delicate. Significant discrepancy has been noted between theoretical and experimental 3D PSFs. The difference results in part from inaccurate choice of parameter values (e.g. unknown refractive index of tissue), or the theoretical model assumes ideal imaging conditions, e.g. the absence of any aberration [89].

Since a correct description of the imaging system in terms of its PSF is not trivial and both, theoretical and experimental approaches seem to be not satisfying, alternative solutions have been suggested. The "blind deconvolution" approach [88] uses a nonlinear, iterative and constrained maximum likelihood estimation (MLE) algorithm that requires the PSF not as an input parameter, but reconstructs the PSF concurrently with the image data. However, it is arguable that this approach is only applicable for rather small image stacks (one or a few fields of view), because application of this filter on large image stacks with high resolution has severe limitations.

First, iterative algorithms are strongly influenced by the estimation of the background intensity [99]. An underestimation of background intensities will make the constraint ineffective. This results in a performance similar to that obtained by linear restoration algorithms. An overestimation of the background is problematic, since it results in clipping of the object intensities. Usually, TLB image stacks of the above described dimensions yield neither a uniform background nor can it be assumed that structures dwell in similar intensity ranges throughout such volumes. These inhomogeneous conditions influence the background estimation negatively and result possibly in a loss of performance. Examples for this phenomenon will be illustrated in the result section.

The second limitation is a rather practical one. An 8-bit image stack of the size of 1.5mm x 1.5mm x 100μm with a sampling rate of 0.116μm x 0.116μm x 0.5μm comprises a data volume of approximately 20 Gigabyte. Even on a multi-core server computer a MLE deconvolution carried out by Huygens Professional 2.9 deconvolution software (Scientific-Volume-Imaging, 1995-2007) takes around 24 hours, whereas a linear, non-iterative filter needs only around 45 minutes.

In the work presented a method for fast deconvolution of large mosaic image stacks is described. It combines the experimental determination of aberrations caused by optical components and specimen with a modeled PSF that assumes ideal imaging conditions. The optical system was sought to be optimized by minimizing the aberrations induced by its optical components and the cortical tissue, here 100μm thick cortical slices from rat brains. Further, it was experimentally verified that it is possible to obtain nearly ideal imaging conditions. Once these imaging conditions are achieved, the complex process of image formation is simplified by reducing the optical pathway to a single refraction and a single diffraction event. Refraction occurs at the interface between the specimen and the immersion medium, which fills the space between the tissue and the objective lens. Diffraction arises at the finite entrance pupil of this objective lens. Further it is shown that the modeled PSF describes sufficiently accurate the image formation for this combination of specimen and microscope. Therefore a linear, non-iterative deconvolution algorithm already yields significantly improved image quality and resolution.

To verify that the degree of aberrations is indeed negligible and constant for similar specimens (e.g. brain slices from different animals and different cortical depths), aberrations are measured by analyzing the deformation of a plane wave front behind the optical system using a Shack-Hartmann (SH) wave front sensor [89]. The samples were either fluorescent beads in Mowiol or beads between two slices of tissue, also embedded in Mowiol. The resultant measured wave front function is essentially the OTF [89]. It yields the amount of aberrations induced by the optical components or the tissue for the two sample types, respectively. This measurement allows then the determination of the average refractive index of the specimen.

The major advantage for using a SH sensor for PSF measurement is that the bead size is not limited by the diffraction limit of the objective [89]. Therefore a larger (e.g., 10μm diameter) and hence brighter bead can be used which allows the measurement of the PSF over a larger axial range (10μm) even when the bead is embedded within cortical tissue.

Finally it is shown that the modeled PSF, which is based on measured aberrations that are of a negligible amount, describes the optimized (TLB) imaging system quite well. A high resolution visualization and quantification of neuronal morphology from linearly deconvolved mosaic data is hence possible.

Shack-Hartmann wave front measurement

The aberration function W, which represents the deviation of the measured wave front from a plane wave, can be expanded as a power series in exit pupil polar coordinates [87], [89]):

$$W(\rho, \theta) = A_{lnm} \rho^n \cos^m \theta, \tag{2.10}$$

where ρ represents the normalized pupil coordinate, θ is the angle between the pupil and the field vectors and l, m, n are integers [87]. Due to rational symmetry conditions and neglecting of off-axis aberrations, the expansion is limited to $l + n = 0, 2, 4...$ and $m = 0$, respectively. Therefore the aberration function reduces to two terms when expanded to the 4^{th} order and when the 0^{th} order term is ignored, assuming incoherent illumination:

$$W(\rho, \theta) = A_{020} \rho^2 + A_{040} \rho^4 \tag{2.11}$$

The coefficients A_{020} and A_{040} are expressed in micrometers and represent the wave front deformation caused by defocus and spherical aberration, respectively. These coefficients are measured during the SH wave front analysis. For a detailed derivation of how the SH analysis is related to the wave front coefficients see [89].

An illustration of the wave front measurement experiment is shown in Figure 2.8. The SH sensor and the aberration measurement unit are implemented within a "Wavescope" (Wavescope Model WFS-01, Adaptive Optics Association, Inc.; USA). It comprises a 32x32 array of square micro-lenses (focal length: f=3.5mm, micro-lens spacing: d=300μm) to

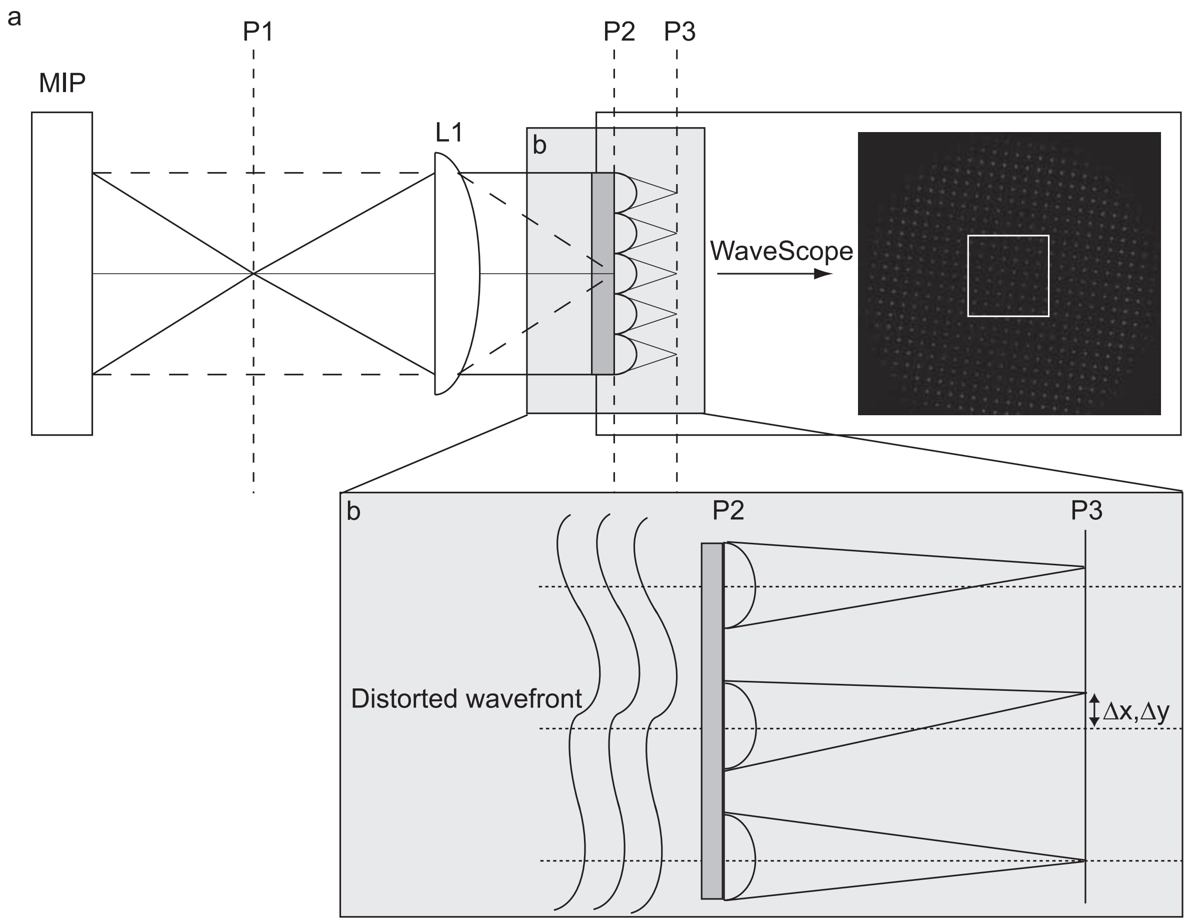

Figure 2.8: **Shack-Hartmann wavefront measurement.** *(a) The wavefront in the microscope's image plane (MIP) is created by fluorescent beads that are embedded in Mowiol and is relayed by a plano-convex singlet (L1) onto the array of micro-lenses (P2) of the SH sensor. The spot displacements within the according spot image are compared with the spot image of a plane wave created by a laser. The "Wavescope" measures these spot deviations and relates them to the coefficients of a power series that expresses the aberration function. (b) Principle of the SH wavefront sensor as shown in [89]. Each lenslet forms an image that is displaced from the local optical axis by an amount ($\Delta x, \Delta y$). The displacement from the local optical axis is determined by the average slope of the wavefront over the lenslet area and the focal length of the lenslet array. Figure adopted from [83].*

sample the wave front in the exit pupil of the microscope as piece-wise planar wavelets and an optical relay system that guarantees correct illumination of the implemented CCD camera. The "Wavescope" measures the displacement of spots created by each micro-lens with respect to a prior calibrated reference spot-image of a plane wave. It further calculates the coefficients of the aberration function. Coefficients are manually scaled to match the normalization, as presented above.

To relay the sample image distribution from the microscope's image plane (MIP) on to the micro-lens array of the SH sensor (P2), a plano-convex singlet (L1) with a focal length of f_{L1}=40mm was used and located 40mm behind the MIP. Hence, this lens provides the SH sensor with a collimated and de-magnified sample distribution of the exit pupil. A grid of 7x7 micro-lenses was always illuminated, independent whether the light was supplied by a bead or a laser. This 7x7 grid (Figure 2.8) was used for the wave front measurements.

Before recording through-focus SH-images of a bead, the SH sensor was calibrated with a monochromatic plane wave. A single mode glass fiber that was connected to a laser (emission wavelength 632.8nm) was therefore located at the MIP, 40mm in front of the plano-convex collimator lens (L1). By temporarily placing a shear plate within the light beam between the collimator lens and the lens array, collimated illumination of the SH sensor could be monitored. The resulting SH reference image defines the imaging properties of the SH sensor, if the exit pupil wave front is described by a plane wave. It accounts for any on-axis aberrations introduced by the sensor optics. Off-axis aberrations can reasonably be neglected due to the size of the micro-lenses [89].

To measure the aberrations caused by the microscope's optical components, a sample with a fluorescent bead embedded in Mowiol was centered in the field of view of the microscope. Through-focus SH images were then recorded at 0.5μm axial intervals over a range of 10μm, between the in-focus position of the bead and the coverslip. To improve the SNR, 100 frames were recorded and averaged at each focal position, using an integration time of 60ms per frame. For measuring additional optical influences on the light beam caused by the tissue, the same measurement was repeated for a bead sample that was placed between two layers of tissue. These measurements were repeated for eight beads respectively.

Simplification and modeling of image formation

As indicated above, the modeling of the image formation within a TLB microscopy is not trivial due to the partially coherent illumination [87] of the specimen. However, considerations about propagation of mutual coherence within a TLB microscope [100], [101], [102] showed that the OTF can be characterized by the ratio of the effective NAs of the condenser and the objective (i.e. ratio between the radii of the entrance pupil of the objective and the illuminating source (microscope field stop)). It is hence possible to model the OTF for the coherent limit (ratio = 0.1), the incoherent limit (ratio $\approx$ 1) or any intermediate partially coherent case (e.g. ratio = 0.5) [102]. These three settings are illustrated by Figure 2.9a-c on the example of one x/y-plane of a stained neuron. The arrows in Figure 2.9a and b indicate coherency artifacts from out of focus planes. The presented imaging system is always adjusted to meet "Koehler conditions" [87], resulting in an effective NA ratio of 1.0 (Figure 2.9c). The microscope then approximately satisfies the theoretical incoherence criterion [102]. In consequence, the high contrast images generated by our imaging system are assumed not to suffer from coherency effects. Hence, the TLB imaging system is treated as if incoherent light originates at the specimen, i.e. the image formation is modeled as in the case of a fluorescent microscope.

However, inverting the gray values and hence treating the TLB like a wide-field fluorescent microscope, the question remains of how to determine the optical properties of the imaging components or the tissue, in order to derive the correct PSF of this system. The simplest

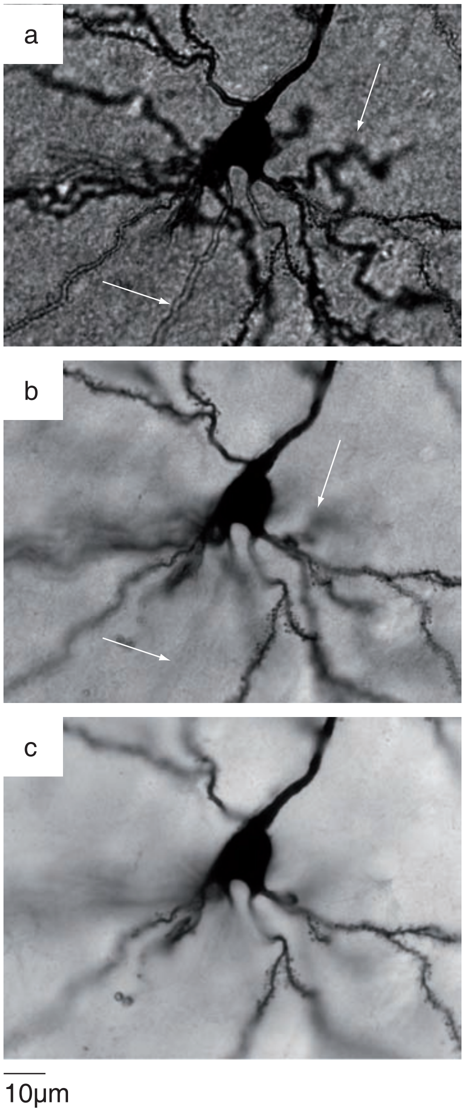

Figure 2.9: **Degree of coherence in TLB images.** *The degree of coherence depends on the ratio of the effective NAs of the imaging system. For illustration an x/y-plane of a neuron imaged by a TLB microscope is shown for three different ratio configurations (0→0.5→1), showing the coherent (a) and incoherent (c) limit, as well as an intermediate case (b). The degree of coherence increases with decreasing NA ratio. Coherency effects result in out-of-focus artifacts as indicated by the arrows in a nd b, which are absent in the incoherent limit (c). It is therefore justified to treat incoherent TLB images like a fluorescent one by inverting the gray values. Figure adopted from [83].*

solution is to assume ideal imaging condition. This means, assuming that neither the optics nor the specimen introduce any aberrations to the path of light. Image formation can then be reduced to a 3D diffraction at the finite entrance pupil of the objective [87], [92]. However, because of the refractive index mismatch between the embedding ($n_{mowiol} = 1.49$) and the immersion medium ($n_{oil} = 1.516$), this simple model is not sufficient. Figure 2.10 shows a geometrical model for this configuration [103]. Since the coverslip and the objective lens have the same refractive index as the immersion oil, these components can be optically neglected. Image formation can hence be reduced to the refraction at the interface between the embedding and the immersion medium and to the diffraction at the finite entrance pupil of the objective lens. This model is implemented in the Huygens software. The parameters are the two refractive indices, the emission wavelength and the effective

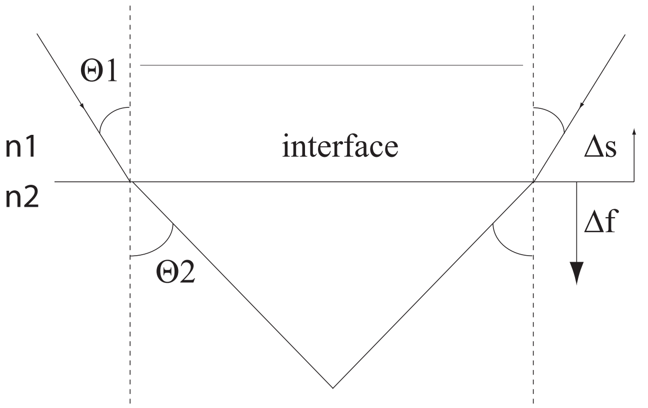

Figure 2.10: **Simple imaging model.** *Simple geometrical model of the refraction at the interface between a homogeneous specimen (n_2) and an immersion medium (n_1) which fills the space between the specimen and the objective's entrance pupil. It relates optical (Δf) and mechanical (Δs) defocus and hence allows the derivation of the specimen's refractive index. The angles are slightly exaggerated for illustration. Figure adopted from [83].*

NA of the objective.

All of these are known for beads embedded in pure Mowiol. However, the cortical tissue could influence the image formation by causing aberrations due to inhomogeneity of the refractive index. To estimate the possible influences of the tissue the following model is used. It assumes that neurons keep their original refractive index, which is approximately $n_{plasma} = 1.35$, and that they can be simplified to spherical somata. The remaining tissue (e.g. extra-cellular space) is assumed to adopt the refractive index of Mowiol. Therefore neurons are treated like convex lenses with an average radius of 10μm in a homogeneous environment of Mowiol. The focal length of these neuronal lenses is then given by:

$$f_{cellbody} = \frac{r}{2} \cdot \frac{1}{n_{mowiol} - n_{plasma}}. \tag{2.12}$$

Therefore, according to Figure 2.11 the length difference between a diffracted and a non-diffracted light beam (Δl) would be approximately:

$$l = \sqrt{l_0^2 + r^2 and \Delta l} = l - l_0. \tag{2.13}$$

This simple model yields that the wave front deformation Δl is about 1.37μm and therefore already about 2.5 times the wavelength, assuming the light penetrates only one soma within the image stack. It is therefore required to show that neuron somata do not function as spherical lenses and to prove that the influence of the tissue is negligible, in contrast to the above estimation. Otherwise the simple "refraction plus diffraction" model could not be applied. In the result section this will be described. Further, the average refractive index for the cortical tissue from rat brains is determined. For the subsequent sections on deconvolution this "refraction plus diffraction" model will always be applied.

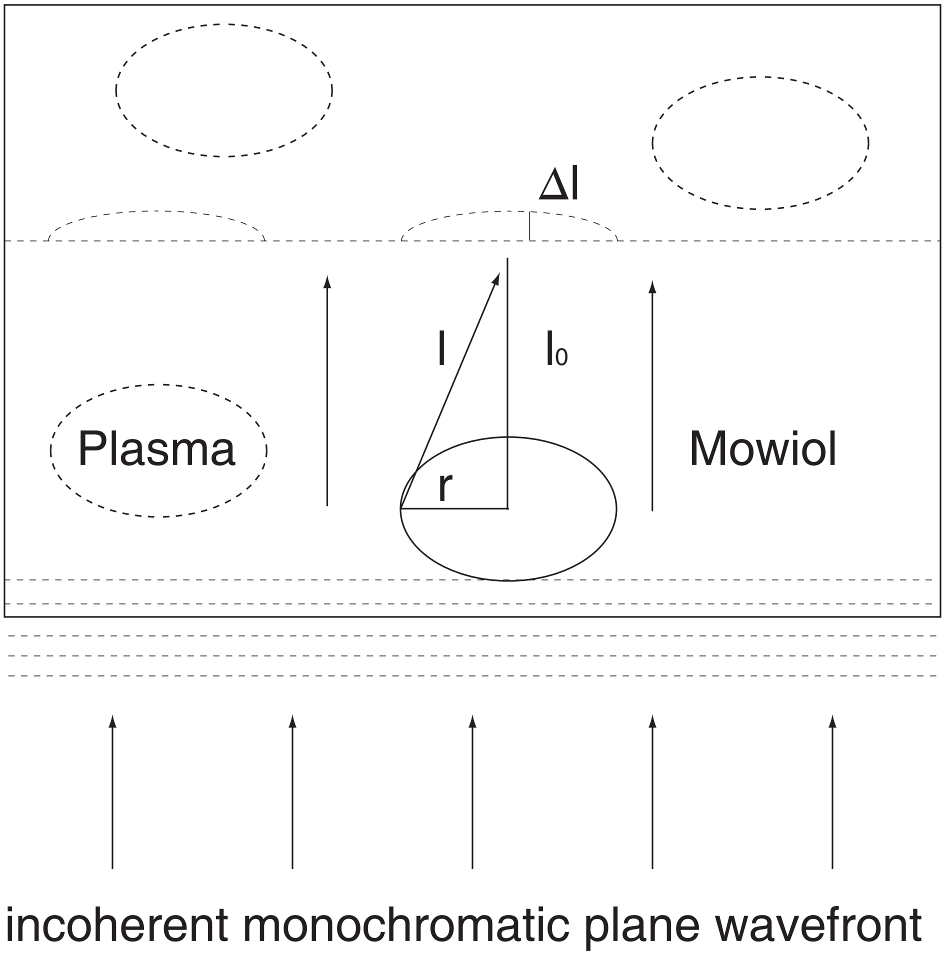

Figure 2.11: **Simple aberration model.** *Simple model illustrating effects of neuron somata on deformation of a plane wave. If neurons keep their original refractive index, they would function as convex lenses within an environment of Mowiol. This would cause deformations of the wavefront and would hence lead ta a significant amount of position dependent spherical aberrations. Figure adopted from [83].*

Deconvolution algorithms

Treating the TLB microscope like a fluorescent one and reducing the complex process of image formation to refraction at the interface between embedding and immersion medium and to diffraction at the finite aperture of the objective's entrance pupil, the Huygens software is able to model a PSF. This PSF can then be applied by various algorithms to the inverted mosaic image stacks. Here, a linear Tikhonov/Miller (TM) filter and a non-linear, iterative MLE filter are used. Both of them are already implemented in the Huygens software. However, since Huygens cannot process a 25 Gigabyte image stack in one run and estimation of a single background value for such a large volume is rather impracticable, the mosaic image stacks are split up into by 100 pixels overlapping "bricks" with a lateral size of 3100 x 3100 pixels. Thus a background value is estimated for each brick.

In contrast to the MLE filter, the image restoration filter of Tikhonov and Miller has no constraints and yields a result after a single deconvolution step. The MLE algorithm ensures non-negative solutions and needs various iterations before it converges or meets a user defined stop criterion. It is further strongly influenced by the background estimation, making the algorithm ineffective when the background is underestimated or causes a severe performance loss if the background is overestimated. More details about these algorithms and their properties can be found in [104], [99], [105].

Deconvolution samples and resolution measurements

In order to verify that the assumptions about ideal imaging conditions, incoherent illumination and a homogeneous refractive index of the tissue are correct, biocytin labeled neuronal processes (dendrites and axons) within mosaic TLB stacks from the cortex of six different rats and at different cortical depths are investigated.

First it was checked whether the results from the SH analysis about an homogeneous refractive index of the tissue are confirmed by an alternative approach. This is done by comparing the theoretically determined angle of the light cone of the modeled PSF with light cones from 15 dendrites and 15 axons, arbitrarily chosen from various locations and depths within the raw image stacks. These cones were further checked for z-dependence and symmetry with respect to the optical axis and the focal plane.
Second, the SNR and the lateral (x/y) as well as the longitudinal (x/z) half-widths are measured from 22 dendrites and 36 axons. This measurement is performed for the raw images and their deconvolved counterparts. These measurements were performed on stacks either containing only dendrites, only axons or both types of structures in intermediate neighborhood. Since axons are usually fainter and thinner than dendrites, the influence of the background estimation for such ”mixed” stacks will become important.

2.2.4 Computing hard- and software

Here, the data size is in general between 15 and 30 Gigabyte per section. Therefore, as in the case of NeuroCount, a fast image processing pipeline based on multi-processor-computing that can handle such large data sets was developed. Again, the algorithms are written in C++ [64] and the raster image file I/O, iteration through a raster image and several filters use the ITK [65]. The algorithms were parallelized by applying the OpenMP standard [106]. They are executed on AMD dual-core 64-bit Opteron servers, equipped with either 4 CPUs and 32 Gigabytes memory (DELTA Computer Products GmbH, Reinbek, Germany) or 8 CPUs and 64 Gigabytes memory (fms-computer.com, Netphen, Germany). Once the mosaic image stack has been saved to disk, a software-demon (a custom written ”Perl” script) detects new data on the hard drive and starts the processing pipeline. Additional image stacks are added to a queue and processed sequentially. The script initiates the subsequent image processing steps, inversion of the gray values, subdivision into bricks, deconvolution, down sampling and finally the 3D neuron tracing (Figure 2.12). Therefore the automatic tracing routine can run 24 hours a day, since the queue of scanned image stacks is sequentially processed. The next step needing user interaction is the manual post-processing of the final 3D reconstructions.

2.2.5 Automated image processing

A major feature of image acquisition is the semi-automated setting of the exposure time of the CCD camera to control the image histogram as described previously. This feature is critical to the downstream neuron tracing algorithms. Their parameters were adjusted and systematically tested to derive the best possible tracings from such images.

Maximum down-sampling

After deconvolution, the data size is reduced to facilitate further computationally intensive steps. Maximum down-sampling is applied for each deconvolved image brick in the x and y plane. Two neighboring voxels are merged to one voxel, computing their maximum gray value. Since this procedure is done in both lateral directions (x and y), the data set is reduced in size by a factor of four. Since neuronal structures are local intensity maxima, all branches will be conserved.

As a consequence the new lateral sampling is 184nm x 184nm per voxel if the 100x objective in combination with the 0.5 TV-mount is used or 216nm x 216nmn per voxel if the 40x objective in combination with a non-magnifying TV-mount is used. Therefore the sampling in both cases is still below the physical resolution limit (approximately half the wavelength; $\approx$232nm) according to the Rayleigh criterion [87].

The down-sampled 3D image bricks are now subjected individually to segmentation algo-

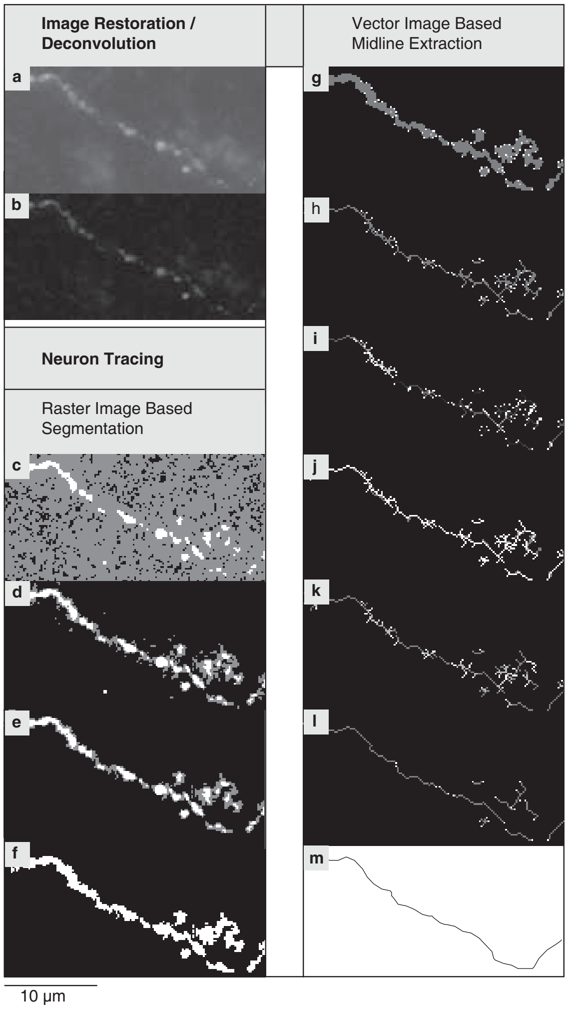

Figure 2.12: **NeuroMorph illustration.** *(a) Max z-projection of inverted image stack cropped from the mosaic image shown in Figure 2.7b (box), showing a weakly stained, fragmented axon. (b) Max z-projection after TM deconvolution. (c) Local threshold function 1: intermediate voxels are shown in gray. (d) Local threshold function 2: intermediate voxels are assigned to fore- or background. (e) Hit-or-miss transform: removes small and isolated artifacts. (f) Dilation/Closing: smooths foreground objects and fuses narrow gaps. (g) Setting of end-line locations: local maxima after distance transformation. (h) Iterative layer-by-layer thinning. (i) Determination of loops in the thinned graph. (j) Removal of loops. (k) Pruning of short branches. (l) Final result of the automated pipeline. (m) Final result of NeuroMorph by manually editing and splicing. Figure adopted from [61].*

rithms (Figure 2.12). The purpose is to separate voxels that represent neuronal structures from voxels that are part of the background.

Local threshold filtering

A target image with the dimensions of a deconvolved image brick is created and initialized with gray value zero. The voxels of the deconvolved bricks are then separated into three groups.

One group, below a lower threshold is set to background (gray value zero in the deconvolved brick). A second group of voxels belonging to potential neuronal structures, with values above an upper threshold, is assigned as foreground (gray value 255 in the target image). The foreground consists of disjoint voxel regions which will be referred to as foreground objects. Voxels with values between the two thresholds form the third group of intermediate value voxels. The intermediate voxels are tested for local features defined by a local property function, to decide whether they belong to foreground objects or to background.

The lower threshold is determined by calculating the intensity distribution of the deconvolved image brick. The deconvolution produces a thin unimodal histogram with the background clustered near zero, structures in the high range, and some remaining intermediate gray values. The lower threshold is taken as the histogram's mean value plus 1.5 standard deviations (STDs). This gray value is usually between 1 and 15. It was derived after systematic testing and essentially deletes the background noise from unstained tissue.

The upper threshold assigns the prominent and most intense structures to foreground. The value of the upper threshold is determined by calculating the histogram of the maximum z-projection of the deconvolved image brick. The upper threshold is then taken as the mean value plus 3.0 STDs. Systematic testing yielded that this is the best value to detect dendrites, well-filled axons and the prominent parts of fragmented filled axons (Figure

2.12c). This upper threshold usually has a gray value between 30 and 60. The remaining voxels between the background (1-15) and the foreground (30-60) margin are referred to as the intermediate voxels.

The local property function comprises two steps. First each intermediate voxel is set as the center of an 11x11 voxel mask in the x/y-plane and the mean intensity of the voxels, regardless of group (background voxels were already set to zero), within this 2D neighborhood is calculated. If the centered intermediate voxel has a gray value that is larger than this mean intensity plus an epsilon value of 5 gray values, it is set to an intermediate gray level of 125 (Figure 2.12c) in the target image. Otherwise it is set to background (gray value zero in the target image). The optimal value of epsilon was derived by systematic testing. The group of intermediate voxels consists usually of isolated artifacts or dim bridges between bright structures. These dim bridges are often found between axonal boutons (swellings of the axon that are likely sites of synaptic contact) and should therefore be part of the foreground. The resultant target image comprises three gray values: 0, 125 and 255 for background, intermediate and foreground voxels respectively.

The second part of the local property function inspects the intermediate voxels of the target image for connectivity to a foreground object. Systematic testing suggested that an intermediate voxel is set to foreground if 10% of the voxels from a 17x17 mask in the x/y-plane centered on this intermediate voxel are part of a foreground object, otherwise it is set to background (Figure 2.12d).

Hit-or-miss transformation

The application of the above local threshold filter results in a binary image. This is then subjected to a hit or miss transformation [66] with rectangular frame-masks of increasing size as structuring elements. The transformation is applied to every image plane. Isolated foreground objects that are completely surrounded by a frame are eliminated to background. Beginning with a radius of 1 voxel and increasing the frame size subsequently to three voxels, small, isolated artifacts that were introduced by the linear deconvolution are removed (Figure 2.12e).

Dilation and closing

Next dilation and closing filters [66] are applied. The dilation filter bridges gaps between the axonal boutons that have not been closed by the local threshold filter. Finally a closing filter as described before is applied (Figure 2.12f). It tends to smooth sections of contours and fuses narrow breaks as well as long thin gulfs, eliminates small holes, and fills small gaps in the contour [66]. The 3D structuring element (sphere) for the closing and dilation has a radius of three voxels. Larger radii could result in a fusion of objects that should not be connected, and smaller radii would have no significant effect on the foreground objects. The radius of three therefore proved to be the best compromise after systematic testing.

Object labeling

The brick-wise segmentation yields binary image stacks. Regrouping of these segmented bricks leads to a binary 3D image stack with the dimensions of a down-sampled mosaic image stack. This large 3D binary stack is subjected to an object labeling algorithm. Once a foreground voxel is detected, a region growing algorithm [66] fuses all connected foreground voxels to a sub-region and assigns a unique integer label. The binary image is thus transformed to an image of N individually labeled sub-regions, each representing a foreground object. Labeled objects are sorted according to their number of voxels. The largest foreground object is labeled as number one, and the smallest object is assigned number N. The background voxels are labeled as zero.

Raster to vector image conversion

Since the neuron occupies only a small fraction of the scanned image volume, the 3D raster image representation requires inappropriately large data storage. A more sophisticated vector data folder is created that stores only foreground objects but keeps the 3D information of the image. The voxels of each foreground object are replaced by vectors, hereafter called compartments. Each compartment stores the three-dimensional coordinates of the prior voxel and can store additional morphological information, such as local properties (e.g. radii, surface distance).

Furthermore, each compartment is linked to its neighboring compartments by inter - compartmental smart-pointers, which allow access of neighboring compartments (e.g. top-left, bottom, left, etc.). Therefore the implicit neighborhood representation by voxel coordinates of the 3D raster image is mapped to an explicit neighborhood construct in the compartment representation. The neighborhood pointers between the compartments preserve the 3D topology of any object. Fast navigation through the object is possible using these inter-compartmental smart-pointers. The compartments representing one object are grouped in a ”double linked” list, which guarantees fast access to each compartment. Therefore the 3D raster image of N labeled foreground objects is converted to N compartment lists. This transformation replaces the 3D raster image of labeled foreground objects by a ”double linked” list, where each list item represents one of these disjoint foreground objects by a list of topology preserving compartments (vector image representation).

Vector image based midline extraction

Representing objects by their main structure or skeleton (approximate midline) is a commonly used technique in image processing. A fast and reliable way to calculate the skeleton of an object is thinning. Generally, thinning is a layer-by-layer (boundary compartment)

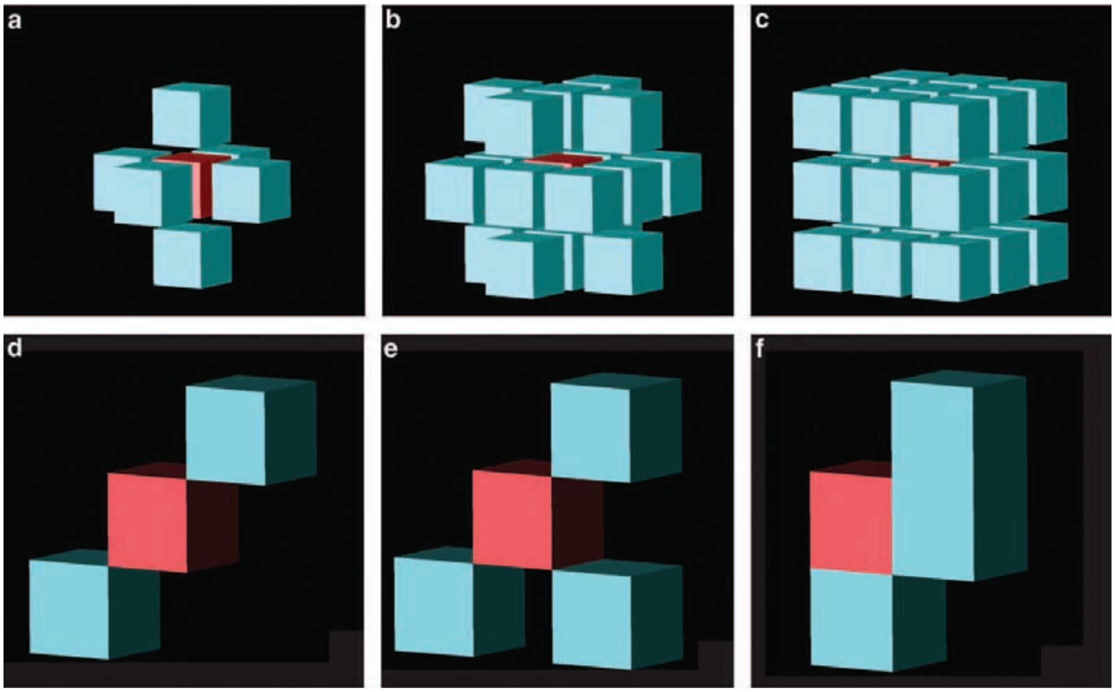

Figure 2.13: **Voxel neighborhoods.** *Panels a-s show different neighborhood topologies in 3D images. Compartments (voxel representatives) are visualized as boxes with edge length 1, centered on their position in image space. The central compartment is shown in red, neighboring compartments in cyan. (a) The six-adjacent neighborhood (N6). Compartments are N6 if they share a face with the central compartment. (b) The 18-adjacent neighborhood (N18). Compartments are N18 if they share at least one edge with the central compartment. (c) The 26-adjacent neighborhood (N26). Compartments are N26 if they share at least one point with the central compartment. (d)-(f) Examples of neighborhood templates for thinning. Removal of the center compartment in f preserves the connectivity (→ simple compartment), which is not the case for d and e. Figure adopted from [61].*

erosion until only a unit-width skeleton is left [107], [108], [109]. Therefore three different classes of compartment topologies are defined: 6-adjacent (N6), 18-adjacent (N18) and 26-adjacent (N26) [108]. Two neighboring compartments are N6 if their Euclidean Distance is equal to one, N18 if their Euclidean Distance is between (or equal to) one and square root of two and N26 if their Euclidean Distance is between (or equal to) one and square root of three [109] (Figure 2.13).

A thinning algorithm has to obey the following demands that are derived from a 2D definition by [110]:

1. Connected objects must thin to connected line structures.
2. The thinned lines should be minimally 26-connected. Two compartments are 26-connected if they are connected by a chain of N26 adjacent compartments.
3. Approximate end-line locations should be maintained.
4. The result of thinning should approximate the midlines of the structures.
5. Extraneous short branches introduced by thinning should be minimized.

To address these demands a template matching algorithm described by [111] is used. It is one of the most efficient thinning algorithms and can be briefly summarized as follows. First a set of end-line locations is determined, necessary to represent the topology of the object. The end-line locations will not be removed. All other compartments, starting from the object boundary, are tested to check whether or not their removal affects the 26-connectivity of the object (Figure 2.13). If compartment removal has no affect on the connectivity, this compartment is termed simple.

In order to determine whether a compartment is simple or not, its N26 neighborhood is compared with all possible N26 neighborhood templates that preserve local connectivity

(Figure 2.13). If the compartment neighborhood matches one of these templates, the removal of this compartment will not affect the local connectivity and the global connectivity will be preserved as well [111]. Hence, this compartment is assigned to be simple and is removed. Whether or not a compartment is simple or not may change after deleting compartments. Therefore the algorithm is iterative and finishes when no more compartments are removed. The implementation of this thinning approach is described in detail below.

Detection of end-line locations

The end-line locations are determined by calculating the compartment, which is most distant to the object boundary (compartments with less than 26 neighbors). This is done by calculating the Euclidean distance map [112] of the object. The compartment with the highest distance number is selected and called the seed point. In case of several compartments sharing the highest distance value, one of them is selected randomly. Now the Euclidean graph distance [109] from each compartment in the object to the seed compartment is computed. This is the shortest connection along the graph between two compartments. Compartments with a local maximal graph distance are assigned as line endings (Figure 2.12g).

Thinning

One disadvantage of thinning is the possibility of inward erosion, which could potentially create wholes in the object. To prevent these artifacts, an iterative approach is used [108]. Using the N6 and N18 topologies defined above, boundary layers are assigned that are peeled by an iterative algorithm (Figure 2.12h):

1. collect the set of N6 boundary compartments (compartments where at least one of the N6 neighbors is missing)

2. delete all simple compartments (according to the N26 topology) in this set, starting with those who have the lowest number of neighbors (i.e. inter-compartmental pointers)

3. collect the set of N18 boundary compartments (compartments where at least one of the N18 neighbors is missing)

4. delete all simple compartments (according to the N26 topology) in this set, starting with those who have the lowest number of neighbors

5. continue with 1) until no more simple compartments are found.

A detailed description of such an algorithm can be found in [108], [111].

Graph validation and pruning

Imaging and segmentation can lead to artifacts like loops and clusters in the thinned midline representation of the objects, which have to be removed by post processing. Loops are removed by selecting one end-line location and calculating the shortest path from this end-line location to all other end-line locations in the object. Compartments or inter-compartmental pointers that are not used by any path within this validation step (Figure 2.12i/j) are removed from the object.

Since the approximate end-line locations were local distance maxima from an inner seed point, swellings within the neuronal branches will result in short sub-branches that are regarded artificial (Figure 2.12k). Therefore these short branches are removed within this pruning step from the object if the distance from the according end-line location to the first intersection compartment is shorter than 3μm (derived by systematic testing). Non artificial axonal sub-branches below this length threshold will hence be pruned as well. However, for most scientific problems this error is negligible.

2.2.6 Semi-automated post-processing

The image processing, so far, transformed the deconvolved raster image into a vector image representation of thinned foreground objects. Each object is therefore represented as a 3D graph with end-line locations (endings). Furthermore, compartments that are connected to more than two neighbors will set to be an intersection. This set of endings, intersections and normal compartments is converted to an ASCII file that can be either visualized in Amira or Neurolucida. Up to this point, all processing steps are automated. Final editing and splicing of the reconstructions is done manually.

Editing

The automatically traced graph is converted into a custom designed "SpatialGraph" format, representing points, nodes (intersections, endings) and edges (lines between nodes, connecting points). Each of the three structures can store multiple data, such as radii, structure type or even membrane potential. This data format, established in cooperation with Vincent J. Dercksen (ZIB) is the basis for any visualization of and interaction with traced neuron morphologies. Using the Amira-based "SpatialGraphEditor" it is possible to select any structure in the tracings, to delete, connect are labeled them individually.
Artifacts that were similar in shape or gray value to neuronal structure have to be erased. In most cases these artifacts are astrocytes (star shaped glial cells). This dirt-removal is done by superimposing the SpatialGraph with the maximum z-projection of the original image stack in the SpatialGraphEditor in Amira. Within the projection image neuronal structures can be easily distinguished from artifacts. Neuronal branches appear as elongated structures within the projection image, whereas falsely traced artifacts are either small spots (most intense parts of unstained neurons) or star shaped if they are the remains of glial cells. These artifacts are then selected and erased.

Further, axonal branches that were not well filled and therefore traced as fragmented structure can be restored by selecting the fragmented edges and splicing them by automatically connecting their closest ending nodes, resulting in a single continuous axon arbor.
Within this interactive step, additional anatomical landmarks, such as section outlines, can be integrated. Superimposing the edited neuron reconstruction with a low magnification image, any visible anatomical structure (e.g. pia or barrel outlines) can be manually added to the automatic reconstruction of the neuron.

Splicing

The results of this automated reconstruction pipeline are 3D tracings of neuronal branches from adjacent, 50-100μm-thick sections. To obtain a complete reconstruction of a cell, the reconstructions from different sections (i.e. brain slices) have to be aligned and spliced (Figure 2.14). Fortunately, large radial blood vessels are running perpendicular to the pial surface and retain their positions within each tangentially cut brain slice, rendering them ideal as position reference points. The blood vessel pattern is therefore extracted during the automatic tracing procedure. Blood vessels are detected via a region-growing algorithm in a maximum intensity z-projection of the original image stack, prior to the deconvolution. Voxels with values close to zero (maximum transparent regions) are used as seed points for a region-growing algorithm.Region-growing seeks dark and almost circular shapes (shape number algorithm [66]) and labels these structures as blood vessels.

Using the "SpatialGraphEditor" introduced above, multiple adjacent sections can be placed on top of each other, by manually entering their section thickness (e.g. 50μm). According to the vessel pattern, the individual reconstructions are aligned coarsely, either manually or automatically, using a transform interface or a point-matching algorithm, respectively. More accurate alignment is then achieved by matching the upper branch

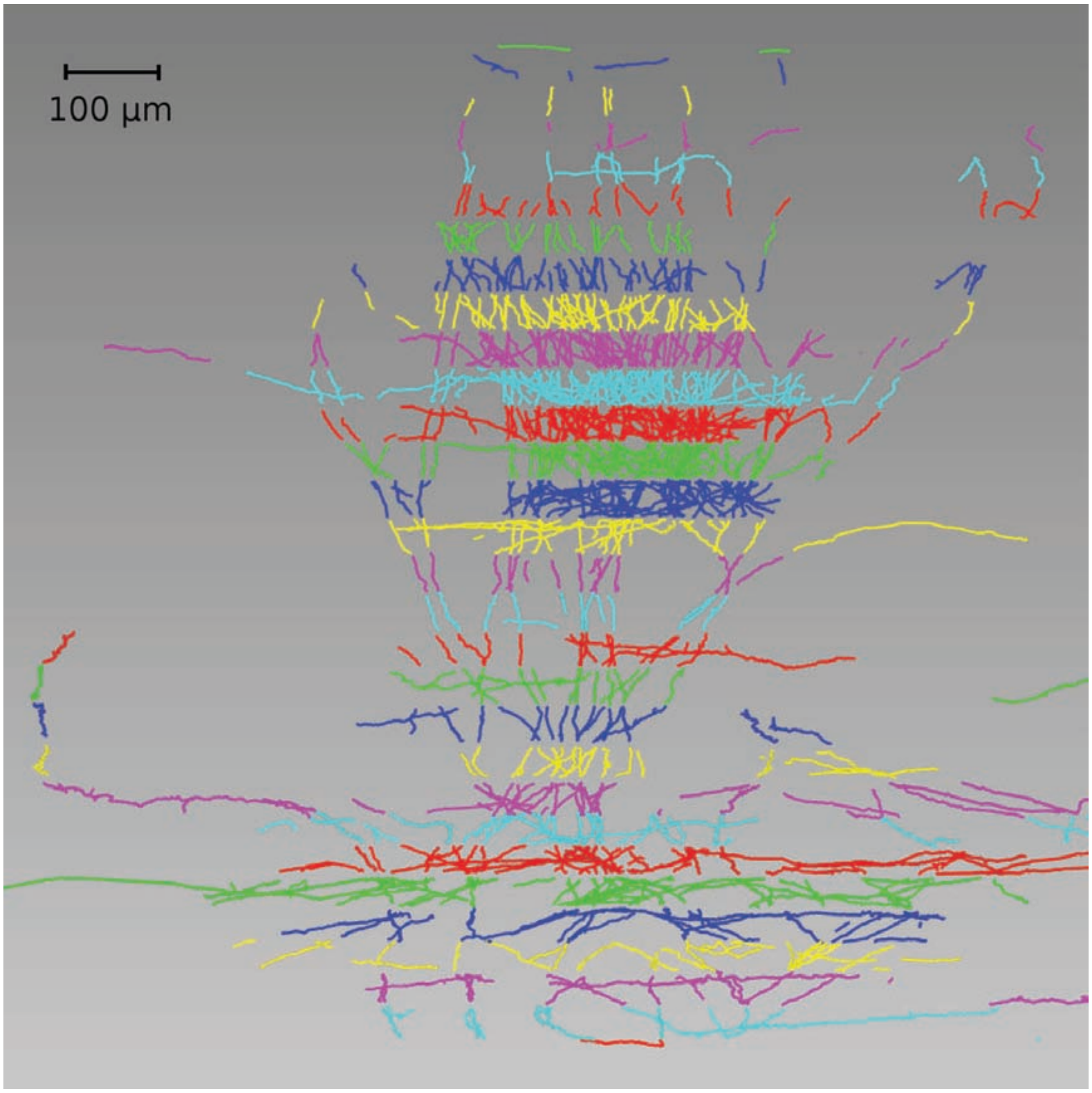

Figure 2.14: **Splicing of tracings from individual sections.** *Automatically aligned stack containing VPM axon fragments from 30 tangential cortical sections (segments colored by section). Figure adopted from [113].*

endings from a lower slice with the lower branch endings from an upper slice, again manually or automatically. Once all branches from individual sections are aligned with their counterparts from the adjacent section, the nearest nodes are spliced as described before. If splicing is performed manually, it proved to be convenient to start at the slice including the soma and to progressively connect the adjacent sections until a complete 3D neuron is reconstructed. If no soma is present (e.g. cortical part of the thalamocortical VPM axon arbor) the splicing starts at the deepest (most distant from the pia surface) section.

Even though the manual 3D alignment proved to be reliable, the automated alternative, especially for axonal reconstructions, can save a lot of time (from 1hour to 20 seconds) (Figure 2.14). The automated algorithm was tested and is described in detail in [113]. Briefly, based upon the point matching approach first described by [114], the correspondence between two 3D point sets and the rigid transform that optimally maps one point set to the other (in a least square sense) are calculated. Given two sections containing multiple polylines (i.e. SpatialGraphs representing traced neuronal branches), an optimal transform is computed, i.e. a rotation angle around the z-axis (perpendicular to the cutting plane) and a 2D (x/y) translation parallel to the cutting plane, using the following steps:

1. Find the set of points $P = \{\mathbf{p}_i\}$ from the first slice S_0 and $Q = \{\mathbf{q}_i\}$ from the other slice S_1, to be matched. Using the edge ending nodes only in the boundary regions r_0 and r_1 respectively, 2D point sets are obtained by orthogonal projection onto the x/y plane. The region size is chosen as a fraction of the total section thickness.

2. Find the set of candidate matchings and compute a starting transform for each matching.

3. For each starting transform, optimize the matching and transform with respect to a scoring function. The result is the transform corresponding to the optimal score.

2.3 3D registration of neuron morphologies

The aim of the presented work is to realistically reengineere the three-dimensional anatomy and synaptic connectivity of neuronal circuits. This requires the placement of any reconstructed neuron in a reference frame that is sufficiently precise and can correct for variability between experiments.

Several quantitative two-dimensional registration methods have been reported for neurons traced from *in vitro* preparations [115], [116], [117]. Here, I present a three-dimensional registration method (daVinci), established in cooperation with Dr. Moritz Helmstädter (MPI for Medical Research, Heidelberg) and Dr. Christiaan P.J. de Kock (VU Amsterdam) [118], that allows to combine neuron tracings from many *in vivo* experiments and hence to build up a standardized model of a cortical barrel column. The method compensates for differences in cortical thickness between animals, shrinkage of physical brain sections and deviations in cutting angle, which is usually not perfectly perpendicular to the vertical column axis. The registration can be summarized by the following five steps:

1. reconstruction of neuron (soma, dendrites, axon) from 20-40 adjacent tangential (with respect to S1) 50-100μm thick brain sections,
2. reconstruction of reference contours (pia, barrel, white matter (WM)) for each brain section,
3. calculation of the most likely vertical column (z-)axis using the pial surface above the neuron and the center of the barrel closest (lateral) to the soma (”home barrel”),
4. rotation of the neuron with respect to the calculated most likely vertical column axis,
5. application of inhomogeneous scaling along the most likely vertical column axis in order to register the pia, barrel and WM to fixed standardized distances.

2.3.1 3D reconstruction of reference contours

All presented morphologies are obtained from *in vivo* stained neurons, traced from tangential (i.e. perpendicular to the vertical column axis) brain slices. For each of these reconstructions, the outlines of the pia, barrels and WM are traced manually by superimposing a low magnification (2x) image of each brain slice with the neuron tracing in Neurolucida or in the "SpatialGraphEditor" in Amira (Fig. 2.15a). The pia outlines are drawn for the top ten brain slices, whereas the barrel and WM contours are usually only visible in L4 or some bottom slices, respectively (Fig. 2.15b).

Using the ten pia contours, a two-dimensional distance transform [66] is calculated for each slice. These distance transforms are then interpolated and smoothed in three dimensions. Finally the isosurface at value zero of the distance transform is calculated.

The same algorithm is used to interpolate the barrel and WM surfaces. The barrels are visible as slightly darker stained regions in brain slices of L4 (Fig. 2.15a). Depending on the slice thickness and cutting angle, the number of contours for individual barrels can differ from two to eight. In any case the barrel that contains (or is laterally closest to) the neuron's soma is traced and assigned to be the "home barrel". Further, the first neighboring barrel in the rostral direction is traced (e.g. home barrel D2, first rostral neighbor barrel D3). In addition, as many WM contours as visible are traced in the bottom-end sections of the cortex. Their number usually differs from four to eight, depending on how many brain slices were cut in total. Figure 2.15b/c shows an example of the ten pia, "home" and rostral barrel and WM contours and their corresponding surfaces for a thick tufted L5B pyramidal neuron.

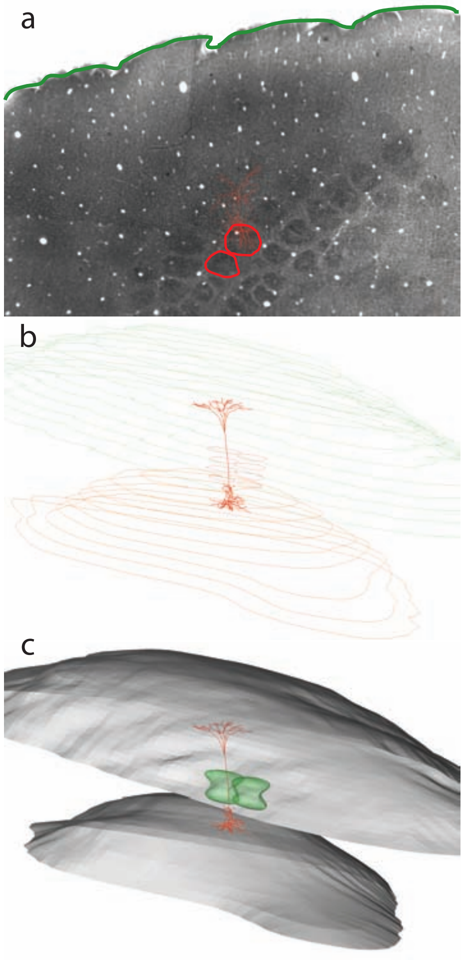

Figure 2.15: **3D reference contours.** *(a) Traced 3D L5B neuron morphology superimposed with a low-magnification (2x) image of a tangential (with respect to D2 barrel) brain slice. The outline of the brain slice (green) and the "home barrel" and its first rostral neighbor (red) are manually traced. "Home barrel" refers to the darker area in slices in L4 that contain the soma, when extrapolated to all sections. (b) Manually traced contours for the ten top pia sections (green), the "home" and first neighboring rostral barrel and the white matter (WM) (orange). (c) Smoothed and interpolated isosurfaces created from the contours in b. The intersection points of the vertical column axis with the pia, "home barrel" top, bottom and WM surface are scaled to fixed measured values, resulting in a standardized cortical column of 2000μm height.*

2.3.2 Calculation of most likely vertical column axis

The prior described contour surfaces are used to compute an approximation of the vertical column (z-)axis. This calculation is based on two assumptions:

1. the vertical column axis is approximately perpendicular to the pial surface above the column,
2. the distance between the home barrel center and the pial surface is minimal along the vertical column axis.

Therefore, the approximate home barrel center is calculated as the midpoint of all its barrel contours. Next, lines between this barrel center and all patches (surface triangles) of the pial surface within a given distance are determined. Then, connection lines to patches that are most parallel to the patch normal are determined. This results in a set of "best-matching" vertical column axes from which a user can interactively select (in MATLAB) the most likely vertical column axis (Fig. 2.16a).

2.3.3 Translation and rotation to standard barrel system

After the vertical column axis is set, the coordinate system can now be transformed such that the origin is aligned with the home barrel center (translation) and that the z-axis is aligned to the most likely vertical axis (z-axis rotation). Figure 2.16b shows an example of this rotation for a thick tufted L5B neuron. Further, this transformation is applied to the interpolated home barrel surface. This transformed home barrel is then used to calculate the vertical position of the barrel bottom and barrel top, which will be of importance in the next section.

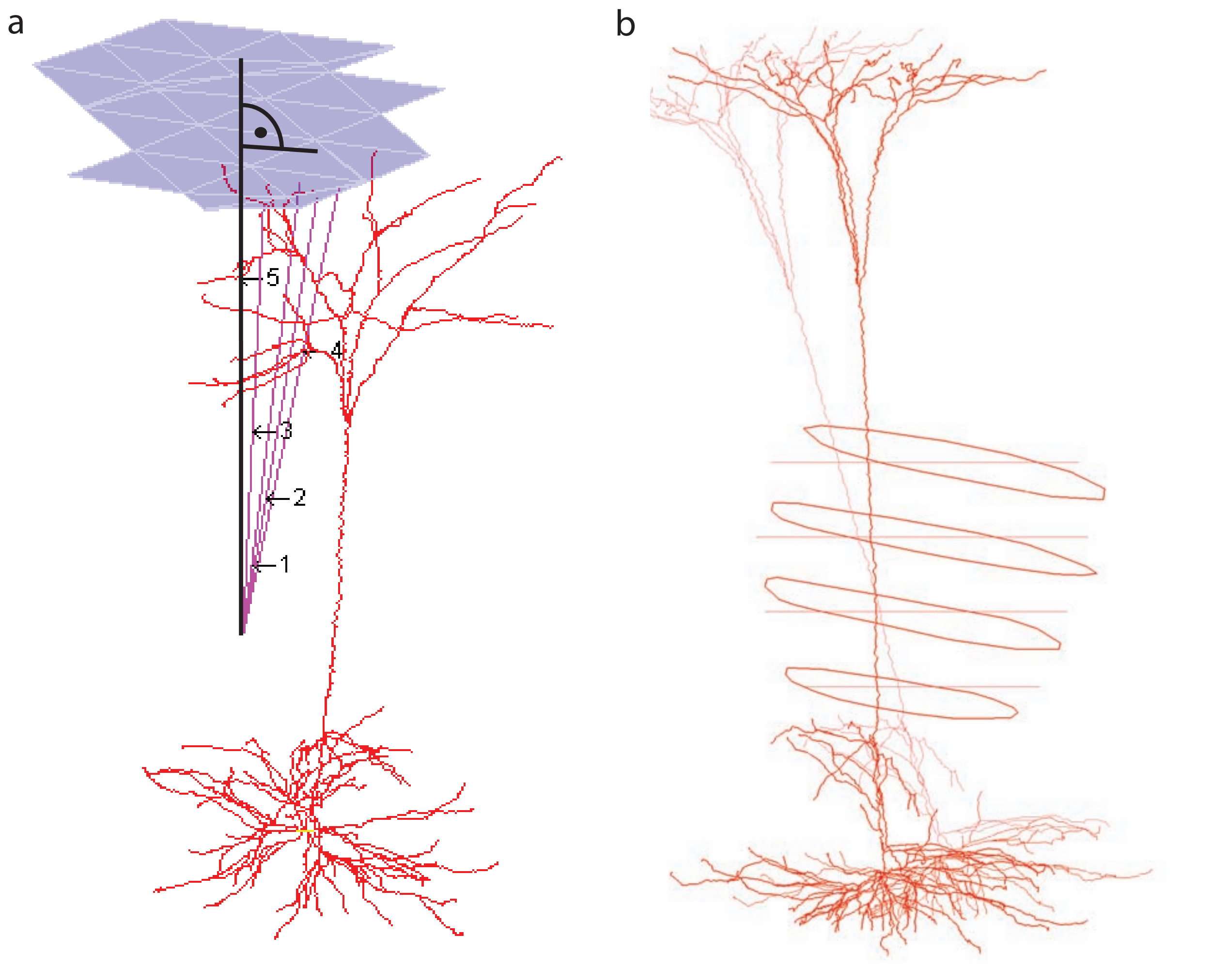

Figure 2.16: **3D registration.** *(a) Illustration of setting the "best" vertical z-axis of the cortical column. Minimal connecting lines from the "home barrel" center to the pial surface are calculated. A set of lines perpendicular to a pial surface patch (triangle) is displayed and can be interactively chosen be the user. Here, line 5, most parallel to the neurons apical dendrite, is set to be the optimal vertical column axis. (b) Rotated neuron. The prior tilted neuron and barrel contours (light red) are rotated to the optimal vertical axis (red).*

2.3.4 Inhomogeneous z-scaling to standard barrel system

In a final step the translated and rotated neuron reconstruction is inhomogeneously scaled along the newly assigned z-axis. Therefore the intersection points of the z-axis with the pia, the upper barrel border, the lower barrel border and the WM surface are calculated. Mean standard distances for these values were obtained by measuring them in fifteen experiments, comprising forty 50μm thick brain slices, respectively. This measurement yielded the following standard distances:

- pia-to-upper barrel border: 575μm,
- upper-to-lower barrel border: 360μm,
- lower barrel border-to-WM: 1065μm,

which in consequence result in a standard column height of 2000μm. These standard measures are compared with the calculated vertical intersection points and hence result in three z-scaling factors. Simple non-continuous transition between these factors finally results in a depth-dependent z-scaling profile. The final, translated, rotated and scaled neuron reconstructions are regarded as registered into the geometrical reference frame of a cortical column with a precision of approximately 50μm [118]. This value is therefore the ultimate resolution limit for any further consideration of the average standard column.

2.4 3D classification of neuronal cell-types

The previous sections described methods to reconstruct and standardize neuron morphologies in three dimensions. However, in order to realistically interconnect these neurons within microcircuits in a cell-type-specific manner, one needs to objectively classify and group the tracings into meaningful subclasses. This is usually achieved by cluster analysis of multidimensional parameters, in the following called neuron features.

As explained in the introduction chapter, neurons can either be classified by their physiological properties in response to a stimulus, their post-synaptic (i.e. dendritic) and/or their pre-synaptic (axonal) innervation pattern. Here, I will present a clustering method, NeuroCluster, that reliably groups traced excitatory neurons of a cortical barrel column in S1. The grouping is based upon thirteen anatomical dendritic features, which are determined for each object (i.e. neuron tracing). Further, their presynaptic counterparts (i.e. thalamocortical VPM axons) are classified by anatomical axonal features. In addition it is possible to analyze the physiological properties of these anatomical neuron classes.

2.4.1 Cluster algorithm

The effectivity, i.e. the quality or usefulness of most standard cluster algorithms (e.g. k-means [65]) is affected by three interconnected issues [119]:

1. most algorithms require input parameters (e.g. anatomical features) that are hard to determine for real-world data sets,
2. the algorithms are very sensible to these parameter values, often producing very different partitionings of the data set even for only slightly different parameter settings,
3. high-dimensional real-data sets often have a skewed distribution, that cannot be revealed by a clustering algorithm using only one global parameter setting.

For these reasons, I present an alternative algorithm, called OPTICS (Ordering Points To Identify the Clustering Structure) [119], which is not limited to one global parameter setting. It has been adopted for neuronal data sets by my collaborators Dr. Stefan Lang

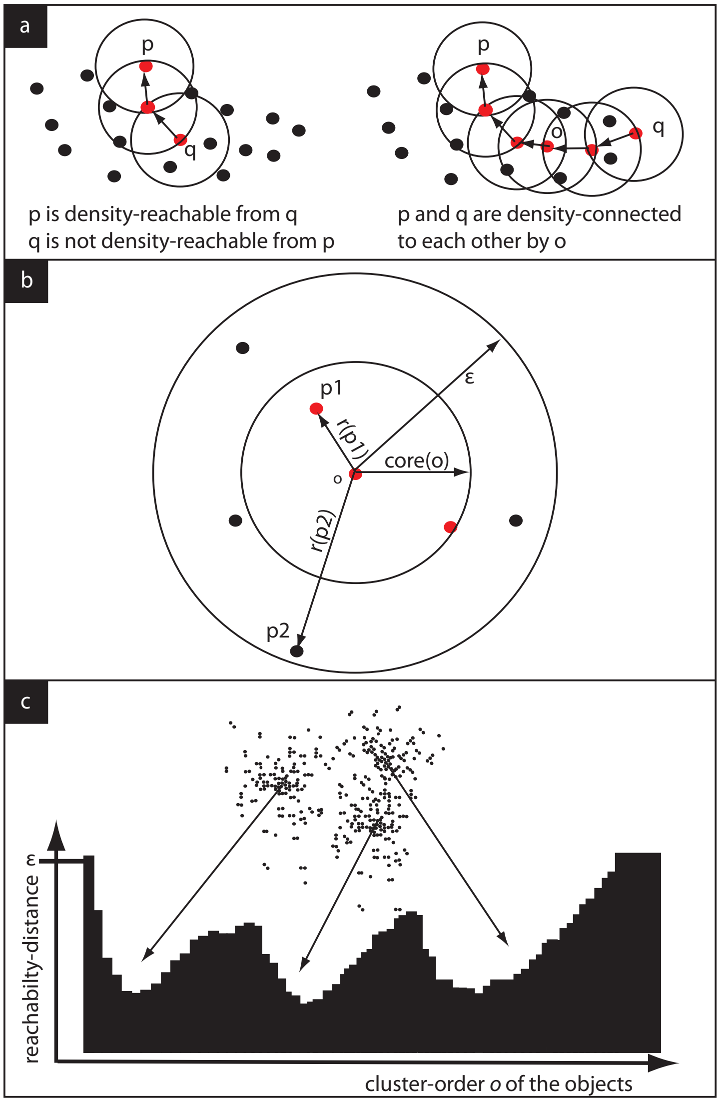

Figure 2.17: **OPTICS clustering.** *(a) 2D illustration of density-reachability and connectivity. The circles have radius* ε *and* $MinPts = 3$*. Point* q *is core object,* p *not. Therefore, point* p *is density-reachable from* q*, but not vice versa. (b) 2D illustration of core- and reachability distances. The number of* $MinPts = 3$ *defines the core-distance* $core(o)$*. If more than (or equal to)* $MinPts$ *points are within a radius* ε *around* o*, then* o *is core-object and all density-reachable points are assigned with a reachability-distance (e.g.* $r(p1), r(p2)$*). (c) Illustration of the cluster-ordering and OPTICS results. The reachability-distance for each object is plotted in an augmented order. "Valleys" in this plot indicate clusters. Figure adopted from [119].*

and Albert Berman (Institute for Scientific Computing (IWR), Heidelberg). This algorithm does not produce a clustering explicitly, but instead creates an augmented ordering of the data set, representing its density-based clustering structure. For the here presented medium-sized data sets (78 S1 dendrite and 14 VPM axon reconstructions) the cluster-ordering can be represented graphically, making it easy to extract not only the "traditional" cluster information, but also the intrinsic cluster structure.

The basic concepts of OPTICS are subsequently introduced in order to understand how the resultant neuronal cell-types, presented in the result section, are obtained. The key idea of density-based clustering is that for each object (i.e. a neuron, represented by a feature vector) of a cluster the neighborhood of a given radius (ε) has to contain at least a minimum number of objects ($MinPts$), i.e. the cardinality of the neighborhood has to exceed a threshold. The formal definitions for this notation of a clustering, adopted from [119], are given below and are illustrated by Figure 2.17:

- **Definition 4: directly density-reachable**:

  Object p is *directly density-reachable* from object q with respect to ε and $MinPts$ in a set of objects D if:

  1. $p \in N_\varepsilon(q)$, where $N_\varepsilon(q)$ is the subset of D contained in the ε-neighborhood of q.
  2. $Card(N_\varepsilon(q)) \geq MinPts$, where $Card(N)$ denotes the cardinality of the set N

  If the latter condition holds for an object p, then p is called a "core object". Objects can only be *directly density-reachable* from core objects.

- **Definition 5: density-reachable**:

  Object p is *density-reachable* from object q with respect to ε and $MinPts$ in a set of objects D if there is a chain of objects $p_1, ..., p_n$, $p_1 = q$, $p_n = p$ such that $p_i \in D$ and p_{i+1} is *directly density-reachable* from p_i with respect to ε and $MinPts$.

- **Definition 6: density-connected**:

  Object p is *density-connected* to object q with respect to ε and $MinPts$ in a set of objects D if there is an object $o \in D$ such that both p and q are density reachable from o with respect to ε and $MinPts$.

- **Definition 7: cluster and noise**:

  A *cluster* C with respect to ε and $MinPts$ in D is a non-empty subset of D satisfying the following conditions:

  1. Maximality: $\forall p, q \in D$: if $p \in C$ and q is *density-reachable* from p with respect to ε and $MinPts$, then also $q \in C$.
  2. Connectivity: $\forall p, q \in D$: p is *density-connected* to q with respect to ε and $MinPts$ in D.

  Every object not contained in any cluster is *noise*.

- **Definition 8: core-distance of p**:

  If $(MinPts - distance(p))$ is the distance from p to its $MinPts$' neighbor, then the *core-distance* of p is defined as:

  $core - distance_{\varepsilon,MinPts}(p) =$

  - $UNDEFINED$, if $Card(N_{\varepsilon}(p) < MinPts)$,
  - $MinPts - distance(p)$, otherwise.

- **Definition 9: reachability-distance of p with respect to o**:

  The *reachability-distance* of p with respect to o is defined as:

  $reachabilty - distance_{\varepsilon,MinPts}(p, o) =$

  - $UNDEFINED$, if $|N_{\varepsilon}(o)| < MinPts$,

  - $max(core - distance(o), distance(o, p))$, otherwise.

Intuitively, the reachability-distance of an object p with respect to another object o is the smallest distance such that p is directly density-reachable from o and o is a core object (Fig.2.17).

Based upon the above definitions, the OPTICS algorithm creates an augmented ordering of the data set and additionally stores the core-distance and a suitable reachability-distance for each object.

- **Definition 10: results of the OPTICS algorithm**:

  If data set D contains n points, then the OPTICS algorithm generates an ordering of the points $o : 1...n \rightarrow D$ and corresponding reachability-values $r : 1...n \rightarrow R_{\geq 0}$.

Finally, plotting the n reachability values in the order o for medium sized data sets, allows to identify clusters simply as "valleys" (Fig.2.17c). In consequence, once a reasonable set of features (i.e. parameters) is extracted for each neuron, the resultant reachability plot will immediately and objectively yield anatomical neuron-types.

2.4.2 Cluster features

Given a reliable cluster algorithm, as introduced above, one still needs to define anatomical features that capture the essential information of individual neuron morphologies. Such features can either be related to the neuron's shape, its geometry or some additional information, such as brain region or genotype. Albert Berman and I tried a large variety of parameters (up to 70) until a specific stable cluster structure emerged for different feature combinations.

It should be emphasized that the prior described three-dimensional registration and therefore standardization is essential for the goodness of classification. Hence, only registered

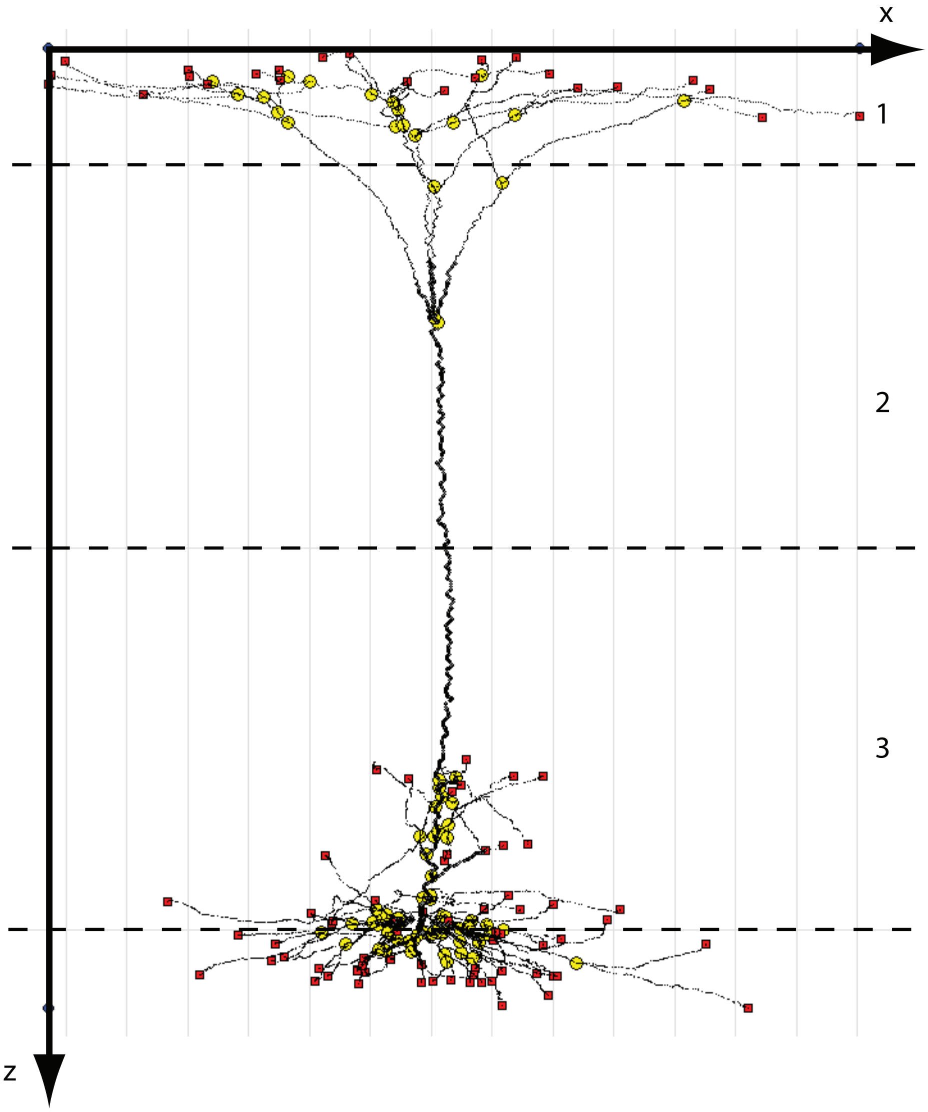

Figure 2.18: **Anatomical neuron features.** *Illustration of anatomical feature extraction. The longest dendrite (here: apical dendrite of L5B pyramidal neuron) is subdivided into three bricks (dashed lines) along the vertical axis (here: representing apical "root", trunk and tuft). Shape- and geometry-related features are extracted for each brick and the entire neuron. Red and yellow dots mark ending and branch points respectively.*

morphologies are used for the subsequently presented methods and results.

Another essential step is to split up the neuron into three bricks along the vertical column axis. Anatomical features are then extracted for the entire morphology and these three dendrite regions (Fig.2.18). The splitting reflects the general grouping of neurons into pyramidal and non-pyramidal cells. Only pyramidal neurons contain a so called apical dendrite, which is also their longest dendrite. In contrast, the longest dendrite in non-pyramidal neurons, like L4 spiny stellates, is arbitrary.

Apart from reliably separating pyramidal from non-pyramidal neurons, the brick-wise feature extraction along the longest dendrite can further discriminate between different types of pyramidal neurons. In general the apical dendrite emerges at the soma, branches (apical "root") and then reduces to a single branch (apical trunk) that might branch again at the region most distant from the soma (apical tuft). The shape and the extend of branching of the apical tuft is cell-type-specific. Therefore the bricking of the longest dendrite also reflects the division into apical "root", trunk and tuft and allows therefore to distinguish between different types of pyramidal and non-pyramidal neurons.

After a stable classification result was achieved, the number of features (i.e. dimension of parameter space) was reduced to a minimum using a genetic search approach [120]. The remaining thirteen anatomical features (Fig. 2.18) are grouped into shape- and geometry-related parameters and are listed below.

Neuron-shape-related:

- $MaxDendZrange$: Maximal extend along the z-axis (vertical column axis) of the longest dendrite (i.e. for pyramidal neurons this reflects the vertical extend of the apical dendrite).
- $MaxDendTh3XYdiagonal$: Maximal extend in the horizontal x/y-plane of the upper brick of the longest dendrite (i.e. for pyramidal neurons this reflects the horizontal

extend of the apical tuft).

- *NeuronXYdiagonal*: Maximal extend in the horizontal x/y-plane of the entire dendrite pattern.
- *NeuronXYZBox*: Volume of the bounding box around the entire dendrite pattern.
- *NeuronESumPolarR*: Sum of direct distances from the the soma to all ending points.
- *NeuronEAvgPolarR*: Average value of direct distances from the soma to all ending points.
- *NeuronEMaxPolarR*: Maximal direct distance from the soma to an ending point.

Neuron-geometry-related:

- *MaxDendCentroidDistSXYZ*: Center of Mass of the longest dendrite, assuming a uniform dendrite thickness.
- *NeuronCentroidDistSXYZ*: Center of Mass of the entire dendrite arbor, assuming a uniform dendrite thickness.
- *NeuronBpNumber*: Number of branch points in the entire dendrite arbor.
- *NeuronLocalAvgBranchOrder*: Average branch order (i.e. max tree depth) of every individual dendrite.
- *NeuronSumLength*: Total trace length of all dendrites.

Additional user information:

- *PiaDistanceRegistered*: Distance from the soma to the interpolated pial surface along the vertical column axis after 3D registration with daVinci.

By extracting the same features for axons, the cortical part of the thalamocortical VPM axon reconstructions could be clustered. Two features are absent for these morphologies. First, the *PiaDistanceRegistered* cannot be calculated, because the soma of these cells is in the thalamus, and only the cortical part was reconstructed. Second, the axon is a single structure, meaning the longest axon is identical to the entire axon. Therefore the feature vector for VPM axons has only eleven entries: *NeuronZrange, NeuronTh3XYdiagonal, NeuronXYdiagonal, NeuronXYZBox, NeuronESumPolarR, NeuronEMaxPolarR, NeuronEAvgPolarR, NeuronCentroidDistSXYZ, NeuronBpNumber, NeuronLocalAvgBranchOrder, NeuronSumLength.*

2.5 3D reengineering of average neuronal networks

Recently reported methods aim to reengineere morphologically realistic large neuronal networks, like a cortical barrel column [121] or the cerebellar granule layer [122]. These approaches distribute synaptic connections either randomly on user-defined parts of the dendrites [122] or use geometrical constraints, like proximity of a pre-synaptic axon to a post-synaptic dendrite [121]. Both methods have in common that the user needs to specify the potential number of synapses, and its variability, for each pre- and post-synaptic connection-type. The reason is that a quantitative three-dimensional description of the presynaptic axonal arborization is difficult to obtain. Therefore, the axon is either completely ignored and the number of synapses, as well as the most likely volume of axon innervation is estimated [122] or the axonal arbor is extrapolated from *in vitro* reconstructions. The latter, called "neuronal healing" [121], compensates for missing parts of the axonal arborization in *in vitro* reconstructions. These extrapolated axons are superimposed with the post-synaptic neuronal network. Synapses are then set at touching points between the dendrites and the extrapolated axons.

Here, a different approach will be presented. Neither the number of synaptic contacts, nor the axonal innervation need to be estimated or extrapolated. The subsequently presented method is regarded as a statistical approach, to contrast the geometrical method by [121]. The above presented methods (NeuroCount, NeuroMorph, daVinci, NeuroCluster) determine three-dimensional neuron distributions, reconstruct neuron dendrites and axons, standardize the tracings and objectively classify them. They supply sufficient quantitative anatomical data to reengineere *average* neuronal networks, like a cortical barrel column, in three dimensions and to synaptically interconnect different neuron populations. In consequence, the cell-type-specific number and three-dimensional distribution of synapses are no input parameters, but results of the here presented network building tool, called ”NeuroNet”.

NeuroNet is again based upon custom written software for Amira [62]. This editor has been established in cooperation with Vincent J. Dercksen (ZIB, Berlin) and allows to interactively reengineere and visualize neuronal networks in three dimensions, using measured and reconstructed anatomical data. The interactive approach proved to be essential in order to control the complex process of building up high-resolution full-compartmental network models. In addition, NeuroNet yields cell-type- and position-specific three-dimensional innervation statics for each neuron in the network.

The number and three-dimensional synapse distribution for individual connection types will be a major result of the here presented thesis. In particular, the cell-type-specific number and distribution of thalamocortical VPM synapses within an excitatory cortical barrel column in S1 will be presented in the result section. Comparing these statistical, purely anatomical results, with previous connectivity estimates from electrophysiological paired recordings performed *in vivo* [12], will prove that the reengineered *average* cortical barrel column realistically reproduces the cortical morphology and connectivity.

2.5.1 NeuroNet

Figure 2.19 illustrates the subsequently described general concept of NeuroNet:

Standardized reference frame The first step to reengineere an average neuronal network in three dimensions is to establish a standardized coordinate system for the brain region of interest. This guarantees that the anatomical data, obtained from many different experiments, fits together and results in a reasonably accurate average network. In case of the cortical barrel column the pia, WM and barrel contours functioned as such standardized position landmarks along a 2mm long vertical column axis. This coordinate system has its origin at the barrel center and will hence be referred to as the "barrel-centered" column. The approximate accuracy of the above described registration method (daVinci) was about 50μm.

3D total neuron soma distribution Once a reference system is established, the average number and three-dimensional distribution of all neuron somata in this brain area needs to be determined by NeuroCount. The resultant soma distribution is transformed into the standardized reference system (e.g. "barrel-centered" column) and then converted into a neuron density distribution, by superimposing a three-dimensional grid. In case of the "barrel-centered" column, a grid resolution (voxel) of 50μm x 50μm x 50μm is chosen, in order to match the registration accuracy. Here, the average distribution of excitatory somata in S1 is determined for a cuboid with dimensions of 550μm x 550μm x 2000μm, resulting in a grid of 11 x 11 x 40 (i.e. 4840)

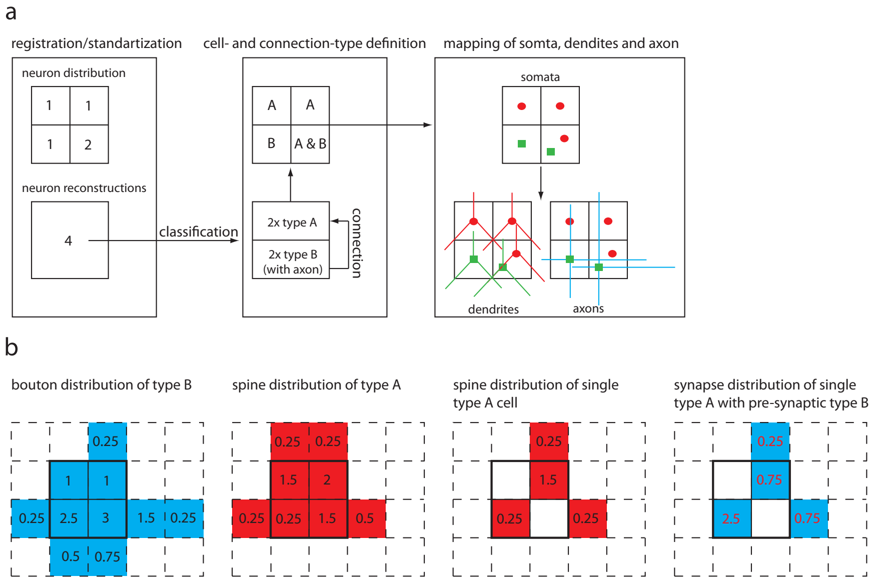

Figure 2.19: **Illustration of NeuroNet.** *(a) Soma distribution grid and neuron tracings are registered to standardized anatomical landmarks (e.g. pia, WM, barrel). The numbers refer to cells per grid voxel and number of tracings, respectively. After classification of the dendritic and axonal cell-types (2 cells of type A and 2 of type B), the soma distribution is subdivided into overlapping cell-type-specific soma distributions (the overlap ratio in the lower/right voxel is 1:1). Type B contains axon (blue) and a connection from B to A is defined. Cell-type-specific somata are mapped into the grid and replaced with neuronal tracings of the corresponding type (A: red; B: green). (b) Extension of the grid to a maximal bounding box (dashed lines) covering all tracings. From left to right: total bouton density for type B axons; total spine density for all post-synaptic cell-types connected by type B (here: only type A); spine density for individual target cell (here: upper/right); voxel-wise relative proportion of each cell's spine distribution to the total spine distribution is calculated and then multiplied with the bouton density; this results in synapse density distribution of each cell, for each connection type. For illustration spine and bouton density, as well as voxel size are set to 1. Summing of voxel values result in cell- or cell-type-specific total spine, bouton or synapse numbers. Here, total number of boutons for type B: 11; total number of spines for type A: 6.5; total number of spines for upper/left cell: 2.25; total number of synapses for upper/left cell: 4.25.*

voxels. For each voxel the density value is given in neurons per cubic millimeter.

Specification of neuron-types The three-dimensional neuron density distribution usually contains various cell-types. Therefore a representative number of neurons from every part of the total distribution needs to be reconstructed manually or with NeuroMorph. The here presented dendrite tracings in S1 were mainly done manually, whereas all axon reconstruction were obtained by NeuroMorph. By first clustering the reconstructed cells by dendritic features with NeuroCluster, as presented above (see sec. 2.4), the number of neuron-types within the area of interest is determined. If, in addition, the axons for all neurons of a cell-type are reconstructed, a secondary clustering might reveal axonal subclasses. The total number of neuron classes (i.e. including subtypes) will be referred to as N.

Spatial extend of neuron-types Each reconstructed neuron is not only represented by its dendrites and/or axon, but also by the position of its soma with respect to the standardized reference frame. Calculating the mean and standard deviation of all somata positions yields the spatial extend of a neuron-type as a three-dimensional interval:

$$[p_i - 1.5 \cdot STD_i, p_i + 1.5 \cdot STD_i]; \tag{2.14}$$

where p_i is the mean, STD_i the standard deviation of soma positions for a cell-type and $i = x, y, z$. Hence, the total neuron density distribution is subdivided into N mutually overlapping cell-type-specific soma distributions. The ratio in the overlap zones is specified by the user (e.g. in the overlap zone between L5A and L5B in S1 the ratio is estimated as 1:1).

Mapping of cell-type-specific somata For each voxel of the soma distribution grid the number of neurons is calculated. If more than one cell-type constitute to one voxel, the relative numbers per cell-type are assigned according to the estimated overlap ratio. Within each voxel the assigned number of neurons is distributed, guaranteeing identical distances between the somata and to the voxel boundaries. It is further assured that the soma position is never outside the spatial extend of its corresponding cell-type. This step results in N cell-type-specific neuron soma distributions.

Mapping of neuron morphologies Each of the N three-dimensional neuron distributions comprises n_j $(j = 1, ..., N)$ neuron soma positions. A neuron tracing of the corresponding cell-type is mapped onto each soma position. Hence, $n = \sum_{j=1}^{N} n_j$ neuron somata are replaced by n neuron tracings, represented as SpatialGraphs (see sec. 2.2.6). Further, it is assured that the new soma position of each tracing does not differ by more than 50μm in each direction from its standardized previous soma position. It is optional to compensate for the change in soma position by scaling the tracing in one or more dimension:

$$scale_i = \frac{somaPos_{old,i}}{somaPos_{new,i}}, \tag{2.15}$$

where $i = x, y, z$. In case of the cortical barrel column the scaling is applied along the vertical (z-)axis. This guarantees that the transformed reconstructions still fit into the standardized column of 2mm height (e.g. the apical tuft of a L5B pyramidal neuron always ends in L1 and never sticks out of the pial surface or ends in L2). However, in general the mapped dendrites and axons extend further than the original grid, specified by the three-dimensional soma distribution (i.e. 11 x 11 x 40 for a cortical barrel column). Hence, the grid is extended to the maximum bounding box, covering each dendritic and axonal branch of the network.

Cell-specific spine and bouton distribution The previous steps resulted in n neuron tracings, grouped into N types and distributed according to corresponding three-dimensional neuron distributions. For each neuron, its dendritic trace length per voxel of the extended grid is calculated. The resultant dendrite density (in $\frac{\mu m}{\mu m^3}$) for each cell is scaled with a cell-type-specific spine density (in spines per μm). Spines are potential sites for synapses on dendrites of excitatory neurons. Therefore the sum of all voxels result in the total number of spines for each post-synaptic neuron.

If the axon is reconstructed for $m \leq n$ tracings, in addition, the axon density is determined. It is scaled with the cell-type-specific bouton density. Boutons are potential pre-synaptic connection sites. Hence, the sum of all voxels results in the maximum number of connections a pre-synaptic cell can make.

Cell-type-specific spine and bouton distribution The previous step resulted in n SpatialGraphs, n spine distributions and m bouton distributions. By summing up the distributions in a cell-type-specific manner, the total number and distribution of spines and boutons for each of the N cell-types is obtained.

Specification of connection-types Each of the N cell-types can be in principle connected to any other one. Hence, the maximal number of connections is N^2. However, usually the axon is only reconstructed for some cell-types and some connections are functionally not obtained *in vitro* or *in vivo*. The number of connections K is therefore usually smaller than N^2. Nevertheless, each pre-synaptic cell-type can connect multiple post-synaptic types. Here, I present connections from one pre-synaptic cell-type (VPM) to eight excitatory post-synaptic types in S1.

Connection-, cell- and cell-type-specific synapse distribution Once all cell- and connection types are set, total post-synaptic spine distributions are calculated as the sum of all distributions for cell-types innervated by the same pre-synaptic type (e.g. VPM is pre-synaptic $\Rightarrow$ sum of eight post-synaptic spine distributions). Again, the total pre-synaptic bouton density defines the number of synapses that can be distributed. Then, for each post-synaptic neuron, its proportion to a total spine distribution (i.e. identical pre-synaptic connection type) is calculated voxel-wise. This ratio value is multiplied with the number of boutons in each corresponding voxel. This process results in a three-dimensional synapse distribution for each post-synaptic neuron:

$$synapseDistr_{j,(x,y,z)} = \frac{individualSpineDistr_{j,(x,y,z)}}{totalSpineDistr_{k,(x,y,z)}} \cdot boutons_{k,(x,y,z)}, \tag{2.16}$$

where $j = 1, ..., n$ and k specifies the pre-synaptic cell-type. A maximum of M connection-type-specific synapse distributions is possible for an individual cell. Summing up all synapse voxels, hence results in the absolute number of synapses per cell. Cell- and connection-type specific summing of all synapse distributions results in total numbers and three-dimensional distributions for a specific pre- and post-synaptic connection type.

Resultant three-dimensional anatomical network model In summary, NeuroNet receives a three-dimensional neuron distribution, N cell-types with classified dendrite and axon reconstruction and M connection types. Specifying the spatial extend, as well as spine and bouton density for each cell-type finalize the input. As output, NeuroNet then calculates:

1. the number and distribution of neurons for each cell-type,
2. a post-synaptic dendritic and a pre-synaptic axonal network, by mapping classified neuron tracings at each cell position,
3. the number and distribution of spines and boutons for each neuron,
4. the number and distribution of spines and boutons for each neuron-type,
5. the number and distribution of synapses for each neuron and connection-type,

6. the number and distribution of synapses for each neuron-type and connection-type.

In consequence, NeuroNet yields an anatomically realistic network model of n full-compartmental neurons (i.e. SpatialGraphs). Each neuron in addition has maximally M synapse distributions that specify the total number and position of connections. The network can then be transferred to a simulation environment, called "Neuro-Dune", established by Dr. Stefan Lang (IWR, Heidelberg). There, HH-typed neuron models can be mapped onto each neuron. Further, synapses are mapped according to corresponding synapse distributions. NeuroDune allows to simulate these large, full-compartmental and realistically interconnected networks with input measured *in vivo* (e.g. volley of synchronous thalamocortical APs from VPM into S1 after passive whisker deflection [10], [12]).

Connection and cell-type-specific sub-cellular synapse distribution In addition to the above results, NeuroNet also yields the possibility to investigate the sub-cellular synapse distribution for each cell- and connection-type. This is achieved by transforming each distribution in a way that voxels, which contain the soma, are superimposed. The resultant "soma-centered" distribution is a standard way to illustrate sub-cellular connections, which can hence be compared with results from other methods, such as the channelrhodopsin-2 (ChR2)-assisted functional mapping of synapses [123].

Chapter 3

Methodical results

So far, five custom designed methods for reengineering of three-dimensional neuronal microcircuits were presented. NeuroCount and NeuroMorph are designed to obtain indispensable anatomical data in a quantitative and objective manner. Further, they yield results within much less time than alternative manual standard methods. However, before this anatomical data can be standardized, classified and placed within a network by daVinci, NeuroCluster and NeuroNet respectively, the performance and accuracy of NeuroCount and NeuroMorph need to be validated. Therefore, automated results are compared to manually derived counterparts [61], [83], [29].

3.1 NeuroCount: 3D counting of neuron somata

The evaluation of the automated counting pipeline is done for eleven confocal image stacks of NeuN/GAD67-stained neuron somata. In general, the scientific interest focuses on neuron densities. Hence, the absolute number of neurons within the stack volume and the deviation of the neurons' position from manual counts need to be investigated. For this error analysis it is necessary to determine the corresponding landmarks from the manually and automatically processed sets. If the deviation in position between the automated and manually detected landmarks is of negligible amount, the absolute difference in landmark numbers can be regarded as a meaningful error value. In addition, the numbers of false positive (FP) and false negative (FN) landmarks are checked. Manually determined landmarks are used as the ”gold standard” and compared with the automated counting results. It should however be emphasized that the results of the manual counting are only accurate within 2.1% precision [38].

The eleven image stacks were randomly chosen from a large data pool that was used for evaluation of neuron densities within a cortical column of S1 in rats [38]. The stacks were taken at various magnifications (40x, 63x) resulting in different resolutions and stack volumes, at various cortical depths (300-1800μm from the pia surface) yielding different dominant neuron populations in each sample (e.g. L4 spiny stellates or L5 pyramidal neurons) [124] and at various slice orientations (i.e. thalamocortical, coronal, tangential). Further, comparison was performed ”double blind”, meaning stacks were first evaluated manually by different individuals and afterwards processed by the automated pipeline described above, without prior inspection of the manual counts.

3.1.1 Automated vs manual counting

Table 3.1 shows the results for the comparison of automatically and manually detected landmarks. No systematic miscounting is performed by the automated pipeline. The number of detected neurons differs similarly in both directions resulting in an average counting difference that is less than 1% (0.92% averaged over the number of data sets). However, the average absolute counting difference in landmark numbers is around 4%. This value is regarded as the absolute error of the automated counting.

♯	manual ♯s	automatic ♯s	relative ♯ difference [%]	absolute ♯ difference [%]	position deviation [μm]
1	430	425	1.16	1.16	4.54
2	846	896	-5.91	5.91	3.93
3	570	594	-4.21	4.21	4.23
4	871	915	-5.05	5.05	4.74
5	1219	1237	-1.48	1.48	4.75
6	809	776	4.08	4.08	1.92
7	719	670	6.82	6.82	2.05
8	739	680	7.98	7.98	2.07
9	1035	983	5.02	5.02	2.70
10	862	846	1.86	1.86	2.96
11	975	976	-0.10	0.10	3.16
		mean:	0.93	3.97	3.37
		STD:	4.77	2.53	1.11

Table 3.1:

The number and position of automatically detected NeuN landmarks is compared to manually generated counterparts for eleven image stacks. Each image stack comprises a single field of view acquired either with a 63x or a 40x objective, using a Leica SP2 confocal microscope. Table adopted from [29].

Deviation in landmark position

The average radius of neurons in S1 is between 5 and 15μm. If the deviation between a manually placed landmark and its automated counterpart is sufficiently lower than the smallest radius value of 5μm, the error in position can be neglected and the absolute difference in landmark numbers is regarded as a meaningful error value. For evaluation of position deviation the following algorithm was used:

1. Calculation of distances from each automated landmark to each manual landmark.
2. Sorting of distances, starting with the shortest one and assignment of this manual landmark as the nearest neighbor (NN) of the automated one.
3. Checking for multiple times assigned NN. If more than one automated landmark has the same NN, the closest automated one will keep this NN, the other automated landmarks are assigned to have their second closest manual landmark as their NN.
4. Step 3 is repeated until no manual landmark is assigned to more than one automated landmark.
5. The distance of all automated landmarks to their assigned manual NN is then averaged (see Table 3.1).

The average deviation in position of 3.37±1.11μm is sufficiently less than 5μm. It is further important to notice that the position deviation for each data set is smaller than 5μm. Hence the error in position can be neglected, because each automated landmark has a manual counterpart within reasonable distance. It is therefore justified to state that the absolute difference between manually and automatically detected neuron somata is 4%.

False positive/negative landmarks

In addition to the above considerations about average differences between manual and automated counts, a false positive/negative analysis for five randomly chosen stacks is performed. Two corresponding landmark sets are visualized in Amira and coinciding landmarks are manually deleted. The remaining automated landmarks are regarded as FP and the remaining manual landmarks are regarded as FN. These FP/FN objects are usually ambiguous cases of touching neurons that could for instance either be counted as one or two neuron somata. Table 3.2 shows the results for this analysis. Both, the average FP and FN values are around 5%. This compensatory effect explains the average relative counting difference of less than 1%.

	FN [%]	FP [%]
	9.30	2.78
	7.23	6.31
	4.71	7.58
	4.65	5.35
	3.19	3.01
mean:	5.82	5.01
STD:	2.43	2.08

Table 3.2:

Five corresponding landmark sets were visualized in Amira and coinciding landmarks were manually deleted. The remaining automated landmarks are regarded as false positive (FP) and the remaining manual landmarks are regarded as false negative (FN). Table adopted from [29].

Detection of GAD67 neurons from 2-channel images

The detection of neurons in the second channel is strongly dependent on the performance of the detection in the first channel. If the neuron is identified correctly in the first (e.g. NeuN) channel, the detection in the second (e.g. GAD67) channel was 100% correct. Hence, the absolute error value of 4% is also regarded as the error for the detection of GAD67 positive interneurons.

3.2 NeuroMorph: 3D reconstruction of single neuron morphologies

The reconstruction of neuron morphology, especially of thin axonal arbors, is impossible from raw TLB image stacks [88]. Hence, special focus on the optimization of the imaging system and the resultant deconvolution proved to be essential for a reliable tracing of both, dendrites and axons. Therefore, before comparing the semi-automated tracing results with manual counterparts, the influence of the optical components, the tissue and the deconvolution algorithm on the SNR of faint axons will be investigated.

3.2.1 Optical aberrations of cortical tissue

In Figure 3.1 the measured optical defocus coefficients (A_{020}) of the aberration function are plotted for a mechanical defocus from 0 to 10μm in 0.5μm steps. Each plot shows measured values averaged from eight samples. Figure 3.1a (plot C) illustrates the 40x dry objective in combination with fluorescent beads embedded in Mowiol. The optical defocus of almost 15μm for a mechanical defocus of 10μm is caused by the inhomogeneous refractive index within the optical pathway. The refractive index of the air between the specimen and the objective is approximately 1 ($n_{air} = 1.003$) and therefore refraction effects cause the apparent difference in optical and mechanical defocus. Consequently the use of dry objectives results in a much thinner appearance of the tissue.

The situation is different when oil-immersions objective are used (Figure 3.1a; Plot A/B). Figure 3.1a (plot B) illustrates bead samples embedded in Mowiol. Here the optical defocus is nearly identical to the mechanical one, because the refractive index between the objective and the specimen is homogeneous.

Using the marginal ray model described by [103] and introduced in the method section, the refractive index for bead samples embedded in tissue (Fig.3.1a; Plot A) can be calculated from the measured optical and the known mechanical defocus. At 10μm mechanical defocus the average resulting optical defocus from eight bead samples surrounded by tissue is $7.84 \pm 0.55\mu$m. Using this value, the approximate refractive index for slices from cortical rat tissue embedded in Mowiol is $n_{tissue} = 1.44 \pm 0.02$. Since the deviation in optical defocus and hence in refractive index is small (± 0.02) for bead samples embedded in tissue from different rats and slices, at random positions between these slices, the refractive index is regarded as homogenous for such specimen.

Regarding the tissue as an homogeneous medium, the deviations for spherical aberration measured for bead samples between slices of tissue should also be small. This prediction is verified by the results shown in the graphs in Figure 3.1b. Here the average measured coefficient for spherical aberration A_{040} is normalized to the wavelength λ of the illuminating light. Both plots for the oil-immersion objective (Figure 3.1b; plot A/B) show a constant coefficient for spherical aberration, independent of the mechanical defocus. However, the absolute coefficient value for bead samples between sections of tissue is slightly higher compared to the one for bead samples without tissue. This is reasonable since the major source for this type of aberration is the refractive index mismatch between the embedding

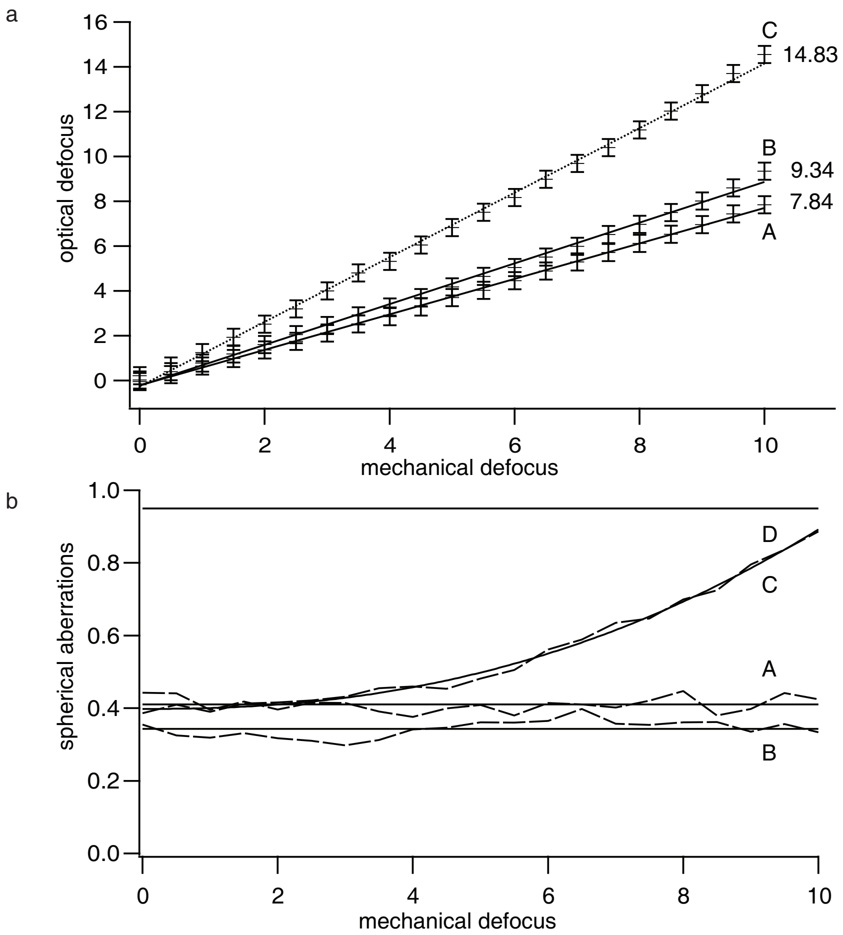

Figure 3.1: **SH measurements.** *a) Measured optical defocus (A_{020}) averaged for eight samples each. Whereas beads embedded in Mowiol (B) yield almost identical optical and mechanical defocus, beads between two layers of tissue (A) appear thicker. This suggests a slightly lowered refractive index. b) Measured spherical aberrations (A_{040}) averaged for eight samples each and normalized to the wavelength. As suggested by a, the spherical aberrations are slightly increased if the beads are embedded in tissue. However, the total amount of aberrations is independent of mechanical defocus for the oil-immersion objective (A/B) and well below one wavelength. In contrast, the spherical aberrations increase rapidly with defocus for the dry objective, reaching one wavelength at about $10\mu m$ mechanical defocus. Figure adopted from[83].*

and the immersion medium, which is slightly higher for tissue, as shown above.

For completeness, the spherical aberration coefficient for the dry objective is also measured. Figure 3.1b (plot C) shows that the coefficient for spherical aberration increases strongly with increasing defocus reaching the order of the wavelength at 10μm mechanical defocus. These measurements suggest that the used oil-immersion objective can be regarded as well corrected with respect to spherical aberration, since the normalized aberration coefficient meets Maréchal's tolerance condition [87]. It is therefore justified to assume ideal imaging condition and to reduce the image formation to the "refraction plus diffraction" model.

Model point spread function and cone of light

According to the above results of the SH wave front measurements, the tissue is regarded as homogeneous in refractive index. Therefore the light sources, here the neuronal processes from inverted TLB stacks, should have light cones which resemble the theoretically modeled cone. Figure 3.2a/b shows an x/z-plane from an inverted TLB stack with various light cones from neuronal projections and the modeled PSF, respectively. It can be clearly seen that the light cones qualitatively resemble each other. Quantitatively this was shown by measuring four angles, as specified by Figure 3.2c. The mean value for the four angles was between 42.42 and 45.9 degrees ($\alpha_1 = 44.6 \pm 1.8$; $\alpha_2 = 42.4 \pm 2.0$; $\alpha_3 = 43.6 \pm 1.8$; $\alpha_4 = 45.9 \pm 1.8$). Hence, the four angles are approximately similar. This is consistent with the assumption of refractive index isotropy. Further, the average angle of a light cone from neuronal projections in cortical tissue embedded in Mowiol, imaged by an oil-immersion objective is $\theta_2 = 44.1 \pm 2.3$ degrees. This value is in good agreement with the theoretical one of $\theta_2 = 44.0 \pm 1.54$ degrees (see method section) derived from the simple geometrical model, if a NA of 1.0 is assumed for TLB image stacks.

I further checked whether the angles are z-dependent. Therefore I subdivided the image

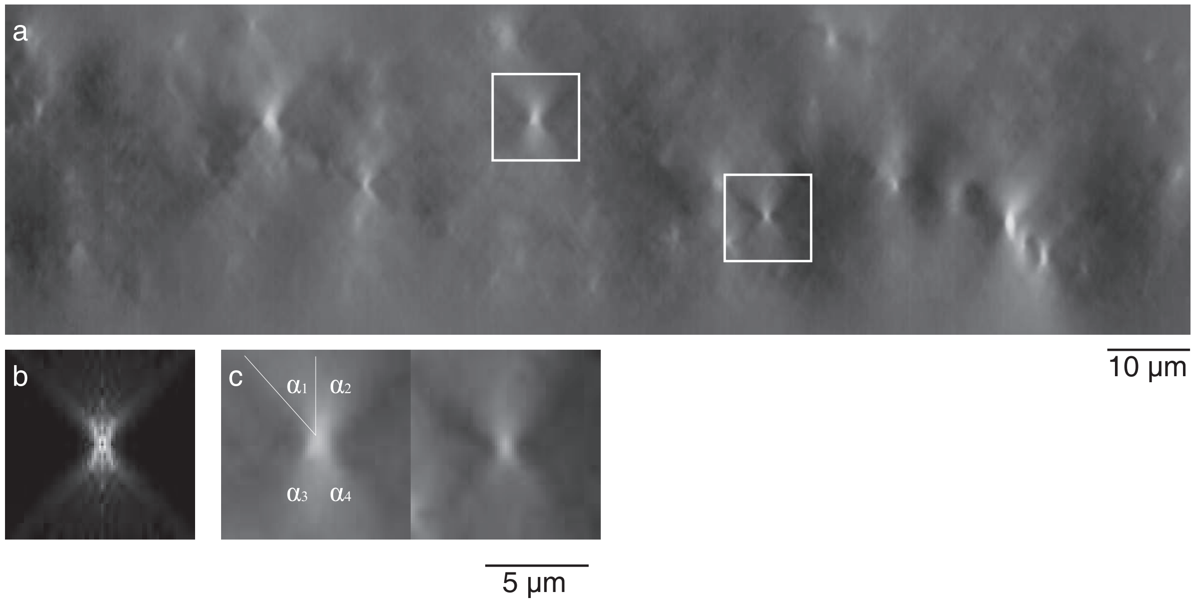

Figure 3.2: **Isotropy of cone of light.** *a) x/z plane from an inverted mosaic TLB image stack. The bright structures are characteristic light cones from neuronal projections. Quantitative analysis of these cones from various preparations proved that the cones resemble each other and the cone of the modeled PSF. b) Central x/z plane of the modeled PSF cone of light. The imaging system is reduced to a simple "refraction plus diffraction" model and based on the assumptions of ideal imaging conditions and a homogeneous refractive index of 1.44 of the tissue from rat cortex embedded in Mowiol. These assumptions are verified by the SH wave front analysis. c) Enlargement of two typical light cones from a. All for angles were measured for 15 dendrites and 15 axons from 6 different rats. The measured average angle is in very good agreement with the theoretically modeled one. Figure adopted from [83].*

stacks into four bins with 20μm thickness along the optical axis and calculated the corresponding average angles. Neuronal processes close to the interface between the tissue and the immersion medium (0-20μm) have an average angle of 43.8 ± 2.1. The angles for the subsequent bins of 20-40μm and 40-60μm are identical at 44.1 ± 2.3. The angles in the most distant region from the cover slip (60-80μm) are 44.9 ± 2.4. This implicates a slight depth dependence of the refractive index from 1.45 at the top to 1.42 at the bottom of the specimen. However, this deviation is still within the error margin of 1.44 ± 0.02 that was measured with the SH sensor.

Hence, this angle measurement confirms the SH analysis by an alternative approach and illustrates the limits of the described PSF simplification. The refractive index of the tissue is not perfectly homogeneous. Both, the SH analysis, as well as the angle measurement showed small deviations and slight depth dependence of the refractive index. However, for the investigated 100μm thick slices from cortical tissue and for quantitative tracing of neuronal morphology, these deviations are of a negligible amount.

Influence of background estimation

Since the modeled PSF resembles that of the measured one of the imaging system as shown above, a deconvolution should significantly improve the image quality in terms of SNR and resolution. However, the estimation of the background value can have a significant influence on the performance of a MLE filter [99]. I therefore checked the loss in signal and background for three groups of structures. First, dendrites in the absence of the much fainter axons were investigated and second, axons in the absence of dendrites. The third group contained both, dendrites and axons. Figure 3.3 (bold markers refer to mean values) shows the relative signal and background loss for the three groups and for two algorithms (TM and MLE). Whereas the background reduction is essentially independent of the structure

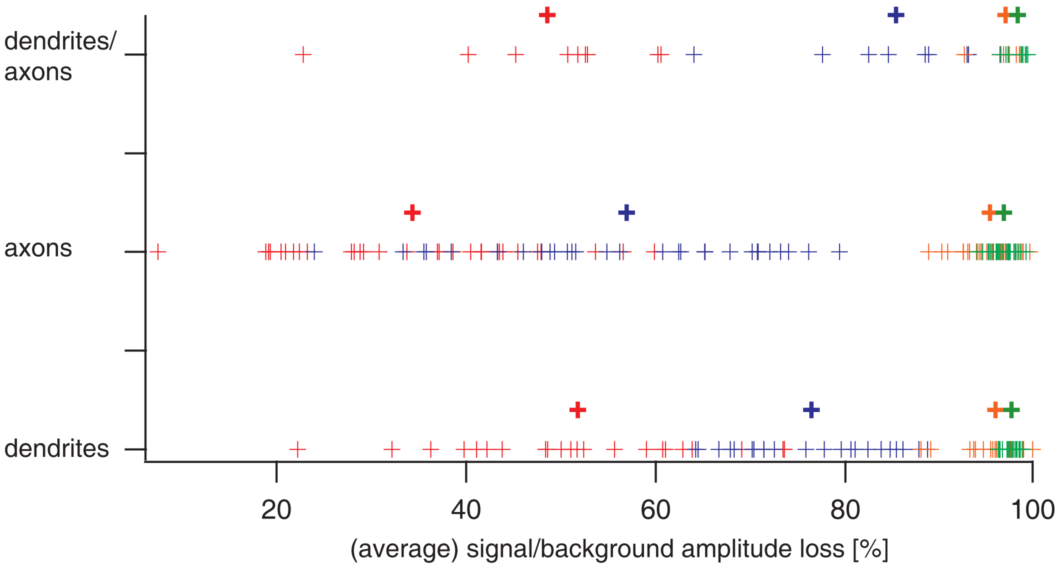

Figure 3.3: **Deconvolution of axons.** *Illustration of performance of two different deconvolution filters for three distinct groups of structure. Whereas the TM (signal/background reduction = red/orange) filter treats stacks containing only dendrites, axons or axons in the presence of dendrites in a similar way, the MLE (blue/green) algorithm tends to fade away the fainter axonal structures in the presence of more intense dendrites. Figure adopted from [83].*

type and deconvolution algorithm, the loss in signal amplitude differs significantly. The tendency that the MLE algorithm decreases the signal amplitude more than the TM filter holds for all three groups. However, whereas the average decrease in signal amplitude is usually much less than the reduction in background, this is not the case for axons surrounded by dendrites. These axons lose around 85% of their signal amplitude, on average. This means that faint structures, in the presence of much more intense structures, tend to fade after application of a MLE deconvolution filter. In consequence, an authentic tracing of axonal arbors from TLB mosaic image stacks is impossible without the application of a linear TM filter.

3.2.2 Automated vs manual reconstruction

State of the art technique for the 3D reconstruction of neuron morphology especially of the largely extending axonal arbors is the computer-aided interactive Camera Lucida technique (e.g. Neurolucida, [81]). Therefore the performance of the semi-automated reconstruction method is compared to such a manual reconstruction approach, as implemented with the Neurolucida system.

First it is checked whether manually traced branches are detected by the automated system and vice versa. I quantified whether branches are missed by either of the reconstruction approaches. In a second comparison step the relative deviation in shape between manually and automatically traced neuronal structures is determined. Finally the time frame for reconstructing complete cells with their entire axonal arbor was compared with the conventional method systems. The comparison is done for 54 slices containing 4 different filled cells (from 4 different rats). They were randomly chosen from a pool of already manually reconstructed cells. Each manual reconstruction was done by a different individual. Users manually traced a L2/3 pyramidal neuron, two star pyramids from L4 and one thalamocortical VPM axon.

Number of identical branches

Each automatically reconstructed cell was inspected for missing branches that have been traced by the manual system and vice versa. The amount of manually reconstructed branches that were missed by the automatic system was similar for all four traced neurons. 5.4% were missing for the thalamocortical VPM axon, 3.5% and 3.4% for the L4 neurons and no manually reconstructed branch was missing for the L2/3 neuron.

In the case of branches that were missing in the manual tracing but found by the automated system, the result was less homogeneous. Approximately 4% of automatically reconstructed branches were missing in the manual version of the thalamocortical VPM axon, 29% and 47% were missed for the L4 neuron and almost 70% of the automatically traced branches were not found manually for the L2/3 neuron.

For the 4 cells, the automated method missed 29 of 682 manually reconstructed branches in 54 sections from 4 different rats. In other words the new reconstruction technique found 96% of the manually reconstructed branches. The manual tracings were missing 268 of 923 automatically reconstructed branches from the same 54 slices. This means only 71% of the neuronal structures traced by the automated method could be found in the manual reconstructions. All of the missing branches, independent of whether they were missed by the manual or automatic system, were part of the axonal arbor. The dendritic branches were traced equally reliable by the two methods.

The amount of missing structures varied widely between 4% and almost 70%. The missed branches can be grouped into two cases:

- The first group consists of branches that were filled and stained but do not belong to the cell of interest. In some cases surrounding neurons take up the tracer molecule, and some of their dendrites or their main axon will be traced.

- The second group comprises neuronal structure that was missed by the human tracer. The user usually starts tracing at the soma. If an axonal branch ending is missed in that section, the human tracer tends to ignore these areas in the subsequent sections and therefore sometimes misses large parts of the axonal branching patterns. In some cases this error becomes obvious during splicing. Then the human tracer has to go back to the tissue and needs to identify the connections missed previously.

The size of the group of missing branches is closely correlated to the experience of the user. Only training, double checking and anatomical knowledge will minimize the loss of branches and improve the manual tracing quality. On the contrary, the automated system fails if the staining of the axon is insufficient, if the background is too high or in the presence of a strong gradient in thickness or contrast within the tissue. The latter will result in different optimal camera exposure times depending on the location of the field of view within the scanning pattern. Since the exposure is set to one value for the entire pattern this may result in a failure of the subsequent deconvolution and neuron tracing.

Another limitation is that, due to the small diameters and tortuous paths of axons combined with physical resolution limits of the system, two close lying axons may occasionally be mistakenly connected by the automatic tracing algorithm. However, resultant loops in the axon arbor are automatically detected by the SpatialGraphEditor and can be manually dissolved by the user.

Shape deviations of identical branches

A fractal box counting method described in detail by [61] was applied to 167 randomly picked branches from the 54 slices that were reconstructed by both methods. It yields that the relative deviation in shape is almost 0% at the lowest fractal resolution, meaning a box size of 5μm. With increasing resolution (decreasing box size), the deviation increases to a value of around 2% at a box size of 1μm and further to more than 3% at a resolution of 500nm. At the highest measured resolution of 300nm the relative shape difference was around 5%. This difference mainly arises from the larger number of points used by the automatic system to represent the graph and will hence be neglected.

Reconstruction time

The average amount of time for a manual tracing of one cell (10 to 30 sections), including its axonal arbor, is approximately 60-90 working hours. This means the reconstruction of a single brain slice takes between 4 and 6 hours. Using the automatic system, an image size of 1.5mm x 1.5mm x 100μm proved to be sufficient for most slices. The computing time for an image stack of this size varies from 3 to 6 hours, depending on the amount of structure within the volume. The human interaction time with the system is on average 30 minutes per slice. This comprises the setting up of the scanning pattern (5 minutes), as well as the manual editing and splicing of the automatically reconstructed slices (5-60 minutes). Therefore the average amount of time for reconstructing one cell with the semi-automatic system is between 30 to 90 hours of computing and 10 to 20 hours of human interaction. Given a working day of eight hours the reconstruction using the manual system takes around two weeks, whereas the automatic system can yield a comparable reconstruction within 2-4 days.

Chapter 4

Anatomical results

NeuroCount and NeuroMorph proved to be reliable methods. They are hence used to reengineer the excitatory part of the thalamocortical lemniscal pathway in the whisker system of rats. Therefore, as derived in the introduction chapter, the number and distribution of neurons and neuron-types in the VPM and S1 needs to be known. Further, a representative samples of dendrite morphologies for every excitatory neuron-type in S1 and of thalamocortical axon morphologies from the VPM towards S1 needs to be traced. Only if the deviation in neuron numbers, distributions and average neuron-type anatomy are small, this pathway can be regarded as an *anatomical* and functional subunit. If this prerequisite is fulfilled, the animation of an average cortical column *in silico* with average measured activity will potentially yield new insights into the mechanisms of neuronal information processing.

So far, this essential anatomical issue could not clearly be answered in a quantitative way. This is mainly due to two problems:

- First, manual sparse sampling methods resulted in total neuron numbers deviating by up to 50% (i.e. 200-300 neurons per barreloid [125], 10000-20000 neurons per barrel column (unpublished data by Verena Wimmer, Hanno-Sebastian Meyer and Bert Sakmann)). Such margins would make any simulation upon an average network unfeasible.

- Second, whereas manual tracing of the rather localized dendrite morphologies proved to be reliable (see chapter: Methodical results), it is problematic for axonal arbors (e.g. thalamocortical VPM neurons). The manual tracing of a single VPM axon takes about 90 hours and can only be performed by an expert user (personal communication with Thorben Kurz, MPIN).

NeuroCount and NeuroMorph solve these problems by yielding accurate three-dimensional neuron distributions and reliable axon tracings.

- First, NeuroCount determines the absolute number of neurons in some cubic millimeter large volumes of S1 and VPM with high precision.
- Second, NeuroMorph allowed for the tracing of fourteen thalamocortical VPM axons within one year. In addition 5 intracortical axons from slender tufted pyramidal neurons in L5A could be reconstructed.

Hence, all presented axons are reconstructed by the NeuroMorph system, whereas most of the subsequently presented 78 dendrite tracings are manually done, using Neurolucida. Evaluation of the resultant anatomical data revealed the following results:

1. Previously obtained large deviations in absolute neuron numbers in S1 are due to inhomogeneous distributions across and within cortical layers.
2. The deviation in total neuron numbers for an average cortical barrel column and a single VPM barreloid is less than 3% and 5%, respectively.

3. The 78 dendrite tracings from S1 group into 8 anatomical excitatory neuron-types.
4. The 5 axon tracings from slender tufted pyramidal neurons in S1 display characteristic innervation of L2/3 of multiple surrounding columns.
5. The 14 VPM axons group into two anatomical types, innervating a single or two columns respectively. In addition, 8 of these 14 tracings innervate columns of which the respective whisker has been continuously trimmed for two weeks. These tracings display a significant reduction in axonal length and density.
6. The number and subcellular distribution of VPM synapses is highly position- and neuron-type-dependent.
7. Spiny stellate neurons in L4 and thick tufted pyramidal neurons in L5 display on average the highest number of potential thalamocortical VPM synapses.
8. **The functional unit called *cortical barrel column* can also be regarded as an anatomical one, who's dimensions are defined by the VPM innervation volume and neuron-dense regions in S1.**

4.1 Quantitative 3D structure of S1

All available data in the literature about neuron densities and distributions in the cortex is based on sparse sampling [34], [35], [33], [36], [37]. This method resulted in rather contradicting density values (e.g. ranging from 40000-80000 neurons per cubic millimeter in V1).

The commonly referenced quantitative study about neuron densities and numbers in S1 was done by Clermont Beaulieu in 1993, using sparse sampling by the so called dissector method [32]. There, a 137μm wide strip of tissue ranging from the pia to the WM was manually investigated in 100μm thick thalamocortical sections. Such a small volume ($\approx$10% of the column volume) will only yield reliable density values for entire S1, if this region of the cortex is more or less homogeneous in every lateral direction.

In order to ultimately reveal the three-dimensional neuron organization of S1 and to quantitatively determine the number of neurons per barrel column, a 1,875mm x 1,875mm x 2mm large volume of S1 has been subjected to NeuroCount. This volume, being about 250 times larger than the one used by Beaulieu, contains at least nine complete cortical columns. It will be shown that the resultant neuron density values per layer, for entire S1 and hence for cortical columns, significantly differ from the previous estimates by Beaulieu. This can be explained by strong density variations within and across all cortical layers in S1, as displayed in Figures 4.1, 4.2, 4.3, Table 4.1 and described below.

4.1.1 3D distribution of neuron somata in S1

The investigated $\approx$8 cubic millimeter large volume of S1 contains nine complete cortical barrel columns (here: C2-4, D2-4 and E1-3 (Fig.4.1)). The column outlines are easily visible in low magnification images of the GAD channel in sections from L4 (Fig.4.1). These GAD outlines are identical to the barrels first observed by Woolsey and van der Loos [38]. Figure 4.1 and 4.2 show the distribution of all neuron somata in each of the 40 consecutive tangential brain slices (50μm thick), starting at the pia and ending at the white matter. It should be emphasized the the colormap is adjusted for each panel to display the respective density maximum and minimum of each slice in red and blue and hence to visualize the neuron organization within each section.

Subsequently the organization of each layer will be briefly summarized. It should be

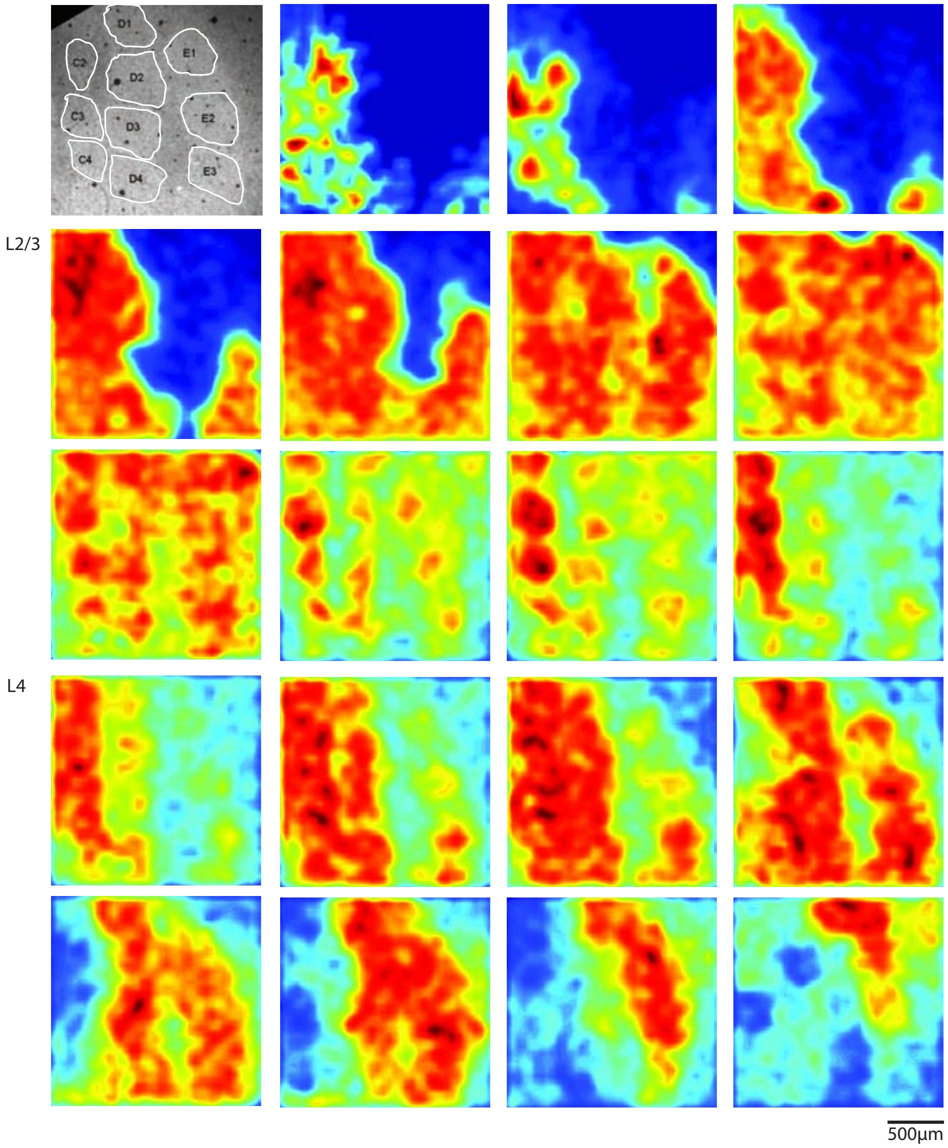

Figure 4.1: **3D neuron soma distribution in L1-L4 of S1.** *Top/left panel: low magnification image of GAD channel in a section from L4. Clearly visible are the barrel outlines, identical to the ones first observed by Woolsey and van der Loos. These contours determine the x/y-center of each column. Remaining panels: starting at the pia, the distribution of all neuron somata in a 1875µm x 1875µm x 50µm volume as derived by NeuroCount is displayed. The colormap is adjusted for each slide (i.e. the respective maximum density is red, minimum blue). The GAD barrel pattern is preserved in the neuron soma distribution of L2/3 and L4.*

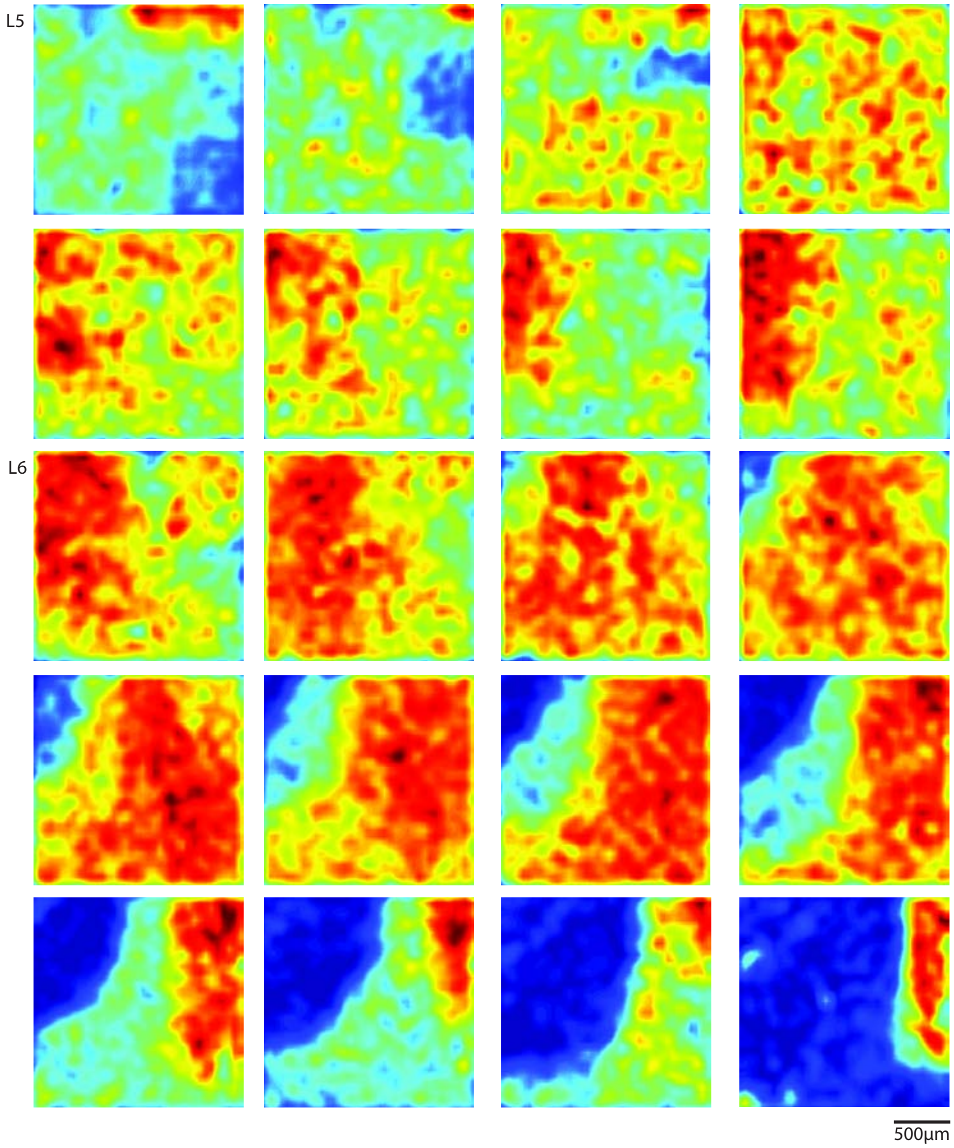

Figure 4.2: **3D neuron soma distribution in L5-L6 of S1.** *Remaining 20 sections from Fig.4.1. Clearly visible are small clusters of neurons in L5, which could resemble so called mini-columns as described by [126]. The last section is not show, because it is completely within the WM and hence no neurons are present.*

mentioned that the cortex is a curved structure. Looking at the first panels of Figure 4.1, it is obvious that the c-row is about 75μm (1.5 sections) higher than the d-row, which in turn is 75μm higher than the e-row. Consequently some panels cannot clearly be assigned to one or the other layer.

Organization of L2/3 Panel 4-8 of Figure 4.1 approximately comprise L2/3. This layer displays strong density variations, ranging from ≈50000-110000 neurons per cubic millimeter. Further, the organization which is determined by the GAD image (panel1) is preserved in L2/3. Cortical columns appear there as neuron-dense circles, having approximately the same diameter as the respective GAD contours. The columns in L2/3 are surrounded by neuron-sparse zones, called septa. The average difference between columnar and septal zones is about 15%. The average density value for entire layer 2/3 is ≈74600 neurons/mm^3.

Organization of L4 Panel 9-16 of Figure 4.1 approximately comprise L4. As L2/3, L4 displays strong density variations ranging from ≈80000-170000 neurons per cubic millimeter. In contrast to L2/3, septa between individual columns of the same row are almost absent. However, septal regions between the rows are even more pronounced than in L2/3, especially between the d- and e-row. The average difference between columnar and septal zones is again around 15%. The average density value for entire layer 4 is ≈104600 neurons/mm^3.

Organization of L5 Panel 1-8 of Figure 4.2 approximately comprise L5. The clear organization in rows or columns is absent and replaced by strong density variations on smaller scales. Small dense zone of density values up to ≈90000 neurons per cubic millimeter are intersected by small neuron-sparse zone with densities of ≈40000 neurons per cubic millimeter. No clear pattern can be seen. Hence, the average difference between columnar and septal regions is around zero. Neuron-dense zones could possibly reflect so called minicolumns, defined by bundles of apical dendrites and described by [126]. The average density value for entire layer 5 is ≈67900 neurons/mm^3, making L5 the neuron-sparsest layer in S1.

Organization of L6 Panel 8-16 of Figure 4.2 approximately comprise L6. As in L5, L6 displays no clear neuron organization. A more or less homogeneous distribution is intersected by randomly arranged neuron-sparse zones. These deviations range from ≈40000-110000 neurons per cubic millimeter. Even though the sparse zone seem to be organized randomly, the difference between columnar and septal regions is about 8%. The average density for entire layer 6 is ≈73200 neurons/mm^3.

Summarizing these layer-specific descriptions, the somatosensory sensory cortex is organized into neuron-dense columns and neuron-sparse septa throughout all layers, except for L5. The average density values peak in L4 and have their minimum in L5 (L1 is neglected, because it is not innervated by the VPM). The average density value of entire S1 is ≈71000 neurons/mm^3, comprising columnar (≈73800 neurons/mm^3) and septal (≈69000 neurons/mm^3) regions. The total difference between these two zones is hence about 7%. These findings are summarized in Table 4.1 and illustrated by Figure 4.3. There, average intensity projections along all three spatial directions of the investigated volume in S1 are shown. The x/y-projection (bottom plane), resembling a top view from the pial surface, clearly depicts the organization of S1 into rows that are divided by prominent septa. Regarding the x/z- and y/z-plane it becomes further obvious that cortical barrel columns are not only functional units, but can be regarded is neuron-dense columns that are separated by septa throughout entire S1. The septa are very prominent in L2/3 and L4 ($\approx -15\%$), almost absent in L5 and somewhat less discernable in L6 ($\approx -8\%$).

The density value for S1 in the commonly referenced study by Beaulieu [33] (Table 4.1) is

	Beaulieu 1993		Oberländer 2009					
Layer	total	GABA	total	GABA	column	septum	≈min	≈max
1	5.3	81	7.1	80	5.3	8.8	4	80
2/3	52.6	15	74.6	14	80.4	68.8	50	110
4	85.7	11	104.6	14	111.6	97.6	80	170
5	36.1	17	67.9	18	69.0	66.9	40	90
6	48.3	16	73.2	9	72.6	73.8	40	110
S1	47.5	15	71.0	17	73.8	69.2	42.8	92.2

Table 4.1:

Comparison of average neuron densities and fraction of GABAergic interneurons per cortical layer in S1 between results from sparse sampling (i.e. dissector) [33] and NeuroCount. Neuron densities are given in $10^3/mm^3$*, whereas the fraction of GABAergic interneurons is given in %. The layer boundaries differ from the estimates done by Beaulieu and are derived in section 4.3.1. Each layer is very heterogeneous in density. Hence, sparse sampling methods can yield average densities ranging from ≈40000-90000. The true average density is 71000 neurons per cubic millimeter. The fraction of GABAergic interneurons is similar between the two studies.*

$\approx 35\%$ less than the here presented one. This underestimation is systematically found for all layers. Most likely this can be explained by strong density variations within each layer. Previously published density values for rat cortex obtained by sparse sampling methods range from $40000 - 80000$ neurons$/mm^3$. This is approximately the range if the here determined minimal and maximal values per layer are averaged (Table 4.1). In the case of Beaulieu, the density values are close to the minimal average density of S1 as determined here.

Further quantification of these findings is done by counting the number of neurons in the nine standardized column regions and a surrounding box shown in Figure 4.4a. The midpoint of each of the nine barrel regions is determined as the center of mass of the respective GAD-contours. Circles with radius 195.44μm are centered on each of these midpoints. This radius is adopted from [6] and has been established by measurements of the extend of VPM synapse distributions in L4 (personal communication with Verena Wimmer and Bert Sakmann). The resultant columnar cross-section of $120000\mu m^2$ yields a column volume of $0.24mm^3$. Compensating for curvature artifacts the number of neurons in each of the nine columns and in the remaining box area yield three-dimensional neuron distributions and depth-profiles (Fig.4.4c) for the average column and the septum, respectively. The resultant numbers are subsequently presented.

4.1.2 3D average cortical column of neuron somata

As stated above, the number of neurons per standard column (i.e. cylinder with 120000 μm^2 cross-sectional area and $0.24mm^3$ volume) is calculated for nine columns within the large volume of S1. The resultant distributions and numbers are given in Figure 4.4b and 4.4c, respectively. The curvature of the cortex is compensated by shifting the distributions of the c-row by 75μm and the ones of the e-row by 150μm. Two observations are remarkable:

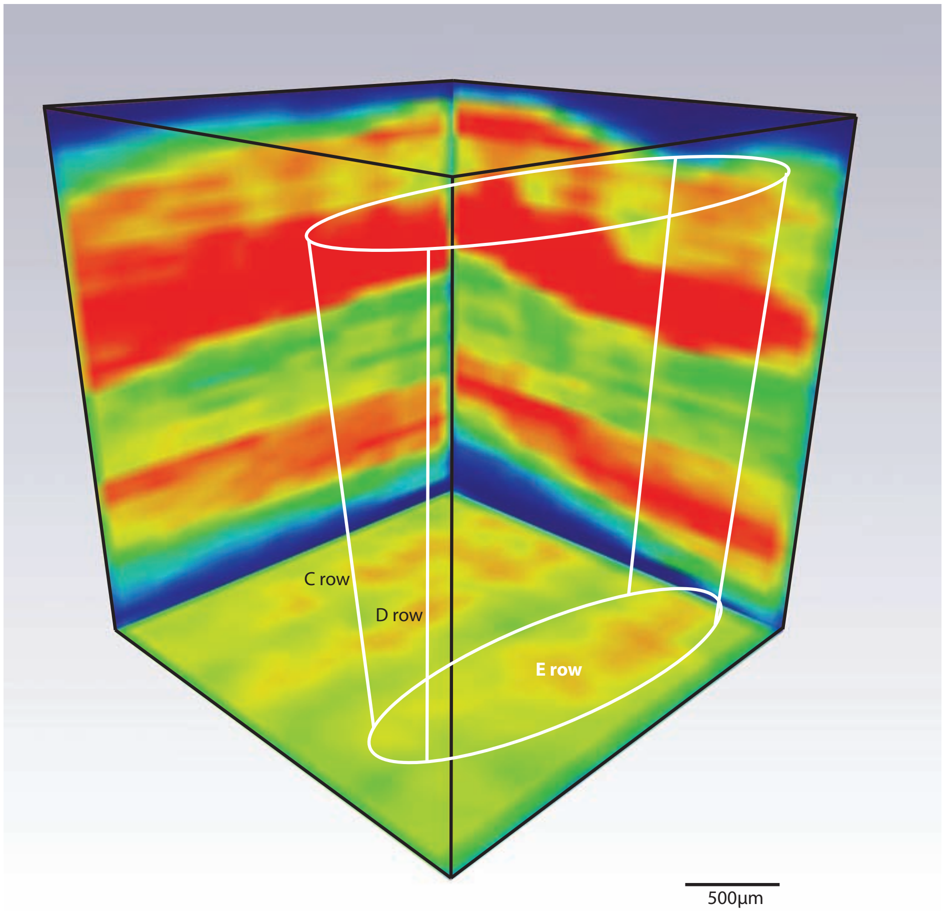

Figure 4.3: **3D neuron soma distribution in S1.** *Average x/z-, y/z- and x/y-projection of neuron densities in S1. Clearly visible is the organization of the barrel cortex in neuron-dense column, separated by neuron-sparse septa. The septa between rows are much more prominent than between columns of the same row. Hence, the cortical barrel column is not only a functional but also an anatomical subunit in terms of three-dimensional soma distribution.*

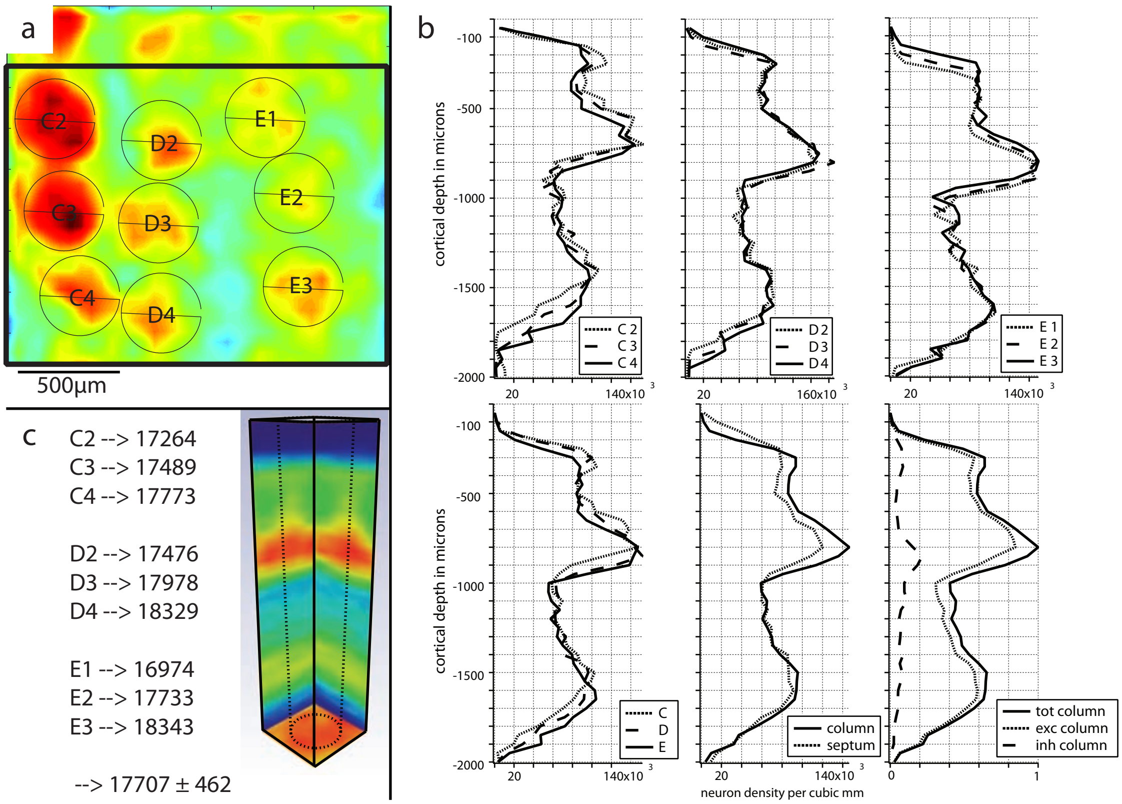

Figure 4.4: **Neuron soma distribution of average cortical column.** *(a) A circle with 195.44μm radius is centered on each column midpoint as determined by the GAD contour. (b) The number of neurons is calculated for each circle in each slice. The resultant depth profiles are shown for each row (three top panels). Compensating for curvature artifacts the average depth profile is determined (bottom left panel). Calculating the number neurons within the remaining box shown in a, additionally yields a depth profile of the septum (bottom middle panel). By subtracting the depth profile of GABAergic interneurons, the distribution of excitatory neurons can be calculated (bottom right panel). (c) The average number of neurons per cortical barrel column is 17707±462. The low deviation in numbers and the identical profiles allow the creation of an average 3D neuron distribution, centered on a cortical column (right panel). The resultant distribution will be the starting point for reengineering the excitatory thalamocortical lemniscal pathway.*

- First, the circle with 195.44μm radius resembles almost exactly the maximal dimensions of the neuron-dense area in L4 (Fig.4.4a C2 and C3 are already in L4).
- Second, the deviation between individual columns is considerably small. Here, the average number of neurons per column is 17707 ± 462 (i.e. the standard deviation between columns is less than 3%).

The small deviation in absolute numbers and almost identical distributions and profiles for the nine columns, allows to calculate the average three-dimensional neuron distribution of a cortical barrel column. Therefore a cuboid with 550μm x 550μm x 2000μm edge length is centered around each column midpoint and cropped from the large distribution. The resultant nine cuboid distributions are averaged and the result is shown in Figure 4.4b. Subtracting the fraction of GABAergic interneurons, as determined in cooperation with Hanno-Sebastian Meyer (MPImF, Heidelberg) [38] and shown in Figure 4.4c (bottom/right panel), the three-dimensional distribution of all excitatory neurons in this standard cuboid volume ($0,605mm^3$) is derived. The total fraction of interneurons is about 15%, resulting in a number of excitatory neurons of ≈15200 per standardized column.
The cuboid distribution will in the following be the starting point for the reengineering of the excitatory thalamocortical lemniscal pathway in S1. Subsequently the number of neuron-types that constitute to this distribution as well as their spatial extend will be determined.

4.1.3 Dendritic excitatory neuronal cell types in S1

In total a number of 78 dendrite tracings of excitatory neurons from S1 are evaluated. The 78 reconstructions are registered to the standardized column using daVinci, as described in the method section. *In vivo* physiological data of spontaneous suprathreshold activity

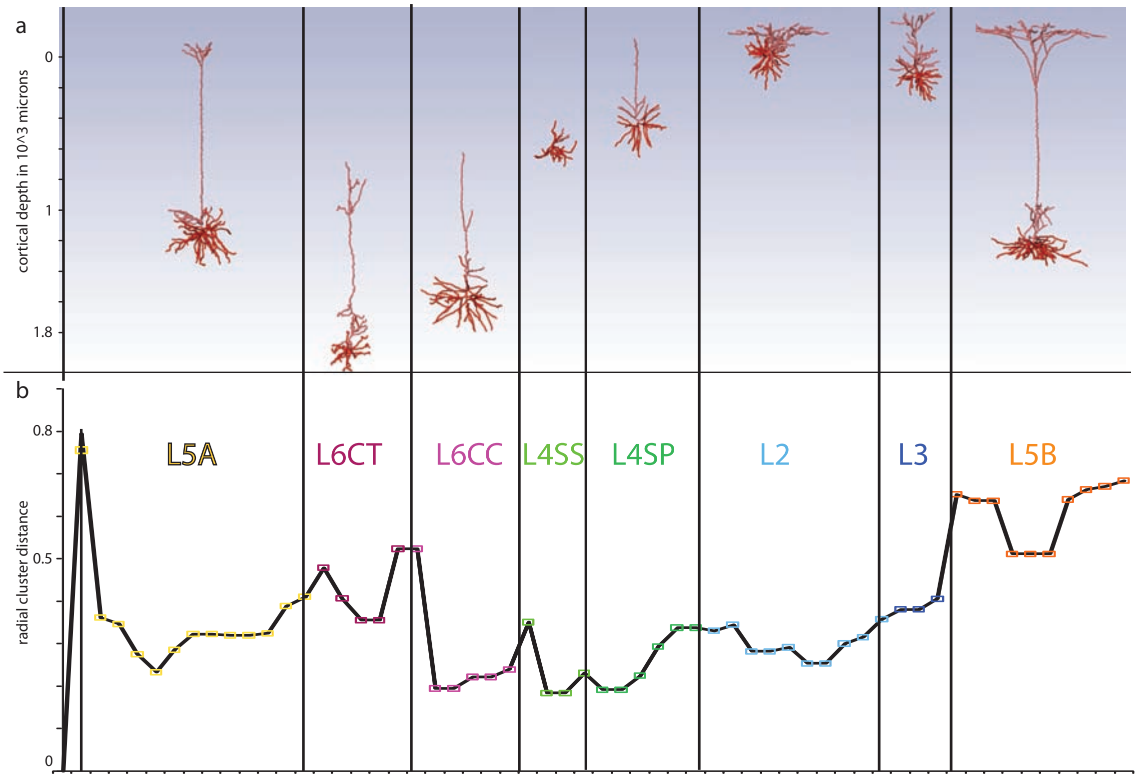

Figure 4.5: **OPTICS cluster results in S1.** *(*a) A representative dendrite tracing for each of the determined eight neuron-types is shown at its standardized, registered soma depth. (b) The OPTICS algorithm used by NeuroCluster produces an augmented reachability plot, where valleys indicated individual clusters. Six neuron-types are clearly found, L5A, L6CT, L6CC, L4, L2/3, and L5B. Further, L4 and L2/3 can be separated into two subtypes respectively, L4SS,L4SP, L2 and L3.

and in response to passive whisker deflection (i.e evoked activity) under anesthesia is also available for 60 of these tracings. This gives the unique opportunity to classify excitatory neuron-types based upon anatomical features and cortical depth and to correlate these anatomical classes with physiological properties.

NeuroCluster, as described in the method section, is used to group the tracings upon geometry- and shape-related dendritic features, as well as by cortical depth. Figure 4.5b shows the resultant reachability plot. Six individual neuron-types could be clearly determined as ”valleys” in this plot. In addition two layer-specific subtypes (i.e. less prominent ”sub-valleys”) could be assigned in L2/3 and L4, respectively. A representative neuron tracing is shown for each of the eight types (Fig.4.5a) at its standardized registered soma depth. The features of each class can be described as follows:

Layer 2 pyramid (L2) These neurons form a subclass within L2/3. Characteristic for these neurons is a very short and usually oblique (with respect to the column axis) apical dendrite with a widely spreading apical tuft. The obliqueness is mainly due to their position within the top 100-400 microns of the column. There the curvature of the pial surface constrains the apical innervation.

Layer 3 pyramid (L3) These neurons form the second subclass within L2/3. The transition from L2 neurons to L3 is rather gradual, which is also indicated in the reachability plot. Therefore, L2/3 is often regarded as a single layer of more or less one excitatory neuron-type [16]. However, characteristically, L3 neurons are found deeper within L2/3, resulting in a still short but straight (with respect to the column axis) apical dendrite. Moreover their apical tuft is less prominent and spreads not as wide as the one of L2 neurons.

Layer 4 star pyramid (L4SP) These neurons form a subclass within L4. As previously described by [127], these neurons display a short apical dendrite with a sparsely, if at all, branching apical tuft. As presented below (see sec.4.3.1), there is a significant overlap between L2/3 and L4. Within this overlap zone the transition from L3 to L4SP neurons is again somewhat gradual, making manual classification difficult.

Layer 4 spiny stellate (L4SS) These non-pyramidal neurons form the second subclass within L4. As L4SP neurons, L4SS neurons were previously investigated by [127]. They are completely lacking an apical dendrite and display a characteristic asymmetric shape, caused by dendrites that usually point towards the column center. Their name is also due to high spine densities, which in the following is estimated as twice as high as for any of the other eight types.

Layer 5 slender tufted pyramid (L5A) These neurons form an unambiguous class in L5 and were first described in rat visual cortex by [128] and have since then been investigated in various cortical areas [129]. Characteristically. L5A neurons have a long, unbranched apical dendrite and a moderately spreading apical tuft. The latter feature gave this type its name.

Layer 5 thick tufted pyramid (L5B) These neurons form the second unambiguous class in L5 [128], [129]. In contrast to L5A neurons, L5B neurons display heavy branching at the apical ”root”, called oblique apical dendrites and a widely spreading apical tuft. Again the latter feature resulted in the name of this class.

Layer 6 corticocortical pyramid (L6CC) These neurons form an unambiguous class in L6. They display a wide basal tree, sparsely branching apical oblique dendrites and a sparsely spreading, if at all, apical tuft. They were first described by their axon morphology from *in vitro* tracings [130], [131]. Projecting mainly within the cortex resulted in the classification as corticocortical.

Layer 6 corticothalamic pyramid (L6CT) These neurons form a second unambiguous class in L6. They display a narrow basal tree, oblique apical dendrites, a long apical trunk and a sparsely branching apical tuft. They were also first described by their axon morphology from *in vitro* tracings [131]. In contrast to L6CC neurons, this type projects from S1 towards the thalamus, resulting in the name corticothalamic L6 neuron.

The here objectively determined neuron types have all been described before. Nevertheless, the grouping is usually done subjectively and is mainly based upon soma depth. It will be shown in section 4.3.1 that this "recording" depth can sometimes be misleading because these neuron-types mutually overlap in the z-direction. In contrast, the reliable classification by NeuroCluster is based upon dendritic, anatomical features and the standardized pia-soma distance of each reconstruction. The unambiguity of the presented eight neuron-types is demonstrated on the example of three of the eleven features (see method section) and is shown in Figure 4.6a/b.

Figure 4.6a displays the neuron-type-specific distribution of apical tuft length compared with standardized pia-soma distance. The ellipses are centered around the respective mean values and the length of the half axes is set to 1,5 times the standard deviations. Figure 4.6b is created in a similar way by replacing the length of the apical dendrite with the maximal horizontal spread of the apical tuft. The ellipses hardly overlap. This indicates that each neuron-type has unique anatomical features, which distinguish them from each other. Since L4SS has no apical dendrite, L4SS and L4SP cannot be distinguished by these parameters and are hence grouped as one type in the illustration.

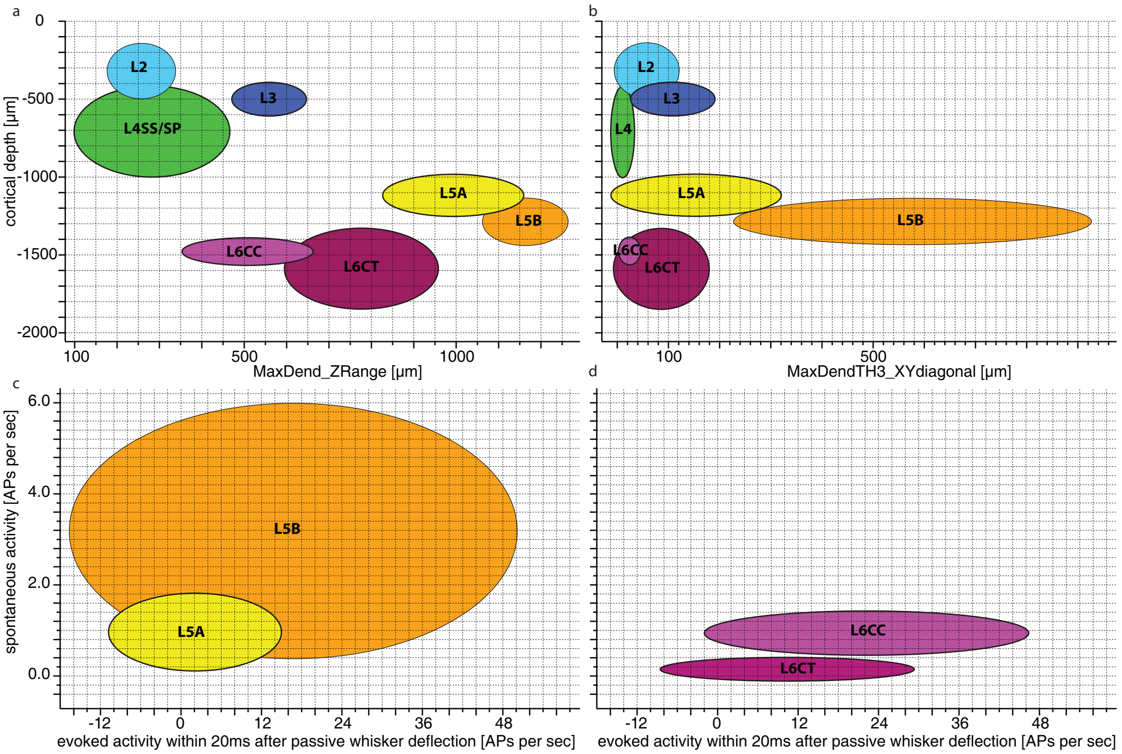

Figure 4.6: **Anatomical and physiological neuron types.** *(a/b) Scatter-plots showing the neuron-type-specific relationship of registered soma depth and length of the apical dendrite (a) and spread of the apical tuft (b). L4SS neurons have no apical dendrite and can therefore not be distinguished from L4SP neurons upon these features. The ellipses are centered around the type-specific mean values and the length of the half axes is set to 1,5 times the standard deviation. Small, if any, overlap zones between the ellipses indicate anatomically well separated clusters. (b/c) Spontaneous and whisker-evoked activity are plotted as in a/b for L5 (c) and L6 (d) neurons. Small, if any, overlap zones between the ellipses indicate that the anatomical types also reflect type-specific functional properties. The results for L5 were previously shown* in vivo *[10]. For L6 these findings were predicted from* in vitro *studies [131] and can now be confirmed* in vivo.

Correlation of anatomical and functional type-specific neuron properties

Apart from anatomical features, neuron-types are often grouped by their physiological response properties. This will be illustrated on two examples:

- A significant difference between L5A and L5B neurons is their response to passive whisker deflection. Whereas L5A neurons remain more or less silent, L5B neurons respond the most among all neuron-types [10]. If the grouping of L5 pyramidal neurons by NeuroCluster is correct, this physiological feature should be present if the mean whisker-evoked and spontaneous activities are compared. This is done in Figure 4.6c. The ellipses are again centered on the respective mean values and their sizes reflect 1,5 times the standard deviation. Clearly separated ellipses demonstrate that L5A and L5B are not only anatomical but also physiological classes. The evoked activity within the first 20ms after whisker deflection mainly represents direct activation by thalamocortical VPM input. The difference in response could hence reflect different dendritic properties (e.g. ion channel distributions) or different synaptic input. The latter will be addressed in section 4.3.2.

- Predicted by [131], L6CC should have higher firing rates *in vivo* when compared with L6CT neurons. There, *in vitro* current injections revealed that the intensity need to elicit APs in L6CT is significantly higher than in L6CC neurons. Both, the spontaneous and whisker-evoked activity are shown for L6CT and L6CC neurons in Figure 4.6d. The activity rates of L6CT neurons are significantly lower than the ones for L6CC. Further, the two ellipses do not overlap, indicating that the anatomically classified two neuron types in L6 are also physiological types.

The process of tracing, standardizing and clustering dendrite morphologies reproduced anatomical and physiological findings. Hence, the above presented eight neuron types will be subsequently investigated further. First the corticocortical axon innervation is studied on the example of L5A neurons. Ultimately, these neuron types function as target populations for thalamocortical VPM projections, yielding a neuron-type-specific number of potential VPM-S1 synaptic contacts.

4.1.4 Axonal projections of L5A neurons within S1

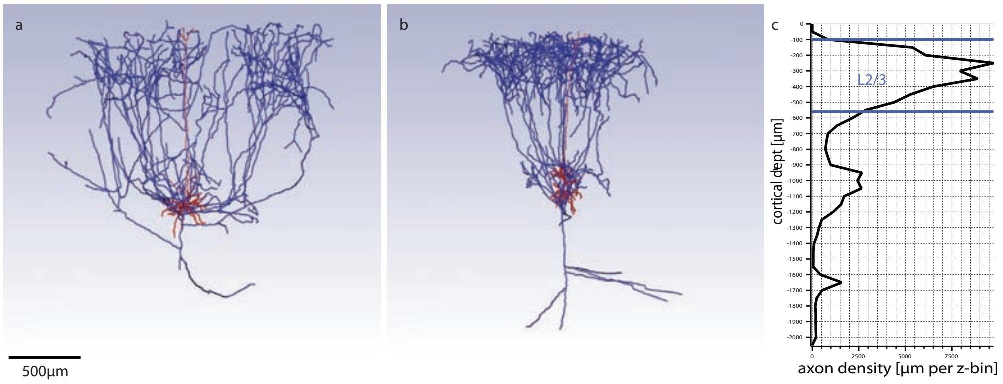

Figure 4.7: **Axonal projections of slender tufted L5A pyramidal neurons in S1.** *(a/b) Three-dimensional tracing of full axon (blue) and dendrite (red) morphologies from* in vivo *labeled L5A neurons. Despite large variability in axon morphology, all traced neurons display characteristic projections into L2/3 of the surrounding columns and to L5 of its own column. The wide-spreading axon morphology prohibits the quantitative tracing from* in vitro *preparations. (c) Average axon density profile for L5A neurons. 9cm average total axon length innervate S1 most densely in L2/3 (reaching a peak at 300µm depth) and in L5A (reaching a peak at approximately 1000µm depth).*

So far, the tracing and classification revealed eight excitatory dendritic neuron types in S1. Subsequently these neurons will be investigated as targets for thalamocortical input from the VPM. However, this VPM-S1 circuit is only the starting step for cortical processing of whisker-evoked sensory information. Any of the determined neuron-types processes and then transfers information towards other neuron-types, before it is ultimately relayed to subcortical areas.

The only possibility to quantify these neuron-type-specific intracortical circuits, is to trace the complete axonal arbor of classified cortical neurons. Here, this procedure is demonstrated for L5A neurons reconstructed by NeuroMorph.

A few *in vitro* studies [24], [132], [25] showed that L5A neurons project into supragranular layers L2/3 and L1. Unfortunately, *in vitro* reconstructions suffer from significant slicing artifacts. An *in vitro* slice thickness of usually 300μm will prove to be insufficient to study the full extend of the axonal arbor in a quantitative manner. Figure 4.7a/b show two of five reconstructed L5A neurons including their full dendritic (red) and axonal (blue) morphology. Regarding the scalebar it becomes obvious that a slice thickness of 300μm will always result in significant cropping of these axonal arbors.

Table 4.2 summarizes the length of axon and dendrites for the five traced L5A neurons. These numbers illustrate the different efforts needed for tracing axons or dendrites. L5A neurons comprise on average about 9cm of axon, compared to approximately 6mm of dendrite. This amount of axon per cell has significant implications. As will be derived below (Table 4.8) L5 contains approximately 1700 L5A neurons per barrel column. Assuming a bouton density that is similar to the one of VPM axons (1 bouton per 3μm), the number of potential corticocortical L5A synapses on axons projecting out of a single column would be more than 50×10^6. For comparison, this is about 20 times more than the total number of thalamocortical VPM synapses per barrel column (sec.4.2.2 and Table 4.8).

In addition to the potential number of L5A synapses, Figure 4.7c shows that their main innervation domains are located within L2/3 (peak at 300μm depth) and L5A itself. Further, despite relatively large morphological deviations between individual cells, all L5A axons share characteristic innervation patterns. Unbranched projections cross L4 and target L2/3 of the same and multiple surrounding columns. There, the axon branches frequently again. Whereas L5A projections in L2/3 span across large areas of S1, in some cases even beyond S1 into the "agranular cortex" (i.e. lacking a high cell density layer), the axon stays essentially local within its home column in L5.

The tracing of the full three-dimensional axonal arborization of L5A neurons in S1 hence suggests the presence of at least three corticocortical circuits:

L5A-to-L5A projection The first circuit suggested by the axon tracing is a local (intra-columnar) circuit within L5A. Such monosynaptic connections between pairs of L5A neurons were recently described in *in vitro* studies [133].

L5A-to-L2/3 projection The second circuit suggested by the tracing of L5A axons is a long range circuit within S1. The morphology suggests that information of whisker movement, which is processed within the paralemniscal pathway, is conveyed from L5A to L2/3 of the same and multiple surrounding columns. In addition to the recent finding that L2/3 neurons are sensitive to whisker movement [134], the here presented tracings support the hypothesis of monosynaptic connections between L5A and L2/3 neurons [22]. Since L2/3 neurons are also part of the lemniscal pathway, which processes information about whisker touch, the presence of L5A-L2/3 connections would indicate convergence of the lemniscal and paralemniscal pathways in L2/3 [22].

L5A-to-AGr projection The third circuit suggested by the tracing of L5A axons is a long range circuit with L2/3 neurons of the agranular cortex (AGr). This cortex is involved in sensorimotor processing [135], [136], [137]. A monosynaptic connection between these populations has to my knowledge not yet been demonstrated. Direct transfer of information about whisker movement from L5A in S1 to L2/3 in AGr, without further processing in S1, is suggested by these projections.

	length [mm]		
♯	axon	basal dendrites	apical dendrite
1	87,31	4,09	2,85
2	83,50	4,64	1,66
3	77,82	6,03	1,14
4	95,01	5,23	n.t.
5	119,16	4,02	n.t.
AVG	92,56	4,80	1,14
STD	16,13	0,84	1,20

Table 4.2:

Dendritic and axonal length of L5A pyramidal neurons (n.t. means "not traced", i.e. the apical dendrite was partly destroyed during filling).

The tracing of intracortical axonal arbors, demonstrated on the example of slender tufted pyramidal neurons in L5 of S1 illustrated two important issues.

- First, the reconstruction of such axon morphologies is almost unfeasible by manual tracing. A total axon length of up to 12cm and unpredictable innervation domains will make a Neurolucida-based tracing tedious, time consuming and experience dependent.

- The second issue is related to the fact that the innervation domains are rather unpredictable. Like "bulk-labeling" studies of entire neuron populations [138], tracing of individual axons potentially yields new information about network circuity (e.g. an estimate of the number of synaptic contacts). However, ”bulk-labeling” studies are rather descriptive, whereas single neuron tracing yields quantitative three-dimensional information about innervation density.

4.2 Quantitative 3D structure of VPM

The aim of the presented work is to reengineer the excitatory part of the thalamocortical pathway in the whisker system of rats. So far the focus was on the target populations of VPM axons in S1. There, eight individual neuron-types could be classified by their dendrite morphology and position within a standardized cortical barrel column. There, a total number of ≈15200 excitatory neurons are potentially targeted by the VPM.

In order to derive neuron-type-specific data of how many thalamocortical synapses are potentially formed with any of these 15200 neurons, and to estimate how the synapses are distributed throughout the column, the following anatomical information about VPM is necessary:

1. the number of neurons that project from the VPM into a single column (i.e. the number of neurons per barreloid),
2. the three-dimensional distribution of VPM axons in S1 (i.e. a representative sample of single VPM axon tracings),
3. the number of boutons (potential sites for synapses) per axonal length,
4. overlap of VPM axons and cortical dendrites.

Using NeuroCount and NeuroMorph this information will subsequently be presented in a quantitative way.

4.2.1 3D distribution of neuron somata in VPM

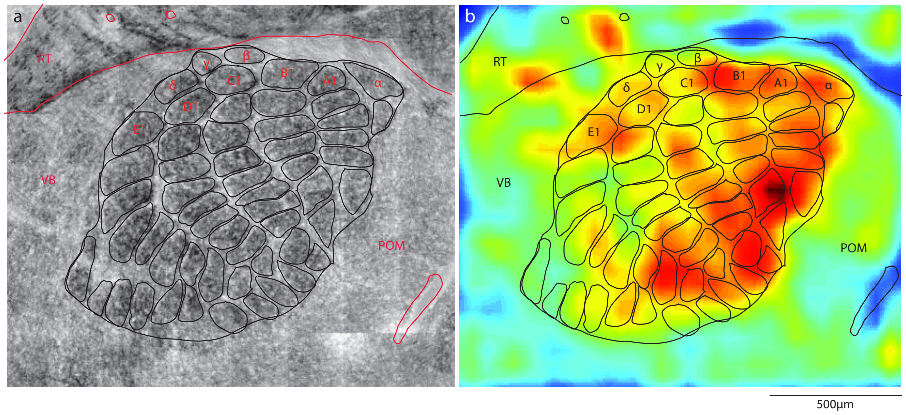

Figure 4.8: **GABAergic innervation of VPM.** *(a) Inverted maximum intensity projection of GAD-channel from a central slice through VPM. No interneurons are present except in RT. The VPM and each individual barreloid is clearly visible indicating that GABAergic neurons from the RT innervate mainly the VPM in a barreloid- and/or row-specific way. (b) The GAD-contours are transferred to the neuron (NeuN-stained) density map obtained by NeuroCount. The VPM boundaries based upon the GABAergic innervation from the RT are reflected in the neuron density. The VPM is hence regarded as a neuron-dense thalamic nucleus surrounded by less dense VB and POm.*

In previous studies of the VPM a number of approximately 200-300 neurons per barreloid [125] has been estimated. Even though this estimate seems to be rather precise, the uncertainty of about 20% (250 ± 50) will be reflected in the range of VPM synapse per barrel column. Arguably, 20% uncertainty in synapse numbers would make simulation of neuronal activity upon an average cortical column unfeasible. Therefore, as presented for S1 previously, NeuroCount is used to determined the number and three-dimensional distribution of neurons from a large thalamic sample. Here, nine 50μm thick sections, cut at an oblique angle as described by [139] are stained with NeuN and GAD67. Large image stacks ($\approx 1,7mm$ x $1,7mm$), acquired by confocal mosaic/optical-sectioning and centered around the VPM are obtained for each of the nine sections.

Figure 4.8 summarizes the two main findings:

1. The VPM does not contain GABAergic interneurons, but still displays characteristic structural organization in the GAD-channel, caused by GABAergic synaptic terminals. Figure 4.8a shows an inverted maximum intensity projection from a central section through VPM. Clearly visible are individual barreloids, rows of barreloids, septa between the rows and a significant intensity drop outside the VPM (i.e. in VB and POm). Further, GABAergic interneurons are only found in the RT. This indicates, as described by [140], [141], inhibitory connections between the RT and the VPM. This innervation seems to be restricted to the VPM, defining its boundaries with respect to surrounding thalamic nuclei. More importantly, the RT innervation seems to be barreloid-, or at least row-specific, defining the boundaries of individual barreloids and rows, similar to the findings in S1 (Fig.4.1). The barreloid boundaries, visible in the GAD-channel, are traced as contours within each of the nine sections. Alignment of these contours results in a three-dimensional reconstruction of individual barreloids. In consequence the volume of each barreloid can be calculated.

2. Superimposing the GAD-contours of the VPM and its barreloids with the respective neuron density distribution yields another important finding. The VPM differs not only in GABAergic innervation from its surrounding thalamic nuclei, but also in neuron density. Almost identical VPM boundaries are obtained in the GAD projection image and the NeuN density distribution (Fig.4.8). However, unlike the barrel contours in S1, the barreloid contours do not reflect neuron-denser areas within the VPM. There, septa seem to be purely defined by the GABAergic innervation from

the RT.

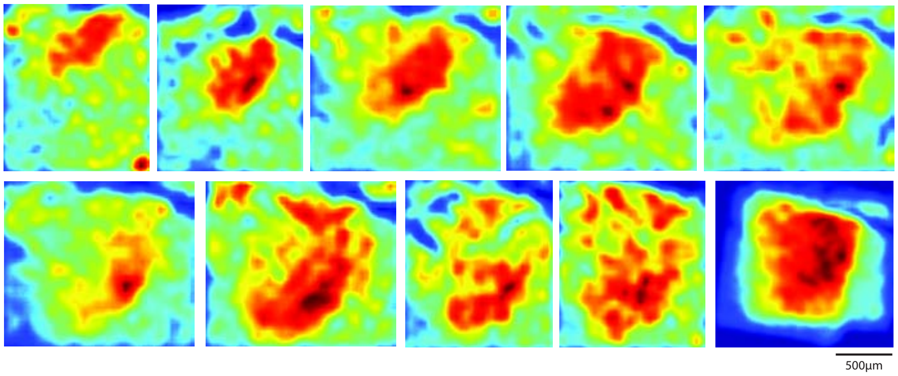

Figure 4.9: **3D neuron soma distribution in VPM.** *NeuN-density distribution for nine consecutive oblique brain slices. The VPM is clearly separated from its surrounding nuclei. The bottom/right panel displays an overlay of the nine sections.*

Figure 4.9 shows that the described confinement of the VPM from its surrounding nuclei is true for every section. The red and yellow parts in each section correlate with the respective GAD-pattern. Superimposing all NeuN-density maps (last panel in Fig.4.9) again illustrates that the VPM can be regarded as a neuron-dense nucleus surrounded by the neuron-sparse VB and POm.

Quantitatively, the number of neurons is determined for 4 barreloids (C1,C2,D1,D2). For each section the respective barreloid contours are superimposed with the NeuN landmark distribution (each landmark represents the 3D position of a soma) in Amira. All landmarks found within the GAD-boundaries of a barreloid are detected. Table 4.3 shows the counts for each of the four barreloids in each section. No significant structure within one barreloid is present. As stated above, the VPM is rather homogeneous in neuron density.
The investigated four barreloids have almost identical volumes ($4,69 \pm 0,14 \times 10^6 \mu m^3$), which approximately resemble ovoids with 50μm x 100μm x 200μm long half axes. The

	number of neurons					
slide	C1	C2	D1	D2	AVG	STD
1	28	39	17	28		
2	49	42	21	19		
3	40	39	21	30		
4	31	32	19	31		
5	33	43	54	41		
6	26	31	24	37		
7	39	40	46	31		
8	41	19	43	33		
9	10	9	26	26		
SUM	297	294	271	276	285	13
volume $[\times 10^6 \mu m^3]$	4,80	4,72	4,73	4,49	4,69	0,14
density per $[\times 10^3 mm^3]$	61,81	62,25	57,22	61,49	60,69	2,34

Table 4.3:*Number of neurons per VPM barreloid.*

resulting number of neurons per barreloid is 285 ± 13. This number is well within the margin of 200-300, but deviates by less than 5% in comparison to the previous uncertainty of 20%. It should be emphasized that even though the VPM seems to be the most neuron-dense thalamic nucleus, its average density of $60,69 \pm 2,34 \times 10^3 mm^{-3}$ is 15% less than the average density of S1 and even 40% less if compared with L4 (in S1).

4.2.2 Axonal excitatory neuronal cell types in VPM

In addition to the number of neurons that project from one barreloid into one cortical barrel column, the three-dimensional axon distribution of VPM axons within S1 needs to be quantified. Therefore fourteen thalamocortical axons, filled *in vivo*, have been traced with the NeuroMorph system, standardized by daVinci and grouped by NeuroCluster. Eight of these axons projected into columns where the corresponding whisker has been continuously trimmed for two weeks. The two main results can be summarized as follows:

1. VPM neurons are grouped by NeuroCluster into two types upon their axon morphology. Figure 4.10a/b and Figure 4.10d/e show examples for these two types, respectively. As described before [142], these types differ in the number of innervated columns. Four of fourteen axons display a bifurcation in L6 and innervate two columns. However, one column still contains the major part or the axon.

   The remaining ten axons innervate only a single column. As shown in Figure 4.10c/f, both types innervate S1 most densely in L4 and have a second, significantly smaller peak in L5B. The innervation abruptly stops within L2/3 around 300μm below the pial surface. Further, the depth profiles display a significant minimum in L5A, around 1000μm below the pial surface. It should be emphasized that the lateral extend, especially in L4, matches the estimated column diameter of 390,88μm (cross-sectional area $120000 \mu m^2$, see sec.4.1.1).

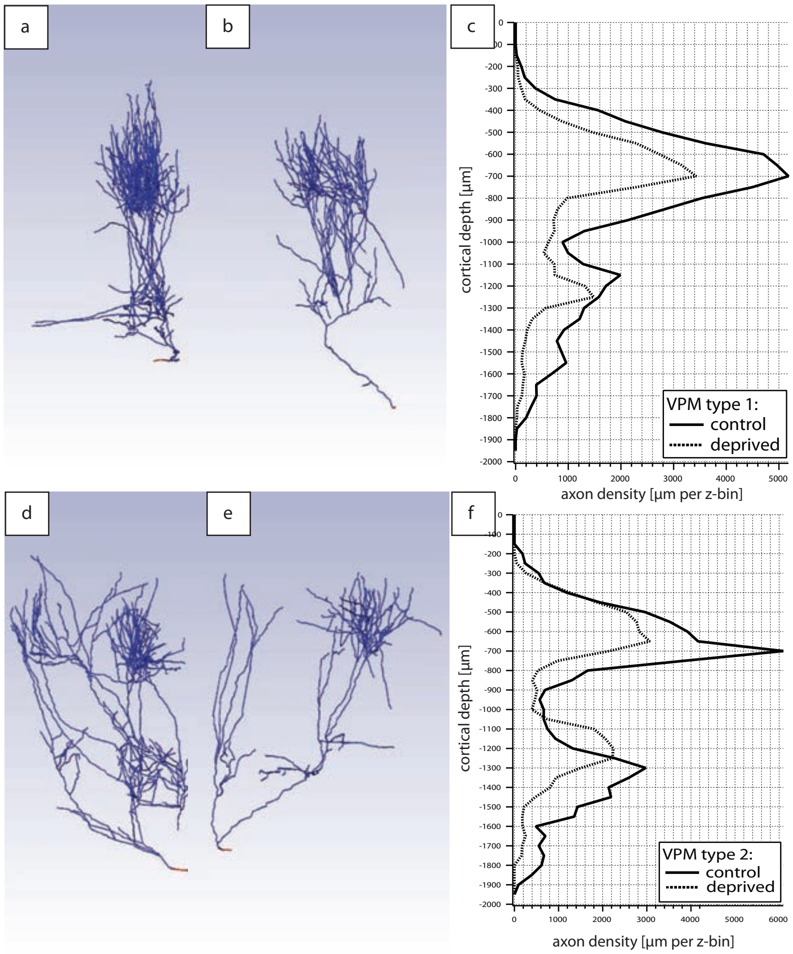

Figure 4.10: **Classification and deprivation of VPM axons.** *(a/b) Two example tracings of the cortical part of thalamocortical VPM axons projecting into a single cortical barrel column. The tracing in b projects into a column where the corresponding whisker has been continuously trimmed for two weeks (deprived). (d/e) Two example tracings of VPM axons that bifurcate in L6 and project into two adjacent barrel columns. The tracing in e corresponds to a deprived whisker. (c) Average deprived and control axon density profiles for tracings projecting into a single column. (d) Same profile as in c for tracings projecting into two columns.*

2. Table 4.4 shows the axon length for deprived (whisker trimmed) and control tracings, respectively. In the control case, VPM axon have an average length of $56,95 \pm 13,08$mm. In the deprived case of $42,31 \pm 15,03$mm. Hence, the VPM axon length in control animal is 34% larger when compared to the deprived animals. The absence of functional input hence results in a diminishment of axon branches and therefore thalamocortical connectivity within a cortical barrel column. Specifically, the axon decrease is more pronounced in L4 and L6. In contrast, the average axon density remains almost unchanged in L5A and decreases less in L5B.

   The determined deprivation-depended decrease in thalamocortical VPM axon is supported by a recent bulk-labeling study [143]. There, VPM axons were labeled with a virus expressing a fluorescent protein. The VPM innervation density was estimated by measuring the fluorescent intensity in S1. Between control and deprivation a difference in fluorescence of ≈34% was also observed. However, it remained unclear if the decrease in fluorescence reflected a decrease in bouton numbers, axonal length or both. Further, the possibility that the fluorescent marker depends on neuronal activity could not finally be excluded. The single axon tracings support strongly the hypothesis in [143] that continuous deprivation of whiskers results in significant functional long-term changes, which is based on anatomical plasticity of VPM-S1 projections.

The control group of VPM tracings will be subsequently used to reengineer the thalamocortical pathway and to interconnect the VPM with any of the previously presented excitatory neuron-types in S1. Therefore it is essential to know the number of boutons per axonal length, since boutons are potential sites for synaptic contacts. I therefore measured the distance between pairs of boutons manually, using Neurolucida software in combination with a 100x magnification oil-immersion objective. Since boutons are small swellings along

control		deprived	
type	length $[mm]$	type	length $[mm]$
single column	68,15	single column	32,20
single column	59,27	single column	17,52
single column	68,78	single column	48,67
single column	51,87	single column	55,83
single column	33,52	single column	58,36
double column	60,09	double column	56,29
		double column	28,65
		double column	40,89
AVG	56,95	AVG	42,31
STD	13,08	STD	15,03

Table 4.4: *VPM axon length with and without whisker trimming.*

the axon arbor ($\approx 1\mu m$), they are hardly visible for axons projecting along the optical axis. Hence, only axons projecting more or less perpendicular to the optical axis are investigated. The distance for 300 pairs of boutons at random cortical depth and for different axons and animals has been measured. The resulting bouton density of $2,94 \pm 1,15$ will therefore subsequently be regarded as constant (i.e. 3 boutons per μm axon) throughout the entire VPM axon.

4.3 3D reconstruction of lemniscal thalamocortical pathway

The above obtained results are sufficient to reengineer the thalamocortical lemniscal pathway in NeuroNet. As described in the method section NeuroNet needs the following input information:

3D target neuron distribution As derived in section 4.1.2, this distribution is a standardized cuboid centered around a cortical barrel column with dimensions of 550μm x 550μm x 2mm. The distribution is chosen sufficiently larger than the estimated column diameter of 390,88μm to avoid edge artifacts (i.e. neurons at the column border would otherwise receive too many synapses because of absent dendrites from septal neurons).

Number of target neuron-types As derived in section 4.1.3, eight excitatory neuron-types are classified in S1. For every of these types a representative sample of dendrite morphologies is available (i.e. 78 tracings in total). Further, any of these types will be connected to the VPM.

Number of input neurons As derived in section 4.2.1, 285 neurons are found in one barreloid. Further, the 6 VPM tracings of the control group, as described in section 4.2.2, function as a representative input sample.

Spatial extend of target neuron-types This issue has not been addressed so far and will hence be subject of the subsequent section.

4.3.1 The standardized 3D *cortical column in silico*

type	AVG recording depth [μm]	STD [μm]	AVG registered depth [μm]	STD [μm]
L2	346,5	93,7	299,6	130,0
L3	475,0	189,1	392,5	103,2
L4SP	781,8	116,8	670,8	176,0
L4SS	802,2	144,5	724,3	151,1
L5A	1131,7	124,2	1133,7	106,4
L5B	1220,4	76,2	1286,6	98,3
L6CC	1477,0	65,0	1502,2	86,2
L6CT	1577,5	111,3	1587,9	172,9

Table 4.5:*Neuron-type-specific average recording and registered soma depth.*

The standard cortical barrel column has been described as a cylinder with a radius of 195,44μm and 2mm height. However, the spatial extend of each neuron-type within this column remains undetermined. Since the cortex is a laminar structure, it is reasonable to assume that each neuron-type has only boundaries along the vertical column axis (z-axis). These are determined by calculating the average registered neuron depth (pia-soma distance) and its standard deviation of the standardized tracings of each neuron-type.

Table 4.5 shows these values for each neuron-type in comparison to the so called recording depth, which reflects penetration depth of the pipette during *in vivo* filling experiments. As stated in the method section, this is only valid if the penetration axis is parallel to the vertical column axis.

However, for infragranular neuron-types in L5 and L6, on average the recording and registration depth are similar. This is not the case for supragranular and granular neuron-types (i.e. L2, L3, L4SP, L4SS). The average recording depth is systematically deeper than the registered one. Table 4.6 shows the average ± 1,5× its standard deviation, minimal and

type/ **layer**	$AVG - 1.5STD$ $[\mu m]$	$AVG + 1.5STD$ $[\mu m]$	min $[\mu m]$	max $[\mu m]$	bounds $[\mu m]$
L2	104,7	299,6	87,5	481,6	100-500
L3	237,8	547,3	182,9	531,6	250-550
L2/3	151,1	527,8	87,5	531,6	100-550
L4SP	406,8	934,8	523,6	1000,1	400-950
L4SS	497,7	950,9	460,2	1020,8	500-950
L4	452,1	940,5	460,2	1020,8	400-950
L5A	974,2	1293,3	948,5	1350,4	950-1300
L5B	1139,3	1434,25	1130,0	1381,2	1150-1450
L5	1007,0	1388,0	948,5	1381,2	950-1450
L6CC	1373,0	1631,4	1409,4	1657,2	1350-1650
L6CT	1328,5	1847,4	1286,0	1725,1	1300-1850
L6	1343,0	1732,8	1286,0	1725,1	1300-185

Table 4.6:*Layer- and type-specific boundaries.*

maximal registered depth for each neuron-type and their respective layers. The minimal and maximal type-specific depths match the values of AVG±1,5×STD depths. Since the three-dimensional neuron distribution is given with 50μm precision, the boundaries for each neuron-type are rounded to the next z-bin. The resultant type- and layer-specific boundaries are given in Table 4.6 and are illustrated in Figure 4.11.

There, layer and type boundaries are compared with normalized depth profiles of excitatory and inhibitory somata and VPM axon density. Usually minima and maxima in one of these plots are used to determine type-specific neuron boundaries [144]. Specifically,

- L4 is centered around the maximum of the VPM or the excitatory soma distribution,
- L5A is centered around the infragranular minimum of the VPM distribution,
- L5B is centered around the infragranular maximum of the VPM distribution,
- L6 is centered around the infragranular peak of the excitatory soma distribution,
- and the border between L2 and L3 is determined at the end of the supragranular plateau of the excitatory soma distribution or at the supragranular end of the VPM distribution.

Even though the neuron-type-specific center depths, determined by the "profile-based" approach, are similar to the ones determined as the average registered depth, I prefer the latter method for two reasons:

- First, the relative central depth values for L4SS and L4SP, L6CC and L6CT cannot be set by the profile-based methods and would hence be assumed identical as L4 and L6.
- Second, the z-range cannot clearly be determined by the profile-based approach.

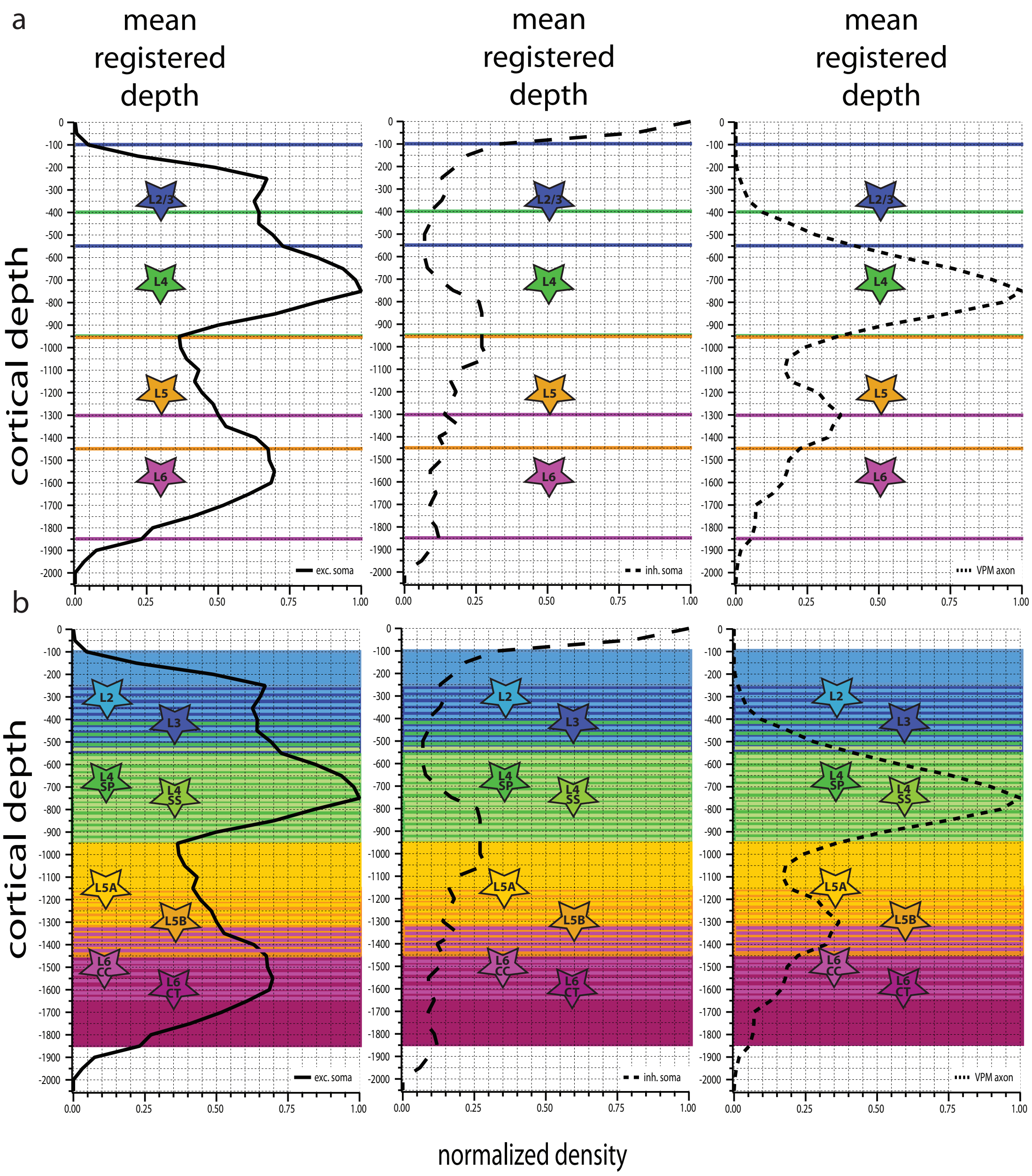

Figure 4.11: **Layer- and neuron-type-specific boundaries in S1.** *Layer- (top) and neuron-type- (bottom) specific boundaries along the vertical column axis are determined as the average registered depth of all tracings from a type ± 1,5× its standard deviation. These boundaries are shown with respect to the depth profile of excitatory and inhibitory somata and VPM axon density (from left to right), which are often used to determine type boundaries.*

depth [μm]	L2	L3	L4SP	L4SS	L5A	L5B	L6CC	L6CT
100-250	1							
250-400	1	3						
400-500	1	3	1					
500-550		1	1	3				
550-950			1	3				
950-1150					1			
1150-1300					1	1		
1300-1350						2	1	
1350-1450						2	1	1
1450-1650							1	1
1650-1850								1

Table 4.7: *Type-specific overlap ratios.*

Therefore, subsequently the registered depth-based boundaries in Table 4.6 will be used. The resultant overlap between neuron-types is indicated in Figure 4.11 as hashed zones and quantified in Table 4.7. There, the overlap ratios reflect approximately the relative frequency of occurrence of a neuron-type at a certain depth. For example, L2, L3 and L4SP neurons are found between 400μm and 500μm below the pial surface. The ratio of 1:3:1 is derived as the ratio of neurons from each type among the 78 tracings that can be found at this depth. In this case, the area between 400μm and 500μm is essentially occupied by L3 neurons (3 out of 5), but L2 or L4SP neurons can also be found at this depth (1 out of 5, respectively).

Once the neuron-type-specific boundaries and overlap ratios are set, NeuroNet determines the type, number and position of neurons for each 50μm voxel of the standard cuboid and replaces it by an appropriate dendrite tracing. Superimposing 285 VPM axon tracings (i.e. each of the 6 tracings is pasted about 45 times), the number and subcellular distribution of VPM synapses of any postsynaptic neuron is calculated by NeuroNet, as described in the method section, and presented below.

4.3.2 Number and 3D distribution of VPM synapses in S1

The standardized cuboid distribution of excitatory neuron somata in S1 results in approximately 40000 neurons. Each of these neurons is replaced by a dendrite tracing of its respective type. This results in a three-dimensional spine density, which is identical to the dendrite density but multiplied with constant neuron-type specific spine densities. For all types this density is assumed as 1 spine per 2μm of dendrite, except for L4SS, where a density of 1 spine per 1μm of dendrite is assumed. I am currently working on methods to determine more reliable spine density values, using serial block-face-scanning electron microscopy (SBFSEM) [145]. However, the absolute spine densities will not influence the

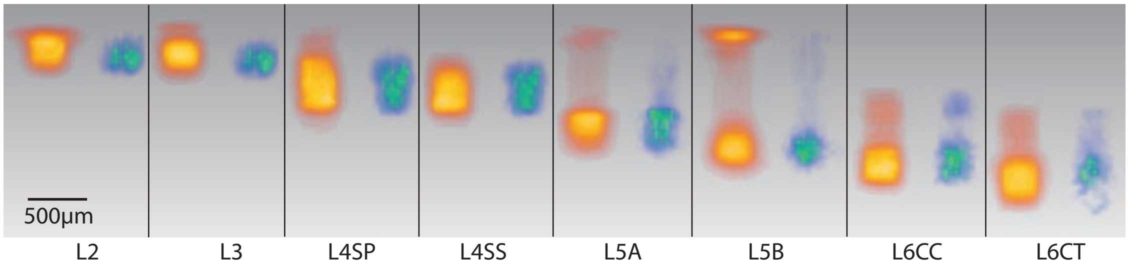

Figure 4.12: **3D neuron-type-specific spine and VPM synapse distributions.** *X/z-projections of neuron-type-specific spine (yellow) and VPM synapse distributions as derived by NeuroNet.*

calculation in NeuroNet. The relative densities between the types are decisive and it is reasonable to assume that L4SS neurons have a spine density twice as high as the other types.

The created spine density is superimposed with the bouton density, which reflects the axon density of 285 thalamocortical VPM axons, multiplied with a constant bouton density. As presented above, this density value is 1 bouton per 3μm of axon. Upon the eight neuron-type specific three-dimensional spine distributions (Fig.4.12 yellow), eight neuron-type-specific synapses distributions are calculated (Fig.4.12 blue). Therefore NeuroNet determines the contribution of every of the ≈40000 dendrite tracings to the total spine and bouton distributions, as described in the method section. Subsequently, only neurons with a soma position that is within the standardized column radius of 195,44μm will be evaluated. The remaining "septal" neurons will be neglected, since they might be effected by edge artifacts. The results of the three-dimensionally reengineered thalamocortical pathway can be summarized as follows (Table 4.8):

1. The here presented average cortical column contains 15289 excitatory neurons. The largest population is formed by L4SS, followed by L6CT neurons. The L4SS popu-

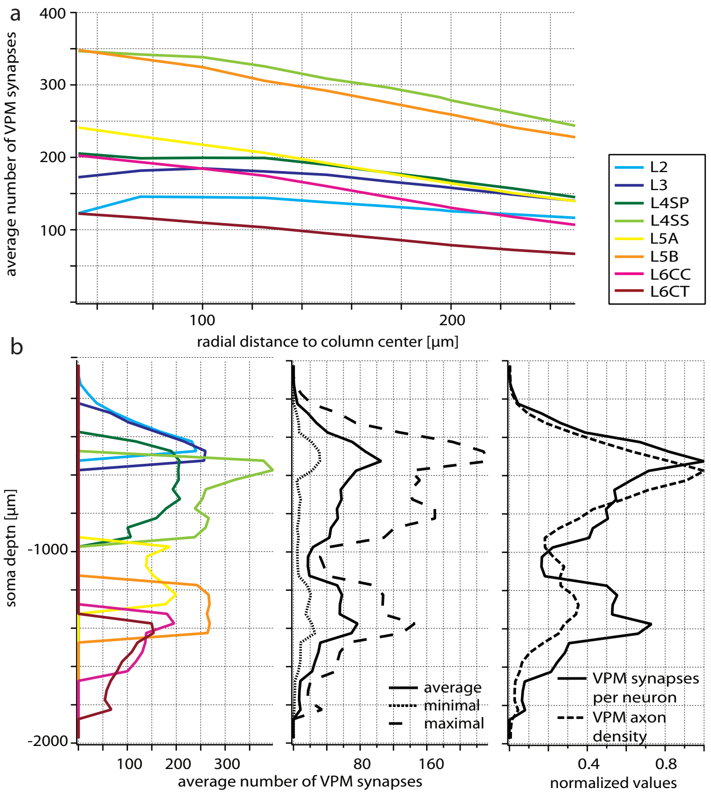

Figure 4.13: **Neuron-type-specific position dependence of synapse numbers.** *Depending on the neuron-type and its three-dimensional soma position within the column, the number of VPM synapses per neuron differ significantly. The upper panel shows the decay of the average number of synapses per neuron with respect to the distance of the soma from the column center. The lower panels show the average number of synapses per neuron with respect to the pia-soma distance (cortical depth).*

lation also comprises the largest number of spines ($\approx 16\times10^6$), but most spines per neuron are found in L5B (6644). In total, the here generated average postsynaptic network contains about 55×10^6 spines.

2. Most VPM synapses are formed with the L4SS population ($\approx 1{,}2\times10^6$). This is one order of magnitude more than for any other neuron-type. The total number of VPM synapses that are formed with the 15289 excitatory neurons of the average cortical barrel column is $\approx 2{,}8\times10^6$. As derived previously (sec.4.1.4) this is about 50 times less than the number of synapses L5A neurons from a single column form within S1.

3. On average, L4SS and L5B neurons have most synapses per neuron (283 and 262). Neurons of these two types have on average approximately twice as many VPM synapses than neurons of the remaining types. Specifically, if the average synapse numbers are divided by the number of VPM neurons (285), L4SS and L5B neurons are the only populations where on average, each postsynaptic neuron forms one synapse with each presynaptic VPM neuron.
   Further, the neuron receiving most VPM input in this network is a L4SS cell, making 948 synapses. Hence, given a convergence ratio of 0.43 [12], on average this neurons forms about eight synapses with every connected VPM neuron.

4. The number of synapses among neurons of the same type is strongly position dependent. Distance of the soma from the pial surface and/or the vertical column axis (i.e. column center) influence the number of synapses this neuron will form. Figure 4.13 illustrates this in a neuron-type-specific way. The upper plot shows that independent of the neuron-type, the number of VPM synapses decreases with increasing distance from the column center. However, the slope of this decay is type-specific. Whereas the lateral position of L2 neurons within the column has hardly any effect

on the number of synapses, L5B neurons at the column border form about 30% less synapses than neurons of this type at the column center.

Further, the three bottom plots in Figure 4.13 illustrate that neuron-type-specific VPM synapse numbers depending on the z-position of the soma. Specifically, the summed synapse profile is similar to the VPM axon profile, with one significant difference. The relative difference between the minimum in L5A and the maximum in L5B is significantly increased in the synapse profile. This means that L5A neurons between 950 and 1150μm below the cortical surface receive significantly less VPM input than L5A cells between 1150-1300μm.

type	neurons	spines		VPM synapses					
	total	total	AVG	total	max	AVG	max per	AVG per	radial
	♯	$\sharp \times 10^6$	♯	$\sharp \times 10^5$	♯	♯	VPM cell	VPM cell	decay
L2	718	2,87	3994	0,92	596	127,3	2,1	0,5	-0,10
L3	1682	6,05	3595	2,69	798	159,7	2,8	0,6	-0,20
L4SP	1524	3,52	2310	2,60	509	170,3	1,8	0,6	-0,30
L4SS	4128	15,98	3872	11,68	948	283,0	3,3	1,0	-0,53
L5A	1752	7,30	4168	2,92	392	166,5	1,4	0,6	-0,52
L5B	1135	7,54	6644	2,97	540	261,9	1,9	0,9	-0,62
L6CC	1373	4,10	2989	1,83	357	133,3	1,3	0,5	-0,50
L6CT	2977	7,97	2677	2,39	273	80,3	1,0	0,3	-0,29
SUM/AVG	15289	55,34	3781	27,99	552	172,8	1,9	0,6	-0,38

Table 4.8: *Thalamocortical lemniscal pathway in numbers.*

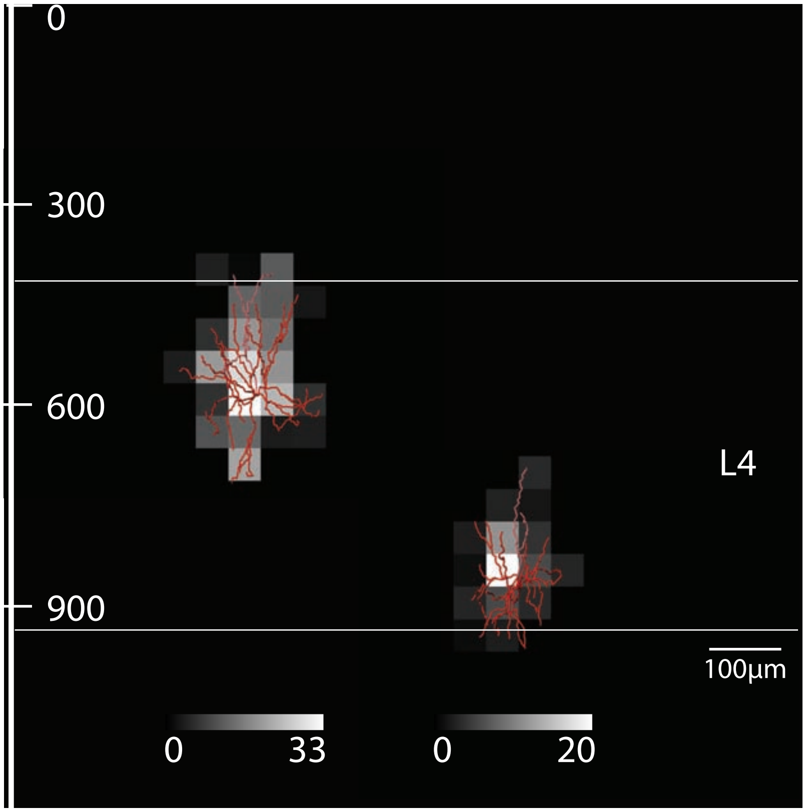

Figure 4.14: **Subcellular distribution of VPM synapses in L4SS neurons.** *Different dendritic length, as well as position within the column, cause significant differences in total VPM synapse numbers on L4SS neurons; 406 synapses (left) vs. 105 synapses (right).*

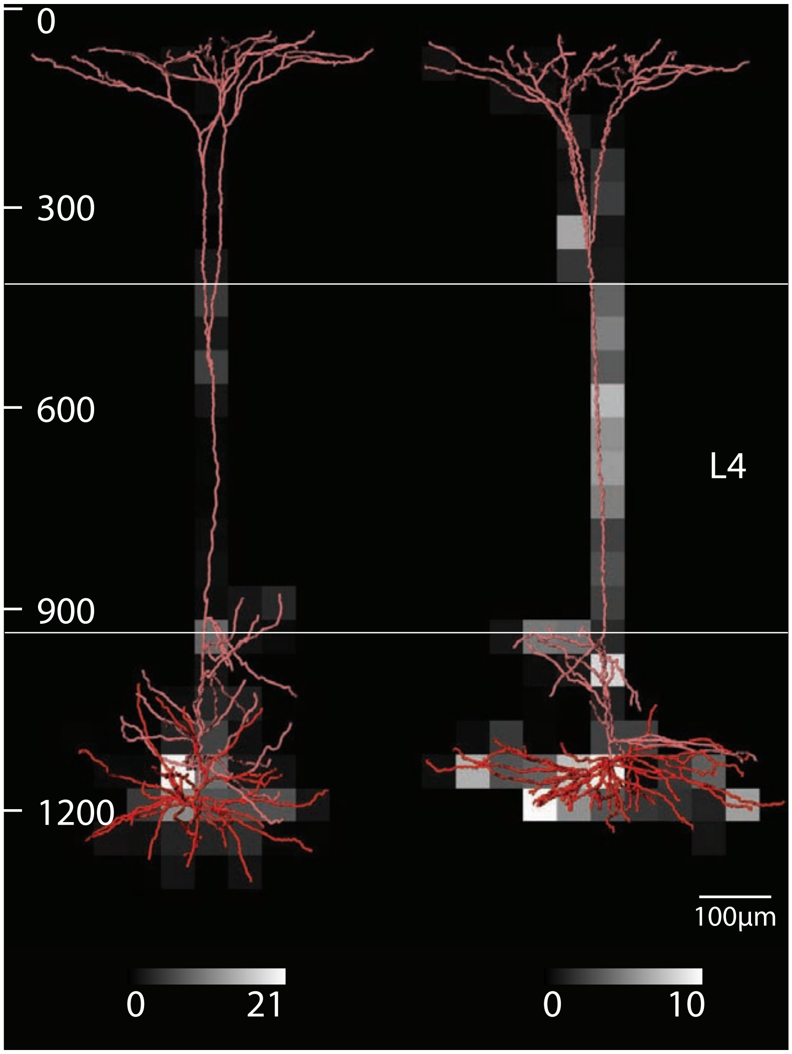

Figure 4.15: **Subcellular distribution of VPM synapses in L5B neurons.** *Two example L5B tracings from the average "cortical column in silico" are superimposed with an x/z-projection of their respective VPM synapse distribution. This distribution is radially symmetric in the basal tree, having its peak usually around the soma. In most cases a second innervation peak is found along the apical trunk within L4. Almost no VPM synapses are present in the apical tuft. The same kind of innervation has been described previously [123].*

Very little is known about numbers and distributions of thalamocortical VPM synapses in S1. To my knowledge only three recent studies yield information that can be used to validate the presented results by NeuroNet.

1. *In vivo* recordings from all excitatory neuron-types in S1 demonstrated, that L4SS and L5B neurons respond the most to passive whisker deflection, within 20ms after the stimulus [10]. This fast increase in AP-rates is regarded as directly caused by thalamocortical VPM synapses.

   The above presented results, based on innervation statistics of an average cortical column, yield that exactly these two neuron-types receive most VPM input. The *in vivo* results hence support these findings.

2. Based on *in vivo* paired recordings of VPM and L4SS neurons, the number of synapses for this connection-type is estimated as 600, but maximally slightly less than 1000 [12]. As derived above, L4SS receive on average 283 synapses, which is only half as much as predicted. However, the number of synapses, especially for L4SS neurons is strongly position dependent (Figure 4.14). The average number of VPM synapses in the upper part of L4 is about 400 (Fig.4.13 bottom/left panel). Further, the number of synapses differs by more than 20% between the column center and its border areas (Fig.4.13 top panel), reaching even maximal values of 948 VPM synapses per neuron. In consequence the estimated limit of slightly less than 1000 synapses per L4SS neuron is never crossed by any of the L4SS neurons in the presented average network.

   In conclusion, the gross estimate of 600 synapses per L4SS neuron is certainly met by a large fraction of the here presented L4SS population. Further, it can be assumed that during paired recordings, synapse estimates are biased by the fact that only functionally connected neurons are investigated, resulting in slight overestimation of synapses numbers.

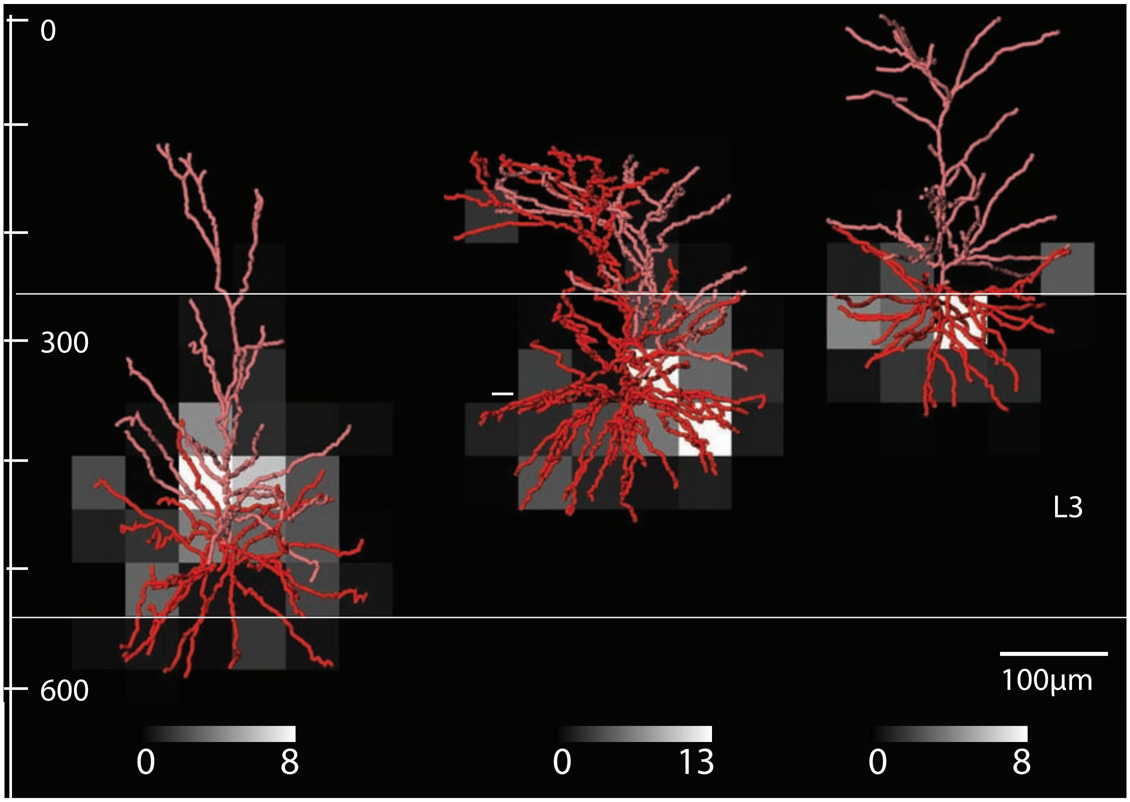

Figure 4.16: **Subcellular distribution of VPM synapses in L3 neurons.** *The average, soma-centered synapse distribution of L3 neurons displays a characteristic shift towards the lower parts of the basal dendrites [123]. This effect is not present for individual synapse densities. Asymmetric innervation of VPM axons in L3 (i.e. innervation stops at 300µm) leads to depth-dependent synapse distributions.*

3. Channelrhodopsin-based (ChR2) functional mapping of VPM synapses in S1, qualitatively revealed two-dimensional (x/z) synapse distributions for L3 and L5B neurons [123]. The average distribution of L5B synapses on basal dendrites is more or less

radially symmetric. A second connectivity peak is detected on the trunk of the apical dendrite in L4 and almost no connections are observed for the apical tuft. Qualitatively, exactly this behavior is found for L5B neurons in the average cortical column as illustrated by two examples in Figure 4.15.

More importantly the ChR2-based mapping yield that on average L3 neurons receive thalamocortical input mainly in the lower parts of their basal dendrites. Figure 4.16 illustrates that the same finding is obtained by the here presented statistical, anatomy-based study. Averaging the presented three density maps and centering them on the soma position results in a distribution, where the peak innervation is shifted towards the lower parts of the basal tree.

However, I would argue that this finding is only true for average, soma-centered distributions. It does not reflect innervation of individual L3 neurons. Depending on their soma depth within L3, ranging from 250-550μm below the pial surface, the innervation of VPM axon will be more or less symmetric. The VPM axon innervation displays a significant decrease in density throughout L3, reaching zero around 250μm below the pial surface (Fig.4.13). Hence, than deeper a neuron is located within L3 than more symmetric the innervation will be. As shown in the right panel of Figure 4.16, neurons located around the top border of L3 are constraint by the VPM axon distribution and can therefore only make synaptic connections with the lower parts of their basal dendrites.

In consequence, I argue that both methods presented here, innervation- and ChR2-based, yield qualitatively the same results, but the interpretations are different. The here presented quantitative anatomical data suggest an alternative explanation for the asymmetric synapse distribution of L3 neurons. Specifically, the asymmetric innervation of this layer is due to inhomogeneous branching of VPM axons.

Chapter 5

Discussion

The here presented thesis describes a custom designed toolbox for reengineering of average functional neuronal networks with high anatomical accuracy, down to the subcellular (i.e. synaptic) level. It comprises five tools: NeuroCount, NeuroMorph, daVinci, NeuroCluster and NeuroNet. Their function is demonstrated by reengineering the thalamocortical part of the lemniscal pathway in the somatosensory whisker system of four week old rats. There, information obtained by a single facial whisker is processed within a cortical barrel column in S1. Excitation of columnar neurons, in response to passive whisker deflection during anesthesia, arises from synchronous thalamocortical input from a single barreloid in VPM. During active whisking, this lemniscal pathway is accompanied by additional thalamocortical input from the POm (i.e. part of the paralemniscal pathway). Such single whisker information is sufficient to trigger a "yes-or-no" gap-crossing behavior in rats. Hence, mechanistic understanding of structure and function of the cortical column network will potentially yield insights in how decision making evolves in mammalian brains.

However, reconstructing the barrel column from anatomical data that is obtained from many different experiments and animals results in an *average* network. Simulation of whisker evoked activity on such an average network model is only reasonable, if the variability of network anatomy is small. Therefore, one aim of this work was to prove that a functional cortical barrel column is also defined as an anatomical subunit with morphological features that are preserved from one animal to the next. This is achieved by new high-throughput methods that allow determination of statistically valid samples of anatomical data, such as the number and three-dimensional distribution of neurons and neuron-types, as well as reliable tracings of dendrites and axons.

Previously used manual standard methods, like sparse-sampling or Camera Lucida-based tracing, yielding neuron densities or morphology, respectively, proved to be time-consuming and in some cases even misleading. For example, assumptions about homogeneity in neuron density were shown to be unjustified for S1, explaining deviating results about neuron numbers in cortex in the past. Further, manual tracing of axons could only be performed by expert users, making the tracing of a representative axon sample almost unfeasible.

The presented methods of NeuroCount and NeuroMorph are based on newly available high-resolution mosaic/optical-sectioning microscopy and high-throughput automated image processing pipelines. Whereas NeuroCount is based on confocal image stacks that yield sufficient resolution and signal-to-noise ratio (SNR) to detect neuron somata, TLB mosaic microscopy lacks both, making automated tracing of axon arbors challenging. Therefore, one essential part of the NeuroMorph pipeline is the improvement in resolution, especially along the optical axis, and in SNR of weakly stained axonal structures. The characterization of the imaging system by Shack-Hartmann (SH) wavefront analysis and the resulting optimization and deconvolution is hence regarded as the key prerequisite for the semi-automated tracing of widely spreading axonal arbors.

Yielding the same precision as their manual counterparts [61], [83], [29], NeuroCount and NeuroMorph were used to determine the number and three-dimensional distribution of neurons in eight and five cubic millimeter large volumes in S1 and VPM, respectively. This data resulted in an average columnar soma distribution and number of neurons per VPM barreloid. Further, 78 dendrite reconstructions from S1, 5 axon reconstructions from L5A pyramidal neurons and 14 VPM axons could be traced. Using standardization by daVinci, classification by NeuroCluster and ultimately interconnection by NeuroNet, this data is the foundation for reengineering the average thalamocortical lemniscal pathway. As a result, ≈15200 full-compartmental excitatory cortical neurons, divided into eight types, are interconnected with 285 thalamocortical VPM axons. The dimensions of the somatic column are ≈390μm in diameter and 2mm in height. The total number of VPM synapses for these 15200 neurons is approximately 2,8 million. The obtained number of synapses per individual neuron, as well as their distributions resemble previous estimations and measurements.

In addition, the cortical barrel column in S1 of four week old rats can be regarded as a well defined anatomical unit. The described dimensions of the column correlate with higher neuron densities and VPM axon innervation (i.e. synapse density). Further, the variability in neuron distribution and number is relatively small between individual columns. The same is true for the number of neurons per barreloid. In addition, neuron tracings from many different animals share characteristic geometry and shape and can hence be grouped into anatomical neuron-types. The distribution of these neuron-types is preserved between animals. In summary, the number of neurons per column, their three-dimensional distribution, their morphology and their VPM innervation are well defined and allow for the reconstruction of an average cortical column *in silico*.

However, whereas the column dimensions are well defined by soma distribution and VPM innervation, this observation is not true for the dendritic network. Figure 5.1 shows neuron-type-specific VPM innervation volumes in comparison with their respective den-

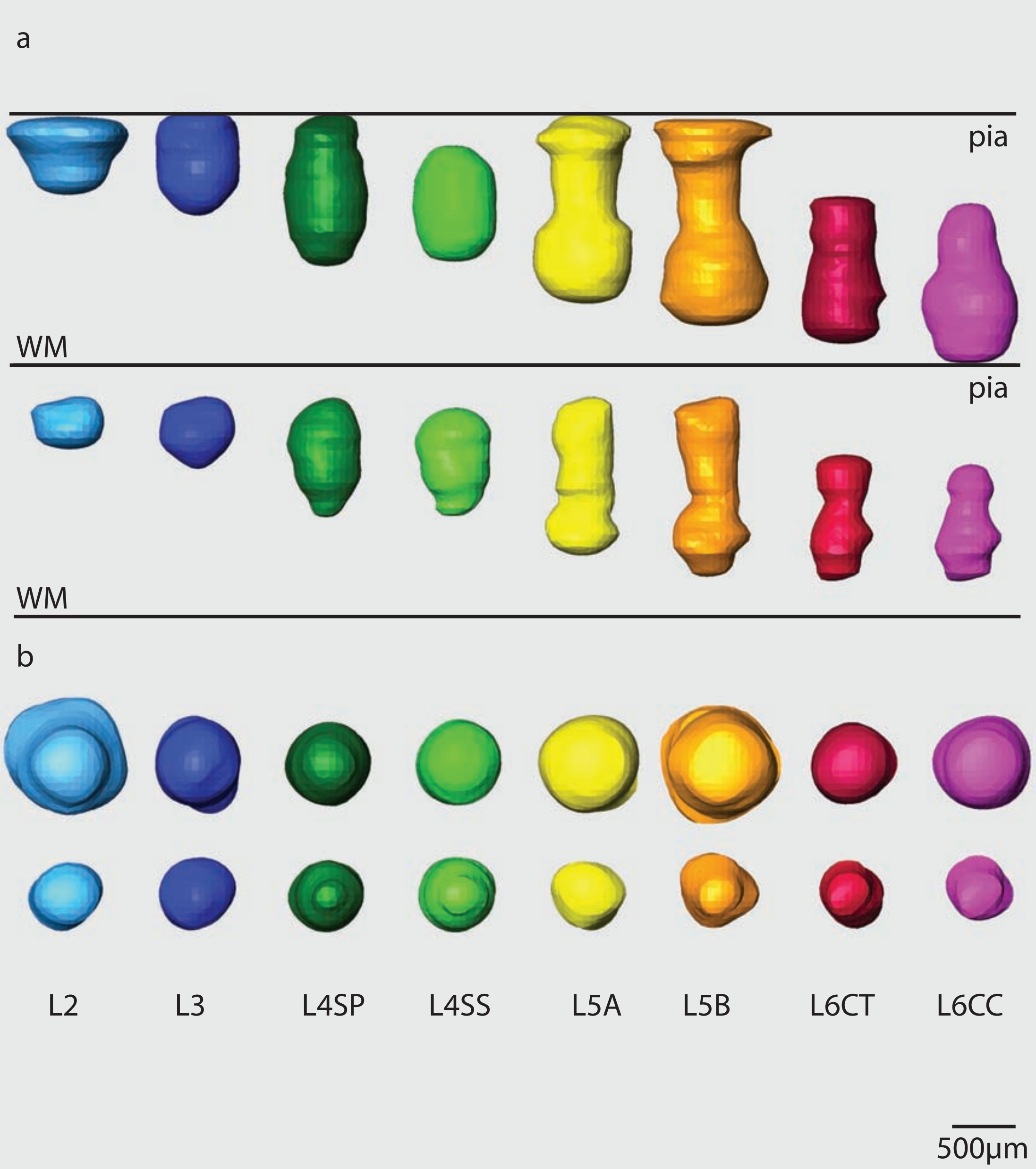

Figure 5.1: **3D neuron-type-specific VPM innervation volumes.** *(a) X/z-view of the dendrite volume and its respective overlap volume with the VPM bouton distribution is shown for each of the eight excitatory neuron-types in a cortical column of S1. (b) X/y-view. Whereas the dendrite distributions laterally exceed the column dimensions (i.e. $\approx 390\mu m$ diameter), VPM innervation volumes and hence synaptic connectivity resembles the columnar shape.*

drite volumes. This illustrates that VPM innervation determines the column dimensions, but dendrites from neurons within a cortical column extend further into adjacent columns. In consequence, I would argue that the reconstruction of an average cortical barrel column connected to neurons from one VPM barreloid is justified. Nevertheless, it remains questionable if the ultimate goal to simulate neuronal activity within such a network model will be feasible. I collaboration with Dr. Stefan Lang (IWR, Heidelberg) and Vincent J. Dercksen (ZIB, Berlin) I am currently developing strategies of how such high resolution network simulations should be approached.

Since the cortical column proved to be an anatomical unit with small variability, the network morphology will be kept fixed for every simulation trial. Only the synapse distributions will be changed slightly from one simulation trail to the next. Injecting always the same measured input to the network (i.e. number and timing of APs), simulation trials will be evaluated by their network output (e.g. increase in spiking rates). Analyzing the synapse distribution of trails that recover input/output relationships measured *in vivo* with the remaining trails will potentially yield spatial and/or temporal constraints for synapse numbers and position along dendrites. To accomplish such network simulations, four tools need to be developed:

Synapse mapper The first tool to implemented converts neuron-specific synapse distributions into concrete realizations. First, each neuron-specific three-dimensional synapse distribution is slightly altered for every trial. However, averaging across all trials yields the original mean distributions. Second, each synapse is placed randomly at a dendrite location within its respective 50μm bin.

Physiology tester The second tool needs to test each individual neuron for its electrophysiological properties. Neuron-type-specific HH-models are generated for each full-compartmental neuron. By injecting standardized input to each single-cell model, it needs to be automatically evaluated if the response reflects input/output relationships measured *in vitro* or *in vivo*.

Synapse tester The third tool will activate every individual synapse and tune its EPSP (i.e. excitatory postsynaptic potential) amplitude until a previously *in vitro* or *in vivo* measured amplitude is obtained at the soma.

Simulation analyzer Once the previous steps yield individual "functional" neurons, the simulation of such a network will produce large amounts of four-dimensional data. A 100ms simulation of a cortical column most likely results in several hundred Gigabytes of data per trial. Visualization and analysis of this data will prove to be great challenge.

However, it should be mentioned that so far, three important issues for building the cortical column network are missing:

1. At this stage the influence of interneurons is completely neglected. Even though they just make up about 15% of the entire neuron population, their large variability in function and anatomy [117], [146], will have a big influence on any network simulation. However, there is no methodological reason that prevents from application of the presented reconstruction approach in order to obtain the "interneuron column".

2. The here presented distributions of spines and boutons are estimated. Sparse sampling of spine numbers along dendrites and bouton numbers along axons resulted in the here presented density values. These values are extrapolated to entire neuronal trees. As for neuron somata, sparse sampling is only reasonable if the assumption of homogeneous distribution is justified. In cooperation with Thorben Kurz (MPIN, Munich), Dr. Kurt Saetzler (University of Ulster) and Dr. Stefan Lang (IWR,

Heidelberg) I am currently working on methods to determine the absolute number and distribution of spines and boutons along large portions of dendritic and axonal branching patterns, using SBFSEM [145].

3. So far, there is no reliable data about ion-channel distributions for any neuron-type available. Hence, full-compartmental HH-typed models for individual neuron-types are usually developed by a reverse engineering. There, single neurons are physiologically classified *in vitro* or *in vivo* and their morphology is reconstructed. Conversion into full-compartmental HH-typed models and fitting of channel distribution parameters can then yield neuron-specific models that reproduce the measured physiological behavior. However, this tedious approach is just described for very few neuron-types, one being L5B pyramidal neurons [147], [148].

Nevertheless, even though the described three issues need to be addressed before the reconstructed network can really be called a cortical column *in silico*, the here presented toolbox and results mark first necessary steps for reengineering and simulation of anatomically realistic neuronal networks. Further, first interactions between individual neuron-types might already be simulated and analyzed at this stage of reengineering. I would argue that the fast activation of L5B neurons by VPM input could already be simulated with the here presented network model. This argument is based on three reasons:

1. The input/output relationship due to passive whisker deflection is well described [10]. $\approx$60 nearly synchronous APs originating in one VPM barreloid cause an increase in supra-threshold activity in L5B neurons by $\approx$10 fold within the first 20ms after stimulus.

2. The physiology of L5B neurons is well studied by a large variety of *in vivo* experiments and resulted in a detailed HH-model for L5B neurons, which reproduces linear and

non-linear properties of dendrite computation [149], [150].

3. The number of ≈1100 neurons, directly activated by ≈300000 VPM synapses within 20ms, reduces the complexity of simulation by one order of magnitude, respectively, when compared with the entire column (i.e. ≈15000 neurons, ≈2800000 VPM synapses, 100ms).

However, simulation of lemniscal thalamocortical input, even for all eight neuron-types, will certainly not be sufficient to unravel the mechanistic principles of how decision making is triggered by the cortical column network. Specifically, the here presented VPM-S1 microcircuits form just a starting point for the reengineering of the single whisker pathway.

As demonstrated for L5A neurons, intracortical wiring exceeds the complexity of these thalamocortical microcircuits by several orders of magnitude. Therefore, in collaboration with Dr. Christiaan P.J. de Kock (VU Amsterdam) I started to reconstruct representative samples of axon morphology from all excitatory neuron-types in S1. Such intracortical axons spread much further than the lateral dimensions of one cortical barrel column. Hence interconnection of multiple adjacent columns (e.g. a 3x3 grid) will be inevitable, increasing the complexity of the network.

Further, corticothalamic and other subcortical projections from S1, as well as thalamocortical input from the POm need to be investigated and ultimately incorporated into the network model. In cooperation with Mike Hemberger (MPIN, Munich), I already started reengineering the VPM-RT inhibitory feedback loop, which is responsible for the exact timing of columnar VPM input.

In general, the here presented strategy is to reengineer any observed microcircuit between two neuron populations, verify its functionality and then add on the next circuit. Ultimately, this might produce a network model of a cortical column containing multiple intracolumnar circuits, which is embedded into intracortical microcircuits with adjacent columns, thalamocortical circuits from VPM and POm, intrathalamic circuits between VPM and RT, corticothalamic feedback circuits and subcortical microcircuits.

The here presented methodological pipeline describes a way of how this long time goal might be achieved. Tracing of S1 axon morphologies, quantification of the resultant projection domains and characterization of these circuits will result in a step-by-step network building process. However, I would argue that the here presented approach is not limited to the somatosensory whisker system of rats. Functionally and anatomically well defined networks are found in many brain regions across species. For example, insect brains display very stable network anatomy (e.g. visual system in flies) and similar approaches for reengineering such networks are currently investigated [151].

Nevertheless, the barrel-whisker system in rats and mice is unique in mammalian brains. Its segregated anatomical pathways, its relationship to single whisker input and finally its direct link to simple whisker-evoked behaviors make it the ideal system for reengineering of an average network. In general, neurons with similar interests tend to be vertically arrayed in the cortex, forming cortical columns, throughout all mammalian species [152], for example in V1 of macaque monkeys [153]. Further, recent evidence points to generic circuit motifs, present in primary somatosensory, auditory and motor cortex, secondary visual and medial prefrontal cortex in rats [154]. Hence, the presented reengineering approach might directly be transferred to columns in other cortical areas and species. However, much more complex input patterns, as well as questionable stability of column anatomy will be challenging.

In conclusion I would hence state that the here presented work opens new possibilities to derive anatomical data from large areas of the brain with high accuracy. In case of well-defined stimulus inputs and small variability of network architecture, this data will potentially allow the animation of electrical activity on average networks, which might give some insight into the spatial and/or temporal constraints in synapse numbers and distribution. These prerequisites are met for the thalamocortical part of the lemniscal pathway in rats. Hence, as a first step in modeling anatomically realistic networks of multiple thousand full-compartmental HH-typed neurons, the simulation of direct activation of L5B pyramidal neurons by VPM input could be approached.

However, whereas the scientific gain of such simulations remains open, the approach to determine quantitative anatomical data, itself, produces many new insights into the organization and function of the brain. Specifically, inhomogeneity of cortical layers in S1, deprivation-induced anatomical plasticity in thalamocortical connectivity in adult rats or the complexity of intracortical projections from L5A pyramidal neurons would have not been obtained, if this network reengineering approach wasn't started.

Bibliography

[1] Christof Koch. *Biophysics of Computation: Information Processing in Single Neurons*. Oxford University Press, 1999.

[2] Wulfram Gerstner and Werner M Kistler. *Spiking Neuron Models: Single Neurons, Populations, Plasticity*. Cambridge University Press, 2002.

[3] E. De Schutter and J. M. Bower. An active membrane model of the cerebellar purkinje cell ii. simulation of synaptic responses. *J Neurophysiol*, 71(1):401–419, Jan 1994.

[4] L F Abbott and T B Kepler. *Model neurons: from Hodgkin-Huxley to Hopfield*. Statistical Mechanics of Neuronal Networks. Springer, Berlin, 2008.

[5] Henry Markram. The blue brain project. *Nat Rev Neurosci*, 7(2):153–160, Feb 2006.

[6] M. Helmstaedter, C. P J de Kock, D. Feldmeyer, R. M. Bruno, and B. Sakmann. Reconstruction of an average cortical column in silico. *Brain Res Rev*, 55(2):193–203, Oct 2007.

[7] Carl C H Petersen. The functional organization of the barrel cortex. *Neuron*, 56(2):339–355, Oct 2007.

[8] T. A. Woolsey and H. van der Loos. The structural organization of layer iv in the somatosensory region (si) of mouse cerebral cortex. the description of a cortical field composed of discrete cytoarchitectonic units. *Brain Res*, 17(2):205–242, Jan 1970.

[9] Daniel J Simons and Peter W Land. Cortical barrels: Maps and plasticity. 2001.

[10] C. P J de Kock, R. M. Bruno, H. Spors, and B. Sakmann. Layer- and cell-type-specific suprathreshold stimulus representation in rat primary somatosensory cortex. *J Physiol*, 581(Pt 1):139–154, May 2007.

[11] Michael Brecht and Bert Sakmann. Whisker maps of neuronal subclasses of the rat ventral posterior medial thalamus, identified by whole-cell voltage recording and morphological reconstruction. *J Physiol*, 538(Pt 2):495–515, Jan 2002.

[12] Randy M Bruno and Bert Sakmann. Cortex is driven by weak but synchronously active thalamocortical synapses. *Science*, 312(5780):1622–1627, Jun 2006.

[13] D. Feldmeyer, V. Egger, J. Lubke, and B. Sakmann. Reliable synaptic connections between pairs of excitatory layer 4 neurones within a single 'barrel' of developing rat somatosensory cortex. *J Physiol*, 521 Pt 1:169–190, Nov 1999.

[14] C. C. Petersen and B. Sakmann. The excitatory neuronal network of rat layer 4 barrel cortex. *J Neurosci*, 20(20):7579–7586, Oct 2000.

[15] C. C. Petersen and B. Sakmann. Functionally independent columns of rat somatosensory barrel cortex revealed with voltage-sensitive dye imaging. *J Neurosci*, 21(21):8435–8446, Nov 2001.

[16] Randy M Bruno, Thomas T G Hahn, Damian J Wallace, Christiaan P J de Kock, and Bert Sakmann. Sensory experience alters specific branches of individual corticocortical axons during development. *J Neurosci*, 29(10):3172–3181, Mar 2009.

[17] Damian J Wallace and Bert Sakmann. Plasticity of representational maps in somatosensory cortex observed by in vivo voltage-sensitive dye imaging. *Cereb Cortex*, 18(6):1361–1373, Jun 2008.

[18] Amiram Grinvald and Rina Hildesheim. Vsdi: a new era in functional imaging of cortical dynamics. *Nat Rev Neurosci*, 5(11):874–885, Nov 2004.

[19] Thomas Berger, Aren Borgdorff, Sylvain Crochet, Florian B Neubauer, Sandrine Lefort, Bruno Fauvet, Isabelle Ferezou, Alan Carleton, Hans-Rudolf Lscher, and Carl C H Petersen. Combined voltage and calcium epifluorescence imaging in vitro and in vivo reveals subthreshold and suprathreshold dynamics of mouse barrel cortex. *J Neurophysiol*, 97(5):3751–3762, May 2007.

[20] Joachim Lübke and Dirk Feldmeyer. Excitatory signal flow and connectivity in a cortical column: focus on barrel cortex. *Brain Struct Funct*, 212(1):3–17, Jul 2007.

[21] Christiaan P. J. de Kock and Bert Sakmann. Spiking in primary somatosensory cortex during natural whisking behavior in the awake rat. *PNAS*, 2009.

[22] Ingrid Bureau, Francisca von Saint Paul, and Karel Svoboda. Interdigitated paralemniscal and lemniscal pathways in the mouse barrel cortex. *PLoS Biol*, 4(12):e382, Nov 2006.

[23] Gordon M G Shepherd and Karel Svoboda. Laminar and columnar organization of ascending excitatory projections to layer 2/3 pyramidal neurons in rat barrel cortex. *J Neurosci*, 25(24):5670–5679, Jun 2005.

[24] Dirk Feldmeyer, Arnd Roth, and Bert Sakmann. Monosynaptic connections between pairs of spiny stellate cells in layer 4 and pyramidal cells in layer 5a indicate that lemniscal and paralemniscal afferent pathways converge in the infragranular somatosensory cortex. *J Neurosci*, 25(13):3423–3431, Mar 2005.

[25] D. Schubert, R. Ktter, H. J. Luhmann, and J. F. Staiger. Morphology, electrophysiology and functional input connectivity of pyramidal neurons characterizes a genuine layer va in the primary somatosensory cortex. *Cereb Cortex*, 16(2):223–236, Feb 2006.

[26] K. A. Hutson and R. B. Masterton. The sensory contribution of a single vibrissa's cortical barrel. *J Neurophysiol*, 56(4):1196–1223, Oct 1986.

[27] Tansu Celikel and Bert Sakmann. Sensory integration across space and in time for decision making in the somatosensory system of rodents. *Proc Natl Acad Sci U S A*, 104(4):1395–1400, Jan 2007.

[28] Jakob Voigts, Bert Sakmann, and Tansu Celikel. Unsupervised whisker tracking in unrestrained behaving animals. *J Neurophysiol*, 100(1):504–515, Jul 2008.

[29] Marcel Oberlaender, Vincent J Dercksen, Robert Egger, Maria Gensel, Bert Sakmann, and Hans-Christian Hege. Automated three-dimensional detection and counting of neuron somata. *J Neurosci Methods*, 180(1):147–160, May 2009.

[30] B. G. Cragg. The density of synapses and neurones in the motor and visual areas of the cerebral cortex. *J Anat*, 101(Pt 4):639–654, Sep 1967.

[31] A. J. Rockel, R. W. Hiorns, and T. P. Powell. The basic uniformity in structure of the neocortex. *Brain*, 103(2):221–244, Jun 1980.

[32] D. C. Sterio. The unbiased estimation of number and sizes of arbitrary particles using the disector. *J Microsc*, 134(Pt 2):127–136, May 1984.

[33] C. Beaulieu. Numerical data on neocortical neurons in adult rat, with special reference to the gaba population. *Brain Res*, 609(1-2):284–292, Apr 1993.

[34] C. A. Knox. Effects of aging and chronic arterial hypertension on the cell populations in the neocortex and archicortex of the rat. *Acta Neuropathol*, 56(2):139–145, 1982.

[35] L. Werner, A. Wilke, R. Bldner, E. Winkelmann, and K. Brauer. Topographical distribution of neuronal types in the albino rat's area 17. a qualitative and quantitative nissl study. *Z Mikrosk Anat Forsch*, 96(3):433–453, 1982.

[36] A. Peters, D. A. Kara, and K. M. Harriman. The neuronal composition of area 17 of rat visual cortex. iii. numerical considerations. *J Comp Neurol*, 238(3):263–274, Aug 1985.

[37] M. A. Warren and K. S. Bedi. A quantitative assessment of the development of synapses and neurons in the visual cortex of control and undernourished rats. *J Comp Neurol*, 227(1):104–108, Jul 1984.

[38] Hanno Sebastian Meyer, Verena C Wimmer, Marcel Oberlaender, Bert Sakmann, and Moritz Helmstaedter. The number and distribution of interneurons in a cortical column of rat barrel cortex. *Cereb Cortex*, in preparation, 2009.

[39] Rebecca Gittins and Paul J Harrison. Neuronal density, size and shape in the human anterior cingulate cortex: a comparison of nissl and neun staining. *Brain Res Bull*, 63(2):155–160, Mar 2004.

[40] Sanjay S Kumar and Paul S Buckmaster. Neuron-specific nuclear antigen neun is not detectable in gerbil subtantia nigra pars reticulata. *Brain Res*, 1142:54–60, Apr 2007.

[41] R. J. Mullen, C. R. Buck, and A. M. Smith. Neun, a neuronal specific nuclear protein in vertebrates. *Development*, 116(1):201–211, Sep 1992.

[42] H. K. Wolf, R. Buslei, R. Schmidt-Kastner, P. K. Schmidt-Kastner, T. Pietsch, O. D. Wiestler, and I. Blmcke. Neun: a useful neuronal marker for diagnostic histopathology. *J Histochem Cytochem*, 44(10):1167–1171, Oct 1996.

[43] D. L. Kaufman, C. R. Houser, and A. J. Tobin. Two forms of the gamma-aminobutyric acid synthetic enzyme glutamate decarboxylase have distinct intraneuronal distributions and cofactor interactions. *J Neurochem*, 56(2):720–723, Feb 1991.

[44] Luca Muzio, Barbara DiBenedetto, Anastassia Stoykova, Edoardo Boncinelli, Peter Gruss, and Antonello Mallamaci. Conversion of cerebral cortex into basal ganglia in emx2(-/-) pax6(sey/sey) double-mutant mice. *Nat Neurosci*, 5(8):737–745, Aug 2002.

[45] J. F. Staiger, C. Masanneck, S. Bisler, A. Schleicher, W. Zuschratter, and K. Zilles. Excitatory and inhibitory neurons express c-fos in barrel-related columns after exploration of a novel environment. *Neuroscience*, 109(4):687–699, 2002.

[46] Walther Akemann, Yong-Mei Zhong, Noritaka Ichinohe, Kathleen S Rockland, and Thomas Knpfel. Transgenic mice expressing a fluorescent in vivo label in a distinct subpopulation of neocortical layer 5 pyramidal cells. *J Comp Neurol*, 480(1):72–88, Nov 2004.

[47] Tianming Liu, Gang Li, Jingxin Nie, Ashley Tarokh, Xiaobo Zhou, Lei Guo, Jarema Malicki, Weiming Xia, and Stephen T C Wong. An automated method for cell detection in zebrafish. *Neuroinformatics*, 6(1):5–21, 2008.

[48] K. Wu, D. Gauthier, and M. D. Levine. Live cell image segmentation. *IEEE Trans Biomed Eng*, 42(1):1–12, Jan 1995.

[49] H. S. Wu, J. Barba, and J. Gil. Iterative thresholding for segmentation of cells from noisy images. *J Microsc*, 197(Pt 3):296–304, Mar 2000.

[50] Gang Lin, Umesh Adiga, Kathy Olson, John F Guzowski, Carol A Barnes, and Badrinath Roysam. A hybrid 3d watershed algorithm incorporating gradient cues and object models for automatic segmentation of nuclei in confocal image stacks. *Cytometry A*, 56(1):23–36, Nov 2003.

[51] Gang Lin, Monica K Chawla, Kathy Olson, John F Guzowski, Carol A Barnes, and Badrinath Roysam. Hierarchical, model-based merging of multiple fragments for improved three-dimensional segmentation of nuclei. *Cytometry A*, 63(1):20–33, 2005.

[52] N. Malpica, C. O. de Solrzano, J. J. Vaquero, A. Santos, I. Vallcorba, J. M. Garca-Sagredo, and F. del Pozo. Applying watershed algorithms to the segmentation of clustered nuclei. *Cytometry*, 28(4):289–297, Aug 1997.

[53] Bjrn Nilsson and Anders Heyden. Segmentation of complex cell clusters in microscopic images: application to bone marrow samples. *Cytometry A*, 66(1):24–31, Jul 2005.

[54] L. Vincent and P. Soille. Watersheds in digital spaces: an efficient algorithm based on immersion simulations. 13(6):583–598, June 1991.

[55] H Chang and B Parvin. *Segmentation of three dimensional cell culture models from a single focal plane*. Springer, Berlin, 2006.

[56] Gang Lin, Monica K Chawla, Kathy Olson, Carol A Barnes, John F Guzowski, Christopher Bjornsson, William Shain, and Badrinath Roysam. A multi-model approach to simultaneous segmentation and classification of heterogeneous populations of cell nuclei in 3d confocal microscope images. *Cytometry A*, 71(9):724–736, Sep 2007.

[57] S. Raman, C. A. Maxwell, M. H. Barcellos-Hoff, and B. Parvin. Geometric approach to segmentation and protein localization in cell culture assays. *J Microsc*, 225(Pt 1):22–30, Jan 2007.

[58] M Ranzato, P E Taylor, J M House, R C Flagab, Y LeCun, and P Perona. Automatic recognition of biological particles in microscopic images. *Pattern Recognition Letters*, 28:31-9, 2007.

[59] J. G. White, W. B. Amos, and M. Fordham. An evaluation of confocal versus conventional imaging of biological structures by fluorescence light microscopy. *J Cell Biol*, 105(1):41–48, Jul 1987.

[60] D. A. Agard. Optical sectioning microscopy: cellular architecture in three dimensions. *Annu Rev Biophys Bioeng*, 13:191–219, 1984.

[61] Marcel Oberlaender, Randy M Bruno, Bert Sakmann, and Philip J Broser. Transmitted light brightfield mosaic microscopy for three-dimensional tracing of single neuron morphology. *J Biomed Opt*, 12(6):064029, 2007.

[62] Amira, 2009.

[63] D Stalling, M Westerhoff, and H C Hege. *Amira: a highly interactive system for visual data analysis. In: The visualization handbook*. Elsevier, 2005.

[64] B Stroustrup. *The C++ programming language*. Addison-Wesley, third edition, 2004.

[65] L Ibanéz, W Schroeder, L Ng, and J Cates. *The ITK software guide*. http://www.itk.org, 2005.

[66] R Gonzalez and R Woods. *Digital image processing*. Upper Saddle River, NJ 07458: Prentice-Hall, Inc., second edition, 2002.

[67] L Vincent and E R Dougherty. *Morphological segmentation of textures and particles. In: Digital image processing: fundamentals and applications*. Marcel-Dekker, 1994.

[68] L. Vincent. Morphological grayscale reconstruction in image analysis: applications and efficient algorithms. 2(2):176–201, April 1993.

[69] P Soille. *Morphological image analysis, principles and applications*. Berlin/Heidelberg: Springer-Verlag, 1999.

[70] Philip J Broser, R. Schulte, S. Lang, A. Roth, Fritjof Helmchen, J. Waters, Bert Sakmann, and G. Wittum. Nonlinear anisotropic diffusion filtering of three-dimensional image data from two-photon microscopy. *J Biomed Opt*, 9(6):1253–1264, 2004.

[71] X. J. Sun, L. P. Tolbert, and J. G. Hildebrand. Using laser scanning confocal microscopy as a guide for electron microscopic study: a simple method for correlation of light and electron microscopy. *J Histochem Cytochem*, 43(3):329–335, Mar 1995.

[72] L. P. Tolbert, X. J. Sun, and J. G. Hildebrand. Combining laser scanning confocal microscopy and electron microscopy in studies of the insect nervous system. *J Neurosci Methods*, 69(1):25–32, Oct 1996.

[73] K A Al-Kofahi, S Lasek, D H Szarowski, C J Pace, G Nagy, J N Turner, and B Roysam. Rapid automated three-dimensional tracing of neurons from confocal image stacks. In *IEEE Trans. Inf. Technol. Biomed.*, volume 6, pages 171–187, 2002.

[74] Alfredo Rodriguez, Douglas Ehlenberger, Kevin Kelliher, Michael Einstein, Scott C Henderson, John H Morrison, Patrick R Hof, and Susan L Wearne. Automated reconstruction of three-dimensional neuronal morphology from laser scanning microscopy images. *Methods*, 30(1):94–105, May 2003.

[75] Stephan Schmitt, Jan Felix Evers, Carsten Duch, Michael Scholz, and Klaus Obermayer. New methods for the computer-assisted 3-d reconstruction of neurons from confocal image stacks. *Neuroimage*, 23(4):1283–1298, Dec 2004.

[76] J. F. Evers, S. Schmitt, M. Sibila, and C. Duch. Progress in functional neuroanatomy: precise automatic geometric reconstruction of neuronal morphology from confocal image stacks. *J Neurophysiol*, 93(4):2331–2342, Apr 2005.

[77] S. L. Wearne, A. Rodriguez, D. B. Ehlenberger, A. B. Rocher, S. C. Henderson, and P. R. Hof. New techniques for imaging, digitization and analysis of three-dimensional neural morphology on multiple scales. *Neuroscience*, 136(3):661–680, 2005.

[78] Alfredo Rodriguez, Douglas B Ehlenberger, Patrick R Hof, and Susan L Wearne. Rayburst sampling, an algorithm for automated three-dimensional shape analysis from laser scanning microscopy images. *Nat Protoc*, 1(4):2152–2161, 2006.

[79] Wenyun He, Thomas A Hamilton, Andrew R Cohen, Timothy J Holmes, Christopher Pace, Donald H Szarowski, James N Turner, and Badrinath Roysam. Automated three-dimensional tracing of neurons in confocal and brightfield images. *Microsc Microanal*, 9(4):296–310, Aug 2003.

[80] K. Horikawa and W. E. Armstrong. A versatile means of intracellular labeling: injection of biocytin and its detection with avidin conjugates. *J Neurosci Methods*, 25(1):1–11, Aug 1988.

[81] Martin Parent and Andr Parent. Single-axon tracing and three-dimensional reconstruction of centre median-parafascicular thalamic neurons in primates. *J Comp Neurol*, 481(1):127–144, Jan 2005.

[82] S. K. Chow, H. Hakozaki, D. L. Price, N. A B MacLean, T. J. Deerinck, J. C. Bouwer, M. E. Martone, S. T. Peltier, and M. H. Ellisman. Automated microscopy system for mosaic acquisition and processing. *J Microsc*, 222(Pt 2):76–84, May 2006.

[83] M. Oberlaender, P. J. Broser, B. Sakmann, and S. Hippler. Shack-hartmann wave front measurements in cortical tissue for deconvolution of large three-dimensional mosaic transmitted light brightfield micrographs. *J Microsc*, 233(2):275–289, Feb 2009.

[84] D. Pinault. A novel single-cell staining procedure performed in vivo under electrophysiological control: morpho-functional features of juxtacellularly labeled thalamic cells and other central neurons with biocytin or neurobiotin. *J Neurosci Methods*, 65(2):113–136, Apr 1996.

[85] Troy W Margrie, Michael Brecht, and Bert Sakmann. In vivo, low-resistance, whole-cell recordings from neurons in the anaesthetized and awake mammalian brain. *Pflugers Arch*, 444(4):491–498, Jul 2002.

[86] M. Wong-Riley. Changes in the visual system of monocularly sutured or enucleated cats demonstrable with cytochrome oxidase histochemistry. *Brain Res*, 171(1):11–28, Jul 1979.

[87] M Born and E Wolf. *Principles of Optics*. Cambridge University Press, Cambridge, UK, 2003.

[88] T. J. Holmes and N. J. O'Connor. Blind deconvolution of 3d transmitted light brightfield micrographs. *J Microsc*, 200(Pt 2):114–127, Nov 2000.

[89] J. L. Beverage, R. V. Shack, and M. R. Descour. Measurement of the three-dimensional microscope point spread function using a shack-hartmann wavefront sensor. *J Microsc*, 205(Pt 1):61–75, Jan 2002.

[90] A. Chomik, A. Dieterlen, C. Xu, O. Haeberle, J.J. Meyer, and S. Jacquey. Qunatification in optical sectioning microscopy: a comparison of some deconvolution algorithms in view of 3d segmentation. *J. Optics-Nouv. Rev. D Optique*, 28:225–233, 1997.

[91] Suk Ho Lee, Moon Gi Kang, and Kyu Tae Park. Ccd noise filtering based on 3-dimensional nonlinear partial differential equation. 44(3):1086–1090, Aug. 1998.

[92] J Philip. Optical transfer function in three dimensions for large numerical aperture. *J. Mod. Opt.*, 46:1031–1042, 1999.

[93] S F Gibson and F Lanni. Experimental test of an analytical model of aberration in an oil-immersion objective lens used in 3-dimensional microscopy. *J. Opt. Soc. Am. A Opt. Image Sci. Vis*, 8:1601–1613, 1991.

[94] B R Frieden. Optical transfer of 3-dimensional objects. *J. Opt. Soc. Am.*, 57:56–66, 1967.

[95] D. A. Agard, Y. Hiraoka, P. Shaw, and J. W. Sedat. Fluorescence microscopy in three dimensions. *Methods Cell Biol*, 30:353–377, 1989.

[96] Y. Hiraoka, J. W. Sedat, and D. A. Agard. Determination of three-dimensional imaging properties of a light microscope system. partial confocal behavior in epifluorescence microscopy. *Biophys J*, 57(2):325–333, Feb 1990.

[97] H. T. M. Vandervoort and K.C. Strasters. Restoration of confocal images for quantitative image analysis. *J. Microsc.*, 178:165–181, 1995.

[98] E. Dusch, T. Dorval, N. Vincent, M. Wachsmuth, and A. Genovesio. Three-dimensional point spread function model for line-scanning confocal microscope with high-aperture objective. *J Microsc*, 228(Pt 2):132–138, Nov 2007.

[99] G. M. van Kempen and L. J. van Vliet. Background estimation in nonlinear image restoration. *J Opt Soc Am A Opt Image Sci Vis*, 17(3):425–433, Mar 2000.

[100] N Streibl. Depth transfer by an imaging system. *Optica. Acta.*, 31:1233–1241, 1984.

[101] N Streibl. Fundamental restrictions for 3-d light distributions. *Optik*, 66:341–354, 1984.

[102] N Streibl. 3-dimensional imaging by a microscope. *Am. A Opt. Image Sci. Vis.*, 2:121–127, 1985.

[103] T D Visser, J L Oud, and G J Brakenhoff. Refractive-index and axial distance measurements in 3-d microscopy. *Optik*, 90:17–19, 1992.

[104] G. M. van Kempen, L. J. van Vliet, and H. T. M. Vandervoort. A quantitative comparison of image restoration methods for confocal microscopy. *J. Microsc.*, 185:354–365, 1997.

[105] G. M. van Kempen and L. J. van Vliet. The influence of the regularization parameter and the first estimate on the performance of tikhonov regularized non-linear image restoration algorithms. *J Microsc*, 198 (Pt 1):63–75, Apr 2000.

[106] R Chandra, L Dagum, D Kohr, D Maydan, J McDonald, and R Menon. *Parallel Programming in OpenMP*. Academic Press, San Diego, 2001.

[107] C M Ma. On topology preservation in 3d thinning. *CVGIP: Image Understand.*, 59:328–339, 1994.

[108] X He, E Kischell, M Rioult, and T J Holmes. Three-dimensional thinning algorithm that peels the outmost layer with application to neuron tracing. *J. Comput.-Assist. Microsc.*, 10:123–135, 1998.

[109] R Klette and A Rosenfeld. *Digital Geometry, Geometric Methods for Digital Image Analysis*. Morgan Kaufman Publishers, San Francisco, 2004.

[110] M Seul, L O'Gormann, and M J Sammon. *Binary image analysis: Thinnig, Chaper 4, Section 7 in: Practicle Algorithms for Image Analysis*. Cambridge University Press, Cambridge, UK, 1995.

[111] P P Jonker. Skeletons in n dimensions using shape primitives. *Pattern Recognition Letters*, 23:677–686, 2002.

[112] A Rosenfel and J L Pfaltz. Distance functions on digital pictures. *Pattern Recognition Letters*, 1:33, 1968.

[113] Vincent J. Dercksen, Britta Weber, D. Guenther, Marcel Oberlaender, Stefan Prohaska, and H.-C. Hege. Automatic alignment of stacks of filament data. 2009.

[114] D. Baum. A point-based algorithm for multiple 3d surface alignment of drug-sized molecules. Master's thesis, Frei Universitt Berlin, 2007.

[115] Kevin J Bender, Juliana Rangel, and Daniel E Feldman. Development of columnar topography in the excitatory layer 4 to layer 2/3 projection in rat barrel cortex. *J Neurosci*, 23(25):8759–8770, Sep 2003.

[116] Joachim Lübke, Arnd Roth, Dirk Feldmeyer, and Bert Sakmann. Morphometric analysis of the columnar innervation domain of neurons connecting layer 4 and layer 2/3 of juvenile rat barrel cortex. *Cereb Cortex*, 13(10):1051–1063, Oct 2003.

[117] Moritz Helmstaedter, Bert Sakmann, and Dirk Feldmeyer. Neuronal correlates of local, lateral, and translaminar inhibition with reference to cortical columns. *Cereb Cortex*, 19(4):926–937, Apr 2009.

[118] C. P J de Kock, Stefan Lang, Marcel Oberlaender, Randy Bruno, Radoslav Enchev, Bert Sakmann, and Moritz Helmstaedter. 3d-registration of neuron morphologies to a cortical column. *(in preparation)*, 2009.

[119] Mihael Ankerst, Markus M Breunig, Hans-Peter Kriegel, and Joerg Sander. Optics: Ordering points to identify the clustering structure. In *SIGMOD Philadelphia*, 1999.

[120] Melanie Mitchell. *An introduction to genetic algorithms.* The MIT Press, Cambridge, 1998.

[121] J. Kozloski, K. Sfyrakis, S. Hill, F. Schürmann, C. Peck, and H. Markram. Identifying, tabulating, and analyzing contacts between branched neuron morphologies. *IBM J. Res. Dev.*, 52(1/2):43–55, 2008.

[122] Padraig Gleeson, Volker Steuber, and R. Angus Silver. neuroconstruct: a tool for modeling networks of neurons in 3d space. *Neuron*, 54(2):219–235, Apr 2007.

[123] Leopoldo Petreanu, Tianyi Mao, Scott M Sternson, and Karel Svoboda. The subcellular organization of neocortical excitatory connections. *Nature*, 457(7233):1142–1145, Feb 2009.

[124] Dirk Schubert, Rolf Ktter, and Jochen F Staiger. Mapping functional connectivity in barrel-related columns reveals layer- and cell type-specific microcircuits. *Brain Struct Funct*, 212(2):107–119, Sep 2007.

[125] P. W. Land, S. A. Buffer, and J. D. Yaskosky. Barreloids in adult rat thalamus: three-dimensional architecture and relationship to somatosensory cortical barrels. *J Comp Neurol*, 355(4):573–588, May 1995.

[126] Patrik Krieger, Thomas Kuner, and Bert Sakmann. Synaptic connections between layer 5b pyramidal neurons in mouse somatosensory cortex are independent of apical dendrite bundling. *J Neurosci*, 27(43):11473–11482, Oct 2007.

[127] Veronica Egger, Thomas Nevian, and Randy M Bruno. Subcolumnar dendritic and axonal organization of spiny stellate and star pyramid neurons within a barrel in rat somatosensory cortex. *Cereb Cortex*, 18(4):876–889, Apr 2008.

[128] E. M. Kasper, A. U. Larkman, J. Lbke, and C. Blakemore. Pyramidal neurons in layer 5 of the rat visual cortex. i. correlation among cell morphology, intrinsic electrophysiological properties, and axon targets. *J Comp Neurol*, 339(4):459–474, Jan 1994.

[129] Alexander Groh, Hanno S Meyer, Eric F Schmidt, Nathaniel Heintz, Bert Sakmann, and Patrik Krieger. Cell-type specific properties of pyramidal neurons in neocortex

underlying a layout that is modifiable depending on the cortical area. *Cereb Cortex*, Jul 2009.

[130] Z. W. Zhang and M. Deschnes. Intracortical axonal projections of lamina vi cells of the primary somatosensory cortex in the rat: a single-cell labeling study. *J Neurosci*, 17(16):6365–6379, Aug 1997.

[131] Pratap Kumar and Ora Ohana. Inter- and intralaminar subcircuits of excitatory and inhibitory neurons in layer 6a of the rat barrel cortex. *J Neurophysiol*, 100(4):1909–1922, Oct 2008.

[132] Gordon M G Shepherd, Armen Stepanyants, Ingrid Bureau, Dmitri Chklovskii, and Karel Svoboda. Geometric and functional organization of cortical circuits. *Nat Neurosci*, 8(6):782–790, Jun 2005.

[133] Andreas Frick, Dirk Feldmeyer, Moritz Helmstaedter, and Bert Sakmann. Monosynaptic connections between pairs of l5a pyramidal neurons in columns of juvenile rat somatosensory cortex. *Cereb Cortex*, 18(2):397–406, Feb 2008.

[134] Sylvain Crochet and Carl C H Petersen. Correlating whisker behavior with membrane potential in barrel cortex of awake mice. *Nat Neurosci*, 9(5):608–610, May 2006.

[135] J. P. Donoghue and S. P. Wise. The motor cortex of the rat: cytoarchitecture and microstimulation mapping. *J Comp Neurol*, 212(1):76–88, Nov 1982.

[136] C. Rapisarda, A. Palmeri, G. Aicardi, and S. Sapienza. Multiple representations of the body and input-output relationships in the agranular and granular cortex of the chronic awake guinea pig. *Somatosens Mot Res*, 7(3):289–314, 1990.

[137] V. J. Brown, E. M. Bowman, and T. W. Robbins. Response-related deficits following unilateral lesions of the medial agranular cortex of the rat. *Behav Neurosci*, 105(4):567–578, Aug 1991.

[138] Philip J Broser, Sezgin Erdogan, Valery Grinevich, Pavel Osten, Bert Sakmann, and Damian J Wallace. Automated axon length quantification for populations of labelled neurons. *J Neurosci Methods*, 169(1):43–54, Mar 2008.

[139] P. W. Land and D. J. Simons. Metabolic and structural correlates of the vibrissae representation in the thalamus of the adult rat. *Neurosci Lett*, 60(3):319–324, Oct 1985.

[140] D. Pinault and M. Deschnes. Anatomical evidence for a mechanism of lateral inhibition in the rat thalamus. *Eur J Neurosci*, 10(11):3462–3469, Nov 1998.

[141] D. Pinault and M. Deschnes. Projection and innervation patterns of individual thalamic reticular axons in the thalamus of the adult rat: a three-dimensional, graphic, and morphometric analysis. *J Comp Neurol*, 391(2):180–203, Feb 1998.

[142] P. B. Arnold, C. X. Li, and R. S. Waters. Thalamocortical arbors extend beyond single cortical barrels: an in vivo intracellular tracing study in rat. *Exp Brain Res*, 136(2):152–168, Jan 2001.

[143] Verena C Wimmer, Philip J Broser, Thomas Kuner, Bert Sakmann, and Randy M Bruno. Deprivation-induced anatomical plasticity of thalamocortical axons in adults. *Journal of Neuroscience*, 2009.

[144] Hanno Sebastian Meyer, Verena Wimmer, Mike Hemberger, Christiaan de Kock, Bert Sakmann, and Moritz Helmstaedter. Neuron density profiles of a thalamocortical innervation column in rat somatosensory cortex. *Cereb Cortex*, in preparation, 2009.

[145] Winfried Denk and Heinz Horstmann. Serial block-face scanning electron microscopy to reconstruct three-dimensional tissue nanostructure. *PLoS Biol*, 2(11):e329, Nov 2004.

[146] Moritz Helmstaedter, Bert Sakmann, and Dirk Feldmeyer. The relation between dendritic geometry, electrical excitability, and axonal projections of l2/3 interneurons in rat barrel cortex. *Cereb Cortex*, 19(4):938–950, Apr 2009.

[147] Thomas Nevian, Matthew E Larkum, Alon Polsky, and Jackie Schiller. Properties of basal dendrites of layer 5 pyramidal neurons: a direct patch-clamp recording study. *Nat Neurosci*, 10(2):206–214, Feb 2007.

[148] Matthew E Larkum, Thomas Nevian, Maya Sandler, Alon Polsky, and Jackie Schiller. Synaptic integration in tuft dendrites of layer 5 pyramidal neurons: a new unifying principle. *Science*, 325(5941):756–760, Aug 2009.

[149] Bartlett W Mel and Jackie Schiller. On the fight between excitation and inhibition: location is everything. *Sci STKE*, 2004(250):PE44, Sep 2004.

[150] Alon Polsky, Bartlett W Mel, and Jackie Schiller. Computational subunits in thin dendrites of pyramidal cells. *Nat Neurosci*, 7(6):621–627, Jun 2004.

[151] Alexander Borst and Juergen Haag. Neural networks in the cockpit of the fly. *J Comp Physiol*, 188, 2002.

[152] William H Calvin. *Cortical Columns, Modules, and Hebbian Cell Assemblies in "The Handbook of Brain Theory and Neural Networks"*. Bradford Books/MIT Press, 1995.

[153] D. H. Hubel and T. N. Wiesel. Ferrier lecture. functional architecture of macaque monkey visual cortex. *Proc R Soc Lond B Biol Sci*, 198(1130):1–59, Jul 1977.

[154] Thomas K Berger, Rodrigo Perin, Gilad Silberberg, and Henry Markram. Frequency-dependent disynaptic inhibition in the pyramidal network - a ubiquitous pathway in the developing rat neocortex. *J Physiol*, Sep 2009.